Ultrafast Coherently Controlled Currents in GaAs: Physics and Applications

Dissertation

zur Erlangung des Doktorgrades der Naturwissenschaften

der Fakultät Physik der Technischen Universität Dortmund

vorgelegt von

Elmar Sternemann

Juli 2015

Erster Gutachter:	Prof. Dr. Markus Betz	(Technische Universität Dortmund)
Zweiter Gutachter:	Prof. Dr. Torsten Meier	(Universität Paderborn)

Datum der Einreichung:	27. Juli 2015
Datum der Disputation:	29. September 2015

Contents

Chapter 1

Introduction

The development of the laser in the early 1960s [1–3] laid the foundation for exploring a novel class of optical phenomena which is generally referred to as nonlinear optics [4; 5]. With the availability of monochromatic, highly directed laser beams, it became possible to achieve much higher illumination intensities than before. When focused on a material, the corresponding electric field amplitude of a laser beam can even approach the magnitude of intra-atomic fields. In this case, the light-matter interaction significantly deviates from the rules of classical or linear optics.

Probably the most prominent example of nonlinear optics is second harmonic generation. It was also one of the first nonlinear effects to be demonstrated [6]. A laser beam incident on a quartz crystal resulted in the generation of a beam with half the input wavelength. The emission was caused by atoms in the crystal which coupled to the high electric field amplitude of the incident beam. As it is characteristic for nonlinear effects, the power of the second harmonic beam depends nonlinearly, in this case quadratically, on the input intensity.

Second harmonic generation illustrates the coupling of differently colored beams via nonlinear light-matter interaction. It follows that the superposition principle does not necessarily hold within the regime of nonlinear optics. In linear optics, the electric field components of two superimposed electromagnetic waves add up linearly. If these are coherent and exhibit the same wavelength, interference effects will occur. Depending on the relative phase, the amplitudes of both waves may add up or cancel each other out. However, if the two waves feature different wavelengths, they do not interfere.

A striking manifestation of the breakdown of the superposition principle is the nonlinear effect of coherently controlled current injection [7; 8], in the following denoted as QUIC (quantum interference control) [9]. It is based on the interference of two differently colored laser beams which are coherently superimposed on a solid, typically a semiconductor. The relative phase of both beams determines the amplitude of a current that is optically injected in the material.

The underlying mechanism of QUIC is a simultaneous excitation of the same electronic transitions via two harmonically related beams. More specifically, their wavelength and thus their energy differ by a factor of two. Owing to the energetic difference, both beams cannot directly excite the same transitions. However, the energy of two photons from the longer-wavelength beam may be combined via two-photon absorption. This effect describes the excitation of one electron transition via the simultaneous absorption of two photons [10; 11]. Being a nonlinear optical process, it requires high intensities to be observed.

Taken alone, one-photon absorption of the higher-energetic beam and two-photon absorption of the other beam only result in an increase of the number of excited charge carriers. If both beams are superimposed, the two absorption paths interfere. In a semiconductor, this quantum interference eventually results in an unequal excitation of electrons with opposite velocity. Thus, a current begins to flow. Its direction and amplitude can be controlled by the relative phase and polarization of both beams.

In 1997, shortly after the theoretical prediction [7], QUIC was first demonstrated in the prototypical direct band gap semiconductor gallium arsenide (GaAs) [8]. Two-color pulse pairs which were coherently superimposed on the semiconductor resulted in a measurable voltage drop across two metallic contacts on top of the sample. The pulse pairs were derived from an ultrashort pulse laser. By concentrating the energy in pulses with durations in the order of pico- or femtoseconds, such a system allows to realize much higher peak intensities than a continuous-wave laser [12; 13]. Later, QUIC has also been applied to other material classes, like the indirect band gap semiconductors silicon and germanium [14; 15], graphene [16], the topological insulator Bi_2Se_3 [17] or copper [18].

QUIC differs fundamentally from current generation via application of a voltage. The latter requires at least two electrical contacts which have to be defined beforehand on the sample. An applied electric field results in a gradual acceleration of the carriers. The rise and fall time of the resulting current is limited by parasitic capacitances of the circuit; it is at least in the order of picoseconds.

A current which is induced via an ultrashort pulse pair emerges practically instantaneously. As the electrons are directly excited into states with non-zero velocity, they do not have to be accelerated by an external field. In this case, the time scales are determined by the light-matter interaction which is typically limited by the pulse duration. Therefore, ultrashort current bursts in the order of femtoseconds can be realized. Besides direct current measurements via electrical contacts on the sample, these bursts can be detected via their emission of terahertz radiation [19].

The unique properties of QUIC make it a versatile tool for studies of electron transport. As an all-optical process, it allows to inject currents at arbitrary spots with microscopic dimensions. Most notably, current injection has been demonstrated at carbon nanotubes [20; 21] or even single GaAs nanowires [22]. By controlling the polarization and optical

phase of the pulses, direction-resolved information about the electron transport can be retrieved. In contrast to voltage-induced currents, it is even possible to inject current components which are perpendicular to the axis of a nanowire.

The explicit phase dependence of current injection can be utilized for spectroscopic studies. A sample which is placed into the beam path alters the optical phase and influences the injected current. In turn, spectrally-resolved transmission properties of the sample can be extracted from measurements of the current [23; 24]. Furthermore, current measurements allow to determine the carrier-envelope phase of the incident laser pulses [25; 26]. This parameter refers to the relative phase of the electromagnetic wave with respect to the peak of the pulses.

As one part of this thesis, a detection technique is presented which utilizes QUIC in a GaAs sample to retrieve the spectral phase of the incident laser pulses. Upon propagation through a dispersive medium, for example glass, the spectral components of a laser pulse are temporally shifted due to a wavelength-dependent speed of light [27, ch. 22.1; 28, ch. 17.1]. This effect manifests in the spectral phase of the electric field component and may lead to a temporal broadening of the pulse. The broadening becomes the more relevant, the shorter the pulse is. In particular, pulses with sub-100 fs pulse durations are significantly influenced by dispersion [29, p. A150ff]. In order to fully characterize such ultrashort pulses and eventually compensate the broadening, it is desirable to measure the spectral phase.

The determination of the spectral phase is a non-trivial task as it is not directly accessible. Measurements with a photodiode, for example, only reveal the intensity of the electric field, which does not contain explicit information about the phase. Furthermore, the temporal resolution of such an electronic-based detection is not sufficient for femtosecond pulses. Therefore, more sophisticated measurement schemes have been developed [30; 31]. Typically, these are based on the detection of a nonlinear light-matter interaction which is caused by two superimposed pulse replicas. For example, SHG-FROG (second harmonic generation – frequency-resolved optical gating) is based on second harmonic generation by two temporally shifted pulse replicas [32–34]. An iterative algorithm is then able to reconstruct the spectral phase from the recorded second harmonic intensity.

The alternative phase-retrieval scheme presented in this thesis is based on the explicit phase dependence of QUIC. The spectral phase of the laser pulses manifests directly in measurements of the injected current and is shown to be extractable without the need for a complex algorithm. Apart from a theoretical derivation of the underlying concept, the presented study also comprises an experimental evaluation of this phase-retrieval scheme.

Another part of this thesis focuses on the interaction between QUIC and a voltage-induced current. More specifically, the experimental realization of an optical current detection scheme proposed by Liu *et al.* [35; 36] is investigated at a thin GaAs sample.

In essence, the presence of a current in the sample is expected to inhibit the injection of an additional current. As a consequence, the absorption of the pulse pair should be reduced. Therefore, the voltage-induced current could be detected by analyzing the pulse pair transmission.

Typically, current measurement techniques rely on the detection of a voltage drop or the detection of the surrounding magnetic field [37; 38]. These schemes require external probes which limit the spatial resolution. By contrast, an all-optical current detection scheme would only be limited by the laser beam which can be focused on arbitrary spots with microscopic dimensions. Furthermore, the temporal resolution would not be limited by electronics. By using femtosecond pulses, ultrafast current dynamics could be investigated.

Apart from practical applications, the thesis also addresses the underlying physics of QUIC itself. A special focus lies on the current injection at high excitation intensities. Theoretical studies show marked deviations from the initial description of QUIC in this regime [39–42]. In particular, the current amplitude is predicted to stagnate due to saturation of the induced transitions. Furthermore, the carriers are expected to strongly couple to the high electric field amplitudes of the laser pulses. Ultimately, even the influence of Rabi oscillations, a coherent light-induced oscillation of the carrier population, is predicted [41; 42]. However, this high-intensity regime is rather unexplored experimentally.

In this thesis, the high-intensity regime of QUIC is investigated within a collaborative theoretical as well as experimental study. The current injection in a contacted GaAs sample is analyzed with respect to its power dependence and the temporal behavior of the excited carriers. These measurements are supported by theoretical simulations by Huynh Thanh Duc from the Ho Chi Minh City Institute of Physics and Torsten Meier from the University of Paderborn.

This thesis is structured as follows: Chapter 2 lays out the theoretical background of nonlinear optics and QUIC. The experimental methods for the realization and measurement of QUIC are described in Chapter 3. Furthermore, this chapter details the preparation as well as the properties of the employed samples, which are based on low-temperature grown GaAs (LT-GaAs). Chapter 4 presents the collaborative study of QUIC in the high-intensity regime. The underlying theory and the experimental implementation of spectral phase-retrieval via QUIC are covered in Chapter 5. Chapter 6 addresses the experimental implementation of an all-optical current detection scheme based on QUIC. Finally, the results of this thesis are briefly summarized in Chapter 7.

Parts of the results that are presented within this thesis have already been published in references [43–45]. Furthermore, parts of this thesis are in preparation for publication elsewhere [46].

Chapter 2

Theoretical Background

This thesis covers different aspects of coherently controlled current injection (QUIC) in semiconductors. By superimposing a laser beam with its second harmonic, QUIC allows to optically induce an electrical current without the need for an externally applied voltage. Direction and amplitude of the injected current can be controlled by the relative phase and polarization of the two beams.

QUIC belongs to the field of nonlinear optics that is briefly introduced in chapter 2.1. The specific theory of QUIC is sketched in chapter 2.2.

2.1 Nonlinear Optics

Optical phenomena are distinguished between linear and nonlinear effects. Everyday phenomena like reflection, refraction or absorption belong to the field of linear optics; that is, the respective coefficients, such as the absorption coefficient, are independent of the irradiance. More precisely, the term "linear" refers to the proportionality between the electric field amplitude $\mathbf{E}$ of the exciting electromagnetic wave and the resulting polarization $\mathbf{P}$ in the material which must not be confused with the polarization of the electric field. The proportionality factor is given by the frequency-dependent electric susceptibility $\chi(\omega)$ [27, ch. 21.1]:

$$\mathbf{P} = \epsilon_0 \chi \mathbf{E} \tag{2.1}$$

Phenomenologically, the polarization $\mathbf{P}$ can be described as the result of a collective displacement of bound electrons induced by the electric field amplitude $\mathbf{E}$ of the incident electromagnetic wave. The electrons begin to oscillate and, according to Maxwell's laws, emit an electromagnetic wave with a wavelength given by the oscillation frequency. The resulting superimposed electromagnetic field depends on the relative phase of the exciting as well as the emitted wave. For example, reflection at a metal surface can be interpreted as a destructive interference in transmission direction and constructive interference in the opposite direction. The polarization $\mathbf{P}$ scales linearly as long as the assumption of a

parabolic binding potential holds.

The invention of the laser in the early 1960s [1–3] triggered the research field of nonlinear optics [4; 5]. When focused on a material, the electric field amplitude of a laser beam can approach the magnitude of intra-atomic fields. As a consequence, the linear approximation of the polarization $\mathbf{P}$ breaks down. Crystalline solids generally exhibit a relative low threshold intensity for the observation of nonlinear optical effects. Their high density and periodic atomic arrangement can be utilized for an efficient constructive superposition of the nonlinear responses of the individual atoms, also known as phase matching [47, ch. 11.3.3].

One of the first nonlinear effects to be demonstrated was second harmonic generation (SHG) in a crystalline quartz sample [6], i.e. an electromagnetic wave with double the frequency of the incoming field was emitted. In terms of the phenomenological picture, the emission can be interpreted as the result of an asymmetry in the electrons' binding potential. Owing to this asymmetry, the electron movement is not entirely harmonic but contains components with double the frequency [47, ch. 11.2.1]. This effect becomes more relevant with increasing field amplitude. Specifically, the intensity of the emitted second harmonic beam scales with the squared intensity of the input beam.

Nonlinear effects can be incorporated into equation (2.1) via an expansion of the susceptibility χ in terms of the driving field $\mathbf{E}$; for example, SHG is described by the second order susceptibility $\chi^{(2)}$ [5, ch. 3.1]:

$$\mathbf{P} = \epsilon_0 \chi^{(1)} \mathbf{E} + \epsilon_0 \chi^{(2)} \mathbf{E}^2 + \epsilon_0 \chi^{(3)} \mathbf{E}^3 + \dots \tag{2.2}$$

As a general rule, $\chi^{(i)}$ declines rapidly with the order i. The orders $\chi^{(i)}$ are differently sized tensors that depend on the polarization as well as the wavelength of the incoming beams. However, because of symmetry conditions, there is typically only a very limited number of nonzero tensor components for crystalline solids [47, ch. 11.3.2]. Higher order terms that are nonlinear in the electric field amplitude $\mathbf{E}$ may even stem from beams of different wavelengths. An example for such an effect is nonlinear frequency mixing [27, p. 883ff]. The superposition of two beams can result in a differently colored beam with the sum- or difference frequency. As a generalization of SHG, it is also described by $\chi^{(2)}$.

QUIC is a third order nonlinear effect that is related to $\chi^{(3)}$ [48]. It relies on a coherent superposition of two-photon and one-photon absorption of a fundamental beam and its second harmonic, respectively. The former process can be thought of as a nonlinear transition induced by a simultaneous absorption of two photons [10; 11]. Its transition energy corresponds to the sum of both photon energies. A detailed theoretical derivation of QUIC is outlined in the following chapter. A more extensive review of nonlinear optics can be found elsewhere [4; 5; 27, ch. 21; 47, ch. 11].

2.2 Coherently Controlled Current Injection (QUIC)

QUIC relies on the coherent interaction of a solid, in this case a direct band gap semiconductor, with a light wave as well as with its second harmonic. Both waves are able to excite the same electron transitions from a valence to the conduction band via one- and two-photon absorption. The coherent superposition of two transition paths connecting the same states leads to quantum interference. As a result, an anisotropic carrier distribution is excited that manifests as a current flow.

The governing parameter of the quantum interference is the relative phase between the fundamental and second harmonic wave. The explicit phase dependence distinguishes QUIC from the majority of other nonlinear effects. For example, the phase dependence of SHG is only implicit by the influence on the envelope of the emitted wave (cf. chapter 5.2). An illustrative analogue for the interference of transition paths is Young's double slit experiment that is sketched later in this chapter. The microscopic theory of QUIC is based on time-dependent perturbation theory and outlined at the end of this chapter.

The general idea of quantum interference controlled via phase manipulation dates back to the late 1960s and early 1970s (see [48] and references within). Not least because of long coherence times, these concepts were first demonstrated at discrete energy levels in atoms and simple molecules. The control of photochemical reactions in molecules established the research field of coherence control. Implementations of coherence control in solids initially focused on atomic-like systems, for example excitons, quantum dots or nanostructures. In particular, directed ionization of AlGaAs/GaAs quantum wells that results in a current flow was demonstrated in 1995 [49].

QUIC in bulk semiconductors, the subject of this thesis, was first theoretically proposed by the group of J. E. Sipe in 1996 [7]. Subsequently, QUIC was experimentally demonstrated in GaAs by the group of H. M. van Driel [8]. The mechanism for current generation crucially differs from directed ionization. In the latter case, the current flow is merely a result of charge separation. By contrast, QUIC directly allows to manipulate the carrier velocity by inducing a carrier distribution that is asymmetric in the momentum space.

In the following, the underlying mechanism of QUIC in bulk semiconductors is discussed for the prototypical material GaAs. Fig. 2.1(a) sketches its direct energy dispersion $E(k)$ around $k = 0$. The band gap is denoted by E_G. For simplicity, $\mathbf{k}$ is restricted to one dimension and only one conduction band and one valence band is shown. To inject a current into GaAs, a linearly polarized fundamental wave is coherently superimposed with its second harmonic exhibiting twice the photon energy. The wavelengths are chosen such that the respective photon energies $\hbar\omega$ and $2\hbar\omega$ of the fundamental beam and its second

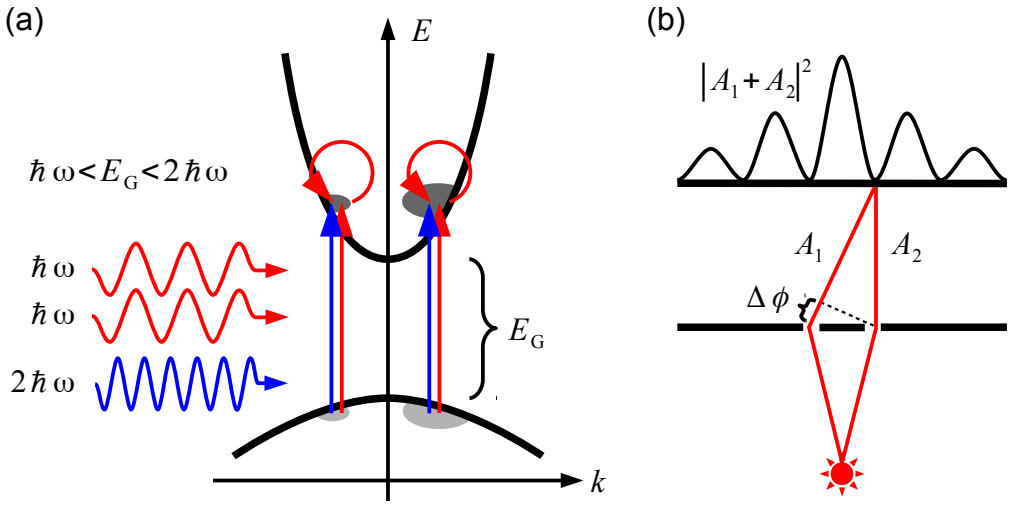

Fig. 2.1: (a) Schematic illustration of QUIC in a direct band gap semiconductor: The simultaneous absorption of two photons with the energy $\hbar\omega$ and one photon with $2\hbar\omega$ results in an interference of the addressed transitions. As a consequence, an asymmetric carrier distribution may be excited that corresponds to a current flow. (b) Sketch of Young's double slit experiment: The light propagation of a coherent light source is restricted to two slits. The phase difference between the two waves propagating through different slits manifests as interference pattern on a screen.

harmonic fulfill the energy relation $\hbar\omega < E_\mathrm{G} < 2\hbar\omega$. Whereas photons of the second harmonic beam are directly absorbed, the lowest order interaction of the fundamental beam is two-photon absorption. Both absorption processes are depicted with differently colored arrows in Fig. 2.1(a). Owing to the negligible photon momentum, the transitions connect states with practically the same k value. In accordance with time-dependent perturbation theory (see below), two-photon absorption is illustrated by an electron transition involving an additional intermediate state.

One-photon absorption induces electron transitions from the valence to the conduction band with an energy difference determined by the photon energy. If the photon energy exceeds the band gap E_G, the electrons are excited at $k \neq 0$. According to the effective mass approximation, the electron velocity is related to the slope $\partial E(k)/\partial k$ of the energy dispersion [50, ch. 12]. Despite a nonzero slope at $k \neq 0$, one-photon absorption of linearly polarized waves alone does not induce a current because it is an isotropic process[1]. There is an equal number of carriers generated at $-k$ and $+k$ with opposite velocities that cancel each other out. The same argument holds for two-photon absorption; it cannot optically induce a current, either. However, if both processes are combined, their carrier distributions do not simply add up. Both transition paths interfere and generate an anisotropic carrier

[1]There is a current injection scheme that is based on the absorption of only one elliptically polarized beam. It was demonstrated by the group of H. M. Driel [51] and can be derived using a similar theory as the two-color current injection [48].

distribution that corresponds to a current flow.

Young's double-slit experiment, depicted in Fig. 2.1(b), constitutes an illustrative analogue for the interference of transition paths. A double slit is placed between a screen and a coherent light source, such as a laser. The latter defines the initial state of the photons; their arrival at the screen corresponds to the final state. Because of the slits, the propagation is restricted to two paths, comparable to the two absorption paths of QUIC. If one slit is covered, only a single spot is visible on the screen[2]. Its shape is described by the respective intensity $|A_1|^2$ or $|A_2|^2$ of the transmitted light amplitude. However, these single-slit patterns may not simply be added if both slits are opened.

The coherent superposition of two light amplitudes propagating through different slits results in an additional phase-dependent term:

$$|A_1 + A_2|^2 = |A_1|^2 + 2\,\mathrm{Re}\left\{A_1\overline{A_2}\right\} + |A_2|^2 \tag{2.3}$$

If the relative phases of A_1 and A_2 are incorporated via exponential phase terms of the form $\exp(-\mathrm{i}\phi)$, the phase dependence becomes apparent: $2\,\mathrm{Re}\left\{A_1\overline{A_2}\right\} \propto \cos(\Delta\phi)$. Depending on whether the two light waves interfere constructively or destructively, the respective spot on the screen is illuminated or dark. As a result, the additional term $2\,\mathrm{Re}\left\{A_1\overline{A_2}\right\}$ manifests as interference pattern of parallel fringes. Similarly, the direction and amplitude of the coherently controlled current can be manipulated by the relative phase of the fundamental and second harmonic beam. Depending on the relative phase, there is an unequal number of carriers excited at $-k$ and $+k$.

In order to describe QUIC quantitatively, the groups of J. E. Sipe and H. M. van Driel developed a theoretical approach based on time-dependent perturbation theory [48]. This approach is sketched in the following whereby only essential steps are given. Lengthy expressions as well as calculations that do not substantially add to the general understanding of the derivation are omitted.

Initially, the electronic band structure, as depicted in Fig. 2.1(a), is calculated for a steady state electron distribution. Transitions by photon absorption are incorporated via time-dependent perturbation theory. In specific, the influence of an electromagnetic field is included with a semiclassical minimal coupling approach. "Semiclassical" refers to the fact that electrons are treated quantum-mechanically while the light is treated as a classical wave. Such an approach sufficiently describes the influence of a moderate electromagnetic field on the electronic states [28, ch. 2.3]. Second quantization of the light field would be necessary if the intensity is so low that single photon effects become relevant, an example of which is spontaneous emission. The opposite regime of high intensities and specifically its influence on QUIC is the subject of chapter 4.

[2]For simplicity, diffraction at a single slit is neglected.

To begin with, it is instructive to discuss the employed perturbation theory for a single electron in a crystal potential $U(\mathbf{r})$. Its time-independent Hamiltonian is given by

$$H_0 = \frac{1}{2m_\mathrm{e}}\mathbf{p}^2 + U(\mathbf{r}). \tag{2.4}$$

Here, m_e denotes the electron mass, $\mathbf{p}$ the momentum operator and $\mathbf{r}$ the position operator. Similar to classical electromagnetism, the interaction with an electromagnetic field is incorporated by a gauge transformation of the momentum operator $\mathbf{p}$, also known as minimal coupling [52, p. 130ff]:

$$\mathbf{p} \to \mathbf{p} - \frac{e}{c}\mathbf{A}(t) \tag{2.5}$$

With typical wavelengths in the order of micrometers and lattice constants in the order of nanometers and less, it is justified to employ the long-wavelength limit for the vector potential $\mathbf{A}(t)$. That is, the field amplitude is independent of the position operator $\mathbf{r}$. Consequently, magnetic effects can be neglected according to the relation $\mathbf{B} = \nabla \times \mathbf{A}$. The electric field is given by $\mathbf{E}(t) = -\dot{\mathbf{A}}(t)/c$. An electromagnetic wave with the angular frequency ω can therefore be described by the vector potential

$$\mathbf{A}(t) = \mathbf{A}(\omega)\exp(-\mathrm{i}\omega t) + \text{c.c.} \quad \text{with} \quad \mathbf{E}(\omega) = \mathrm{i}\,(\omega/c)\,\mathbf{A}(\omega). \tag{2.6}$$

After gauge transformation, the time-dependent Hamiltonian $H(t)$ can be further simplified by neglecting the term proportional to $\mathbf{A}^2$ since it does not substantially contribute to current injection [48]. Finally, the Hamiltonian $H(t)$ can be separated into the unperturbed term H_0 and a perturbation $V(t)$ that is linear in $\mathbf{p}\cdot\mathbf{A}(t)$:

$$H(t) = \frac{1}{2m_\mathrm{e}}\mathbf{p}^2 + U(\mathbf{r}) - \frac{e}{m_\mathrm{e}c}\,\mathbf{p}\cdot\mathbf{A}(t) = H_0 + V(t) \tag{2.7}$$

Solutions of the time-independent Hamiltonian H_0 are steady electron states. If the time-dependent perturbation $V(t)$ is small compared to H_0, it does not significantly alter the energy eigenvalues. However, according to time-dependent perturbation theory, $V(t)$ causes transitions between different states. In specific, the probability density $w_{i\to f}$ for a transition from the initial state i to the final state f can be calculated by Fermi's golden rule [52, ch. 5.6]. Applied to the absorption of a monochromatic wave (cf. equation 2.6), it is given by

$$w_{i\to f} = \frac{2\pi}{\hbar}\,|M_{fi}|^2\,\delta(E_f - E_i - \hbar\omega). \tag{2.8}$$

The delta distribution corresponds to the conservation of energy; M denotes the transition matrix element that is expanded in orders of the perturbation $V(t)$. For a first order calculation in Dirac notation, the matrix element is of the form $\langle f|\,V(t)\,|i\rangle$.

In order to apply these calculations on electrons in a semiconductor, the Hamiltonian

H_0 is expressed by Bloch states with crystal momentum $\mathbf{k}$. The respective energy eigenvalues correspond to the energy dispersion that is illustrated in Fig. 2.1(a). The coherent superposition of the fundamental and second harmonic field is modeled by the following vector potential, whereby ω is assumed to satisfy the energy relation $\hbar\omega < E_\mathrm{g} < 2\hbar\omega$:

$$\mathbf{A}(t) = \mathbf{A}(\omega)\exp(-\mathrm{i}\omega t) + \mathbf{A}(2\omega)\exp(-\mathrm{i}2\omega t) + \mathrm{c.c.} \tag{2.9}$$

One-photon absorption of the second harmonic field induces an electron transition from a state $|v\rangle$ in a valence band to a state $|c\rangle$ in the conduction band. As explained above, the respective matrix element $M_{cv}^{(1)}$ is of the form $\langle c|\, V(t_1)\, |v\rangle$. To account for two-photon absorption of the fundamental field, the second-order matrix element $M_{cv}^{(2)}$ of the form $\sum_i \langle c|\, V(t_1)\, |i\rangle \langle i|\, V(t_2)\, |v\rangle$ must be included. This matrix element can be interpreted as a transition via an intermediate state $|i\rangle$.

It is crucial to note that both matrix elements exhibit a different dependence on the velocity operator $\mathbf{v}$ as well as the electric field amplitudes $\mathbf{E}$. This follows from their different dependence on the perturbation $V(t)$ that is linear in $\mathbf{p}\cdot\mathbf{A}$. The momentum operator $\mathbf{p}$ is, in turn, proportional to the velocity operator $\mathbf{v}$. According to equation (2.6), the amplitudes of the vector potential are proportional to the electric field amplitudes. On the basis of these dependences, it is possible to derive the general functional form of QUIC.

The current injection rate depends on the carrier injection rate $\dot{n}$ and the respective electron velocity v which is given by the slope $\partial E(\mathbf{k})/\partial\mathbf{k}$. Since the slope is a function of the crystal momentum $\mathbf{k}$, the injection rate must be averaged over all states in the valence and conduction bands:

$$\frac{\mathrm{d}J}{\mathrm{d}t} \propto q \sum_{c,v,\mathbf{k}} \dot{n}_{c,v,\mathbf{k}} v_{c,v,\mathbf{k}} \tag{2.10}$$

The injection rate $\dot{n}$ is a linear function of the probability density $w_{v\to c}$ for transitions from a valence to the conduction band. It can be derived by inserting the sum of the first- and second-order matrix elements into Fermi's golden rule (2.8). Similar to Young's double slit experiment, the superposition results in an interference term:

$$w_{v\to c} \propto \left|M_{cv}^{(1)} + M_{cv}^{(2)}\right|^2 = \left|M_{cv}^{(1)}\right|^2 + 2\,\mathrm{Re}\left\{M_{cv}^{(1)}\overline{M_{cv}^{(2)}}\right\} + \left|M_{cv}^{(2)}\right|^2 \tag{2.11}$$

Because of its threefold dependence on $V(t)$, the interference term is the only term that is an odd function of the velocity. It corresponds to an anisotropic carrier generation as illustrated in Fig. 2.1(a). Inserted into equation (2.10), the interference term results in the only term that is an even function of the velocity. In contrast to the terms of the individual absorptions, it does not cancel out by the summation over the symmetric band diagram that corresponds to averaging over the velocity. It thus becomes evident that only the coherent superposition of both transitions is able to inject a current.

Based on the dependence on $V(t)$, it is further possible to derive the fundamental dependence of the current injection rate on the electric field amplitudes. The first- and second-order matrix elements are proportional to $E(2\omega)$ and $E(\omega)^2$, respectively. The complex conjugation in the interference term corresponds to an inversion of the frequency of one component (cf. equation (2.9)). For these reasons, the current injection rate should be of the form $E(\omega)^2 E(-2\omega)$.

An explicit calculation of the current injection rate confirms the predicted dependences:

$$\frac{\mathrm{d}J^a}{\mathrm{d}t} = \eta_3^{abcd}(\omega)\,\overline{E^b(\omega)}\,\overline{E^c(\omega)}\,E^d(2\omega) + \text{c.c.} \tag{2.12}$$

The fourth rank tensor $\eta_3^{abcd}(\omega)$ quantifies the relation between the current injection rate and the electric fields. It also describes the dependence of the current orientation on the polarization of the electric fields, which is neglected above. Both the differently orientated current components as well as the polarization components are denoted by superscripts in Einstein's notation. Furthermore, apart from the electron current, the tensor also contains the current contribution of holes.

If an anisotropic electron distribution in the conduction band is optically excited, there is a complementary distribution in the valence bands, as indicated in Fig. 2.1(a). Owing to the opposite slope of both depicted bands, electrons in the conduction band and holes in the valence band at the same crystal momentum move into opposite directions. Furthermore, their absolute velocities differ due to different effective masses. In specific, the effective electron mass in GaAs is $0.067 \cdot m_\mathrm{e}$ compared to an effective mass of $0.5 \cdot m_\mathrm{e}$ and $0.08 \cdot m_\mathrm{e}$ for the heavy and light hole band, respectively [47, p. 361; 53]. Therefore, the electron and light hole velocity significantly exceeds the velocity of heavy holes. However, since the effective mass also determines the density of states, light holes only account for a few percent of the total hole density at the band maximum [53]. In consequence, current injection is predominantly determined by the electron contribution [9; 48].

It can be demonstrated that η_3 is related to the imaginary part of the third-order susceptibility $\chi^{(3)}(0;\omega,\omega,-2\omega)$ [7; 54]. The explicit components of η_3 can be calculated via density functional theory. With regard to GaAs and a fundamental wavelength of 1550 nm – also used for experiments within the context of this thesis – the nonzero tensor elements are $\eta_3^{xxxx} = 2 \cdot \eta_3^{xxyy} = 2 \cdot \eta_3^{xyxy}$, $\eta_3^{xyyx} \ll \eta_3^{xxxx}$ and their equivalent permutations with x and y exchanged [7]. In this context, x and y denote directions along different crystallographic axes. Hence, if all polarizations are aligned along the same crystallographic axis, the current injection is at its maximum and directed along this axis. In this case, equation (2.12) can be further simplified. If the respective phases of the electric fields are incorporated via exponential terms of the form $\exp(-\mathrm{i}\phi)$, the explicit phase dependence of

QUIC becomes more obvious:

$$\frac{\mathrm{d}J^x}{\mathrm{d}t} \propto \left[E^x(\omega)\right]^2 E^x(2\omega)\sin(2\phi_\omega - \phi_{2\omega}) \tag{2.13}$$

For completeness, it should be mentioned that the time-dependent perturbation approach also yields other coherence control effects. Apart from charge current injection, the superposition of a fundamental beam and its second harmonic may be utilized to inject spin-polarized currents [55–58] or to control the carrier density in semiconductors [59; 60]. The former requires both beams to be orthogonally polarized; the latter only occurs if certain symmetry conditions are fulfilled with respect to the field polarizations and the lattice. Although counterintuitive at first glance, it is even possible to inject a charge current with only one elliptically polarized beam [51]. In this case, the two interfering absorption paths are addressed via different polarization components.

The theoretical approach demonstrates that QUIC fundamentally differs from conventional current generation via an external voltage. Most notably, QUIC is an all-optical process. Since transitions are induced at $\mathbf{k} \neq 0$, the excited carriers exhibit a nonzero velocity practically instantaneously without being accelerated by an external force. Under ideal conditions, the majority of electrons moves collectively in the same direction with an average velocity of about 500 km/s [48]. Hence, with the help of ultrashort pulse lasers, QUIC allows to generate highly directed current bursts with a duration of 100 fs and less. Moreover, the current can be injected at arbitrary spots with minimum diameters of only a few micrometers. In practice, the lower limit is mainly determined by focusing optics. As explained above, the current direction can be further manipulated by amplitude, phase and polarization of the electric fields.

The above mentioned features of QUIC are in striking contrast to current generation via an external field. First, the application of a voltage requires at least two electrical contacts that have to be defined beforehand. Second, if a voltage is applied to a semiconductor, the rise and fall time is limited by an *RC* constant. As evident from maximum CPU clock rates of a few GHz, the *RC* constant is usually at least in the order of picoseconds. Third, the underlying mechanism of current generation is fundamentally different. Without an external field, excess electrons reside at the band minimum in thermal equilibrium. An applied voltage causes a gradual acceleration of the electrons by displacing them in the Brillouin zone. The displacement can be thought of as a minor $\mathbf{k}$-shift of the electron distribution as a whole [9; 61, p. 120f]. However, only the small fraction of electron states that are not compensated by states with opposite $\mathbf{k}$ value contribute to the nonzero drift velocity.

QUIC provides a versatile tool to manipulate and study carrier dynamics on a short timescale with high spatial selectivity. It has been applied to a variety of material classes

as well as experimental concepts. Remarkably, QUIC could be demonstrated in silicon and germanium [14; 15]. Their indirect band gap is typically associated with a low optical response and it further requires a modification of the theoretical approach. Besides, QUIC was applied to graphene, which exhibits a linear dispersion with a vanishing band gap [16], the topological insulator Bi_2Se_3 [17] and copper [18]. By tightly focusing the input beams, it was possible to efficiently inject currents into carbon nanotubes [20; 21] and even single GaAs nanowires [22]. The spatial selectivity of QUIC can even extended beyond the diffraction limit with the help of lithographically defined nanoantennas that result in a local field enhancement [62].

Besides studies of electron transport, QUIC can also be used for other applications. Because of the ultrashort rise and fall time, the injected current acts as a source for terahertz radiation. In fact, terahertz measurements are an established method to detect QUIC [14; 15; 19–21; 63]. Furthermore, the explicit phase dependence of QUIC has been utilized for measurements of the carrier-envelope phase of a pulse train [25; 26] and phase-resolved material spectroscopy [23; 24]. An advanced interferometric technique that allows to reconstruct the spectral phase of the input laser pulses is demonstrated in chapter 5. Chapter 6 discusses the experimental implementation of a proposed QUIC-based optical current detection technique.

Chapter 3

Experimental Methods

The thesis covers three different aspects of QUIC. Despite their different specific requirements, the setups are based on the same experimental concept that is outlined in the present chapter. In this context, it is instructive to recall equation (2.12) that describes the current injection:

$$\frac{\mathrm{d}J^a}{\mathrm{d}t} = \eta_3^{abcd}(\omega)\,\overline{E^b(\omega)}\,\overline{E^c(\omega)}\,E^d(2\omega) + \text{c.c.} \tag{3.1}$$

Because of the threefold dependence on the electric field amplitudes, QUIC scales nonlinearly with the total irradiance. Hence, the requirement of ultrashort pulse lasers is obvious: In contrast to conventional lasers which emit a continuous beam, the energy is concentrated in ultrashort pulses resulting in high peak intensities. Here, the term "ultrashort" particularly refers to pulse durations in the order of 100 fs or less. The employed laser systems are addressed in chapter 3.1.

Apart from their high peak intensities, ultrashort pulses also allow to perform time-resolved measurements in a pump-probe scheme [64, ch. 9]. A material's response to a first pulse is detected via transmission or reflection of a second pulse with variable delay. The temporal resolution of such a measurement is determined by the pulse length, comparable to the temporal limitation of a photography by the shutter speed of the camera.

QUIC requires laser pulses of different wavelengths, a fundamental beam with the angular frequency ω and its second harmonic with the frequency 2ω and twice the photon energy. Furthermore, the relative delay of the pulses must be precisely controllable to resolve the phase dependence of QUIC. For this purpose, the second harmonic beam is generated by the fundamental beam itself, and subsequently the beams are split up in an interferometer. Finally, the beams are focused onto a contacted sample of low-temperature grown GaAs (LT-GaAs) wherein QUIC takes place. The interferometric setup is described in more detail in chapter 3.2. Chapter 3.3 addresses QUIC in LT-GaAs as well as the measurement procedure. All experiments are performed at ambient conditions ($T = 300$ K).

3.1 Ultrashort Pulse Laser Systems

The experiments presented in the following chapters mainly employ two commercially available ultrashort pulse laser systems: The compact fiber laser *FemtoFiber Scientific* (FFS) of *TOPTICA Photonics* and the optical parametric amplifier *OPA 9850* (OPA) of *COHERENT*. In fact, the latter is only the last stage of a laser system that is seeded by a titanium-sapphire laser.

The FFS features two synchronized outputs with an average power in the order of 200 mW. Each output emits about 100 fs-wide linearly-polarized pulses at a repetition rate of 75 MHz. The central wavelength is fixed at about 1550 nm.

The OPA allows to tune the wavelength in a range from 1200 nm to 1600 nm. Depending on the wavelength, the average power is in the order of a few tens of milliwatts. The linearly-polarized pulses exhibit a width of about 50 fs and a repetition rate of 250 kHz.

Both laser systems rely on passive modelocking techniques to generate femtosecond pulses [28, ch. 8.3]. First, an active medium with a broad gain spectrum is required. The minimum pulse width is inversely proportional to the spectral width as evident from the Fourier transform of a Gaussian wave packet (cf. chapter 5.1). Second, it must be ensured that all spectral components are in phase, also called mode-locked. A random phase distribution would result in a temporal shift of the components and causes the pulse to broaden. In practice, passive modelocking is achieved with a mechanism that favors high peak intensities on the basis of nonlinear optical effects.

The FFS utilizes nonlinear intensity-dependent polarization rotation in an erbium-doped fiber [65] that simultaneously acts as active medium. Upon propagation through the fiber, light components with high peak intensities acquire a different polarization and are preferably transmitted by additional polarization optics. The latter and the fiber are arranged as a ring resonator. Starting with noisy continuous-wave emission, the intensity peaks are amplified with every pass until only one ultrashort pulse circulates. It is partly outcoupled, further amplified and directed to the two outputs.

The seed laser of the OPA system employs another modelocking technique. The active medium, a titanium-doped sapphire crystal, is placed in a resonator formed by a high reflective mirror and a semitransparent output mirror. Because of the optical Kerr effect, the refractive index of the active medium changes significantly at high peak intensities [28, p. 218]. Therefore, the laser beam experiences intensity-dependent focusing. By an appropriate arrangement of the focusing optics in the resonator, round-trip losses of low-intensity components are higher than for high-intensity components. Thus, the laser favors the propagation and gain of ultrashort pulses with high peak intensities. After further amplification, the pulses of the titanium-sapphire laser are seeded into the OPA.

Utilizing frequency mixing, the OPA allows to tune the wavelength [27, p. 884ff]. A

portion of the input "pump" pulse is used to generate a white-light continuum via nonlinear processes in a sapphire crystal. Subsequently, the pump pulse and the continuum are superimposed in a beta barium borate (BBO) crystal. Only a specific spectral component of the continuum for which the phase matching condition is fulfilled, the "signal" beam, contributes to frequency mixing. Phase matching and thus the selected wavelength can be conveniently adjusted by rotating the crystal. In turn, the crystal generates a pulsed beam, the "idler", with a wavelength given by the energetic difference of the pump and the signal component. Furthermore, the signal beam is amplified by the high power pump beam during this process. In the experiments presented here, only the signal beam with the above mentioned wavelength range is used.

The choice of wavelengths for QUIC in semiconductors is determined by the energy relation $\hbar\omega < E_{\mathrm{G}} < 2\hbar\omega$. With a room-temperature band-gap of 1.42 eV [66, p. 412; 53], this condition is conveniently fulfilled for GaAs and a fundamental wavelength in the commercially used telecom range around 1.5 µm. In fact, the widespread availability of pulsed laser sources in the telecom range and thus the simple room temperature application of QUIC triggered the initial choice of GaAs [48]. A wavelength of 1.55 µm corresponds to a photon energy of 0.8 eV. Consequently, two-photon absorption of the fundamental beam as well as one-photon absorption of the second harmonic beam in GaAs result in an excess energy of 180 meV.

3.2 Interferometric Setup

The main purpose of the interferometric setup, sketched in Fig. 3.1, is to generate the second harmonic beam from the fundamental beam and to control both beams in intensity, polarization and phase. Previously, the laser output is directed into a telescope consisting of two lenses. By adjusting their relative position, it is possible to minimize beam divergence that may otherwise disturb the measurements.

To ensure phase stability, the second harmonic beam is derived from the fundamental beam via SHG. For this purpose, the fundamental beam is focused into a nonlinear crystal. In particular, either beta barium borate (BBO) or bismuth borate (BiBO) is used. With crystal thicknesses in the order of a millimeter and a fundamental wavelength around 1.5 µm, both laser systems are able to generate several milliwatts of an orthogonally polarized second harmonic beam. The orthogonal polarization is a result of the crystal's birefringence and the phase matching condition that has to be fulfilled [28, ch. 15.4]. A second lens behind the crystal collimates both beams that propagate collinearly into the subsequent interferometer.

The beams are individually manipulated in a Michelson interferometer featuring one arm for each color. A dichroic beamsplitter transmits the fundamental beam and reflects

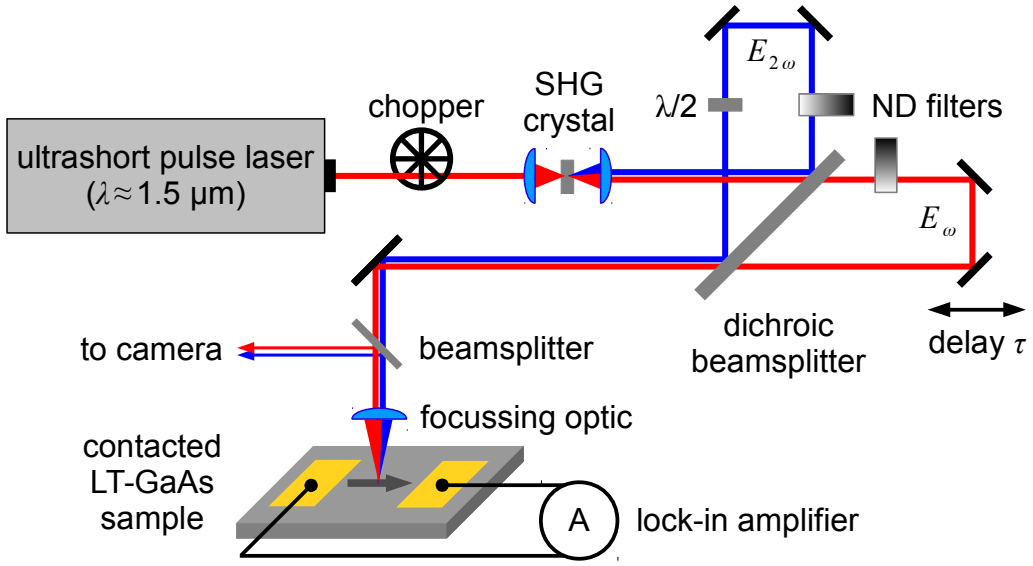

Fig. 3.1: Prototypical experimental scheme for the realization and detection of QUIC in LT-GaAs: A nonlinear crystal is used to generate the second harmonic of the output of an ultrashort pulse laser. The individual intensity, the polarization and the relative phase of the two beams can be controlled in a two-color interferometer. Both beams are collinearly focused on a contacted LT-GaAs sample at room temperature with a typical contact gap width in the order of 10 µm. The induced current is recorded with a lock-in amplifier which is referenced to a chopper wheel placed at the laser output. A beamsplitter in front of the focussing optic redirects the reflections of the sample to a camera that allows to monitor the focal spots on the sample.

the second harmonic beam. Further filters in the arms, a low- and a high-pass filter, ensure an effective separation of both harmonics. Retroreflectors are placed at equal distance in both arms, so that the beams are recombined on the same beamsplitter. While the retroreflector of the second harmonic arm is fixed, the retroreflector of the other arm is mounted on a motorized stage.

In order to resolve the phase dependence of QUIC, the relative phase of both beams must be controlled on a subwavelength scale. For that purpose, a computer-controllable linear motor stage of the *XM* series by *Newport* is used. The stage is specified with a uni-directional repeatability of 50 nm at a travel range of 50 mm[1]. The overall arm lengths are kept as short as possible to minimize phase distortion of the individual beams, for example by air turbulences or vibrations. The minimum length is limited by additional optical elements that are placed into the arms; it is typically in the order of 20 cm.

Apart from phase, QUIC depends on the intensity and polarization of the beams. Half-wave plates in the interferometer allow to adjust the relative polarization of both beams and ultimately to address specific elements of the current injection tensor η_3. In particular,

[1]In comparison, a 100 fs delay corresponds to a stage movement of 15 µm.

the beams' orthogonal polarization that results from SHG must be altered to address the largest element η_3^{xxxx}. The beam intensity is set individually via neutral density filter wheels (ND filters) with variable attenuation. In this way, unintentional phase shifts, that would otherwise result from the exchange of different filters with a fixed attenuation, are prevented.

Before both beams are focused onto the LT-GaAs sample, it must be ensured that they propagate collinearly. Otherwise their phase relation would vary across the beam width and current injection would be reduced. To this end, both beams can be redirected through a separate thin nonlinear crystal onto a camera. The nonlinear crystal generates another second harmonic beam from the fundamental beam. The resulting interference pattern of both second harmonic beams on the camera is a direct measure for collinearity.

Efficient current injection further requires appropriate focusing to enhance the illumination intensity. For this reason, the reflected light from the sample is redirected onto another camera by a beamsplitter in front of the focusing optic. The camera allows to monitor the focal spot and its relative position on the LT-GaAs sample. Moreover, the size and relative position of the beams' focal spots can directly be measured by replacing the sample with a beam profiler. The beam profiler scans a laser beam with a movable slit and automatically calculates its spatial width.

3.3 QUIC in LT-GaAs

The presented QUIC measurements rely on the detection of the induced charge separation via metallic contacts on top of the sample. The sample itself typically consists of a few micrometer thick epilayer of low-temperature grown GaAs (LT-GaAs) on an intrinsic GaAs substrate. Its lateral size is in the order of a few millimeters. LT-GaAs has proven superior to intrinsic GaAs for such a detection scheme [8; 9]. Essentially, defect states in LT-GaAs preserve the charge separation and thus the voltage that would otherwise equilibrate rapidly after optical excitation [67].

As depicted in Fig. 3.1, the collinear excitation beams are focused onto the gap of a metallic contact pair. It is defined via optical lithography and metallic evaporation, typically titanium and gold with a thickness in the order of 100 nm. A gap size in the order of the beam width that determines the charge separation, typically a few tens of micrometers, ensures a high detection efficiency. The sample is glued into a chip carrier and contacted with bond wires to facilitate convenient current measurements via macroscopic electrical connectors. Furthermore, the chip carrier is mounted on a micro-positioner for precise alignment. The measurement procedure itself employs lock-in technique and is explained at the end of this chapter. In the following, a more detailed description of QUIC in LT-GaAs is given.

LT-GaAs is grown by molecular beam epitaxy (MBE) at a substrate temperature of 200 °C to 400 °C [68]. This is well below the typical temperature of about 600 °C for stoichiometric growth of GaAs. Excess arsenic atoms form defects in LT-GaAs, mainly by substituting gallium atoms (antisite defects) or by occupying additional sites in the lattice (interstitial defects). Thermal annealing at about 600 °C rearranges the defects and restores the lattice constant to a relaxed state.

Concerning QUIC, it is sufficient to describe the defect states in LT-GaAs by an additional band approximately in the middle of the band gap [69; 70]. A simplified band diagram is depicted in Fig. 3.2. Since individual defect states have a low conductivity due to their spatial separation, the illustration as a continuous band must be treated with caution. Concerning photon energies that exceed the band gap by about 100 meV or more, the optical properties of LT-GaAs and intrinsic GaAs do not significantly differ [9]. With a linear absorption coefficient of $1.5 \cdot 10^4$ cm^{-1} for 775 nm, the second harmonic beam is fully absorbed in the LT-GaAs layer. Therefore, the following discussion of QUIC focuses on LT-GaAs.

Fig. 3.2 depicts the electron distribution in the band diagram of LT-GaAs for different time scales during the current injection process. Furthermore, a top view of the

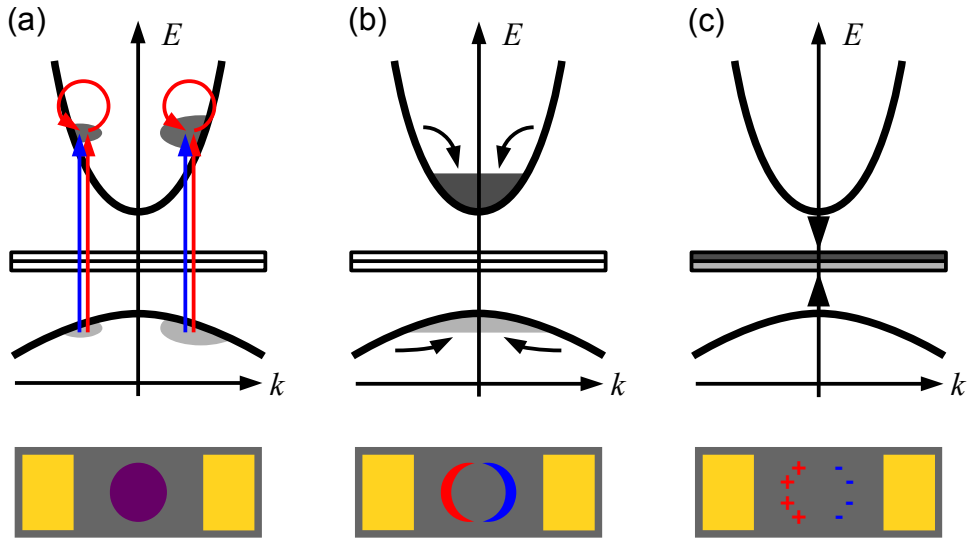

Fig. 3.2: Schematic temporal evolution of the carrier distribution during and after current injection in LT-GaAs. The upper panels illustrate the occupation in a simplified band diagram; the states in the middle of the band gap represent defects. The lower panels depict the spatial carrier separation in the sample that is measured via two metallic contacts. (a) The coherent absorption of a fundamental wave and its second harmonic generates an asymmetric carrier distribution that results in a current flow. (b) After injection, the carriers quickly thermalize and the current decays. Electrons and holes are spatially separated because of their different velocities. (c) Carriers are trapped within defect states and a frozen electronic dipole remains that can be detected via metallic contacts.

LT-GaAs and the adjacent metal contacts illustrates the spatial charge separation. First, in Fig. 3.2(a), a pulse pair consisting of an infrared fundamental pulse as well as its second harmonic impinges on the LT-GaAs surface between the metal contacts. The respective one- and two-photon absorption correspond to a transition energy of about 1.6 eV. As explained in chapter 2.2, the interference of absorption paths results in an asymmetric carrier distribution that manifests as current flow. Determined by the slope of the dispersion, the electron and hole distribution move into opposite directions and a spatial charge separation forms. The duration of current injection is determined by the pulse length, in the context of the presented measurements about 100 fs.

Subsequent to injection on a time scale of about 100 fs, the current declines by inelastic scattering, e.g. electron-phonon or impurity scattering [9; 48; 71; 72]. In terms of the band diagram, such a thermalization corresponds to a relaxation of the carriers to the center of the band, as depicted in Fig. 3.2(b). With an average electron velocity of several 100 km/s, individual electrons may only move a few tens of nanometers [48; 67]. However, the collective injection in the focal spot results in a carrier separation given by the beam widths [67]. The injected electron and hole distributions overlap in the middle of the illuminated area and can directly recombine. At opposing edges of the area, there is a local excess of electrons and holes which form an electronic dipole. These opposing charges attract each other by Coulomb forces that would eventually neutralize the dipole. In a first approximation, the charge dynamics can be described by a rigid shift model with a neutralization time of about 1 ps, given by the density-dependent plasma frequency [67]. Consequently, the electron dipole is hardly measurable in intrinsic GaAs [9].

Utilizing defect states in LT-GaAs, see Fig. 3.2(c), the carriers are trapped and the dipole can be frozen before it neutralizes. The respective carrier trapping time is about 1 ps or even less [70; 72–74]. In comparison, the carrier lifetime in intrinsic GaAs is at least in the order of nanoseconds [75]. Owing to the spatial separation of defect states in LT-GaAs, the carriers are immobilized. Moreover, the recombination to the valence bands is hindered as there are few empty states; the current flow has caused a local excess of carriers. Only a low hopping-conductivity or thermally excited carriers may cause a long-time neutralization of the dipole.

The long-lived electronic dipole induces charges in the metallic Schottky contact pair. In turn, a measurable compensating current flows if both contacts are connected. Because of the defects, LT-GaAs should have a lower Schottky barrier as well as a lower resistivity than GaAs [68; 76, ch. 3.6]. The measurements on LT-GaAs presented in the following chapters feature average currents of up to a few nanoampere. Taking the pulse width and the repetition rate of the laser into account, the average current amounts to a remarkable peak current injection. For example, an average current of 1 nA injected by 100 fs pulses at a repetition rate of 75 MHz corresponds to a peak current of about 100 µA. What is more,

the calculated peak current only constitutes a lower limit since the extraction efficiency of the contacts as well as the amplitude of internal compensating currents in the sample are unknown.

Lock-in technique is used to measure these currents as low as a few picoampere. The laser output is periodically blocked by a chopper wheel with a frequency of a few 100 Hz. In essence, a lock-in amplifier that is connected to the sample only records current components which are modulated by such frequency. Noise and disturbing signals at other frequencies, e.g. from the power grid at multiples of 50 Hz, are suppressed.

The experiments in the following chapters require phase resolved measurements of QUIC. To this end, current interferograms as exemplarily depicted in Fig. 3.3(a) are recorded. The average current is plotted against the relative delay τ between the fundamental and second harmonic pulses. A constant offset that may result from phase-independent photocurrents of the illuminated metal-semiconductor junction is subtracted. In practice, the interferograms consist of subsequent current measurements with a stepwise length increment of one interferometer arm. A typical increment of about 40 nm corresponds to a temporal resolution of 0.3 fs and is sufficient to resolve the phase dependence (see Fig. 3.3(b)).

Current interferograms correspond to a convolution of the electric field components of the laser beams which are incident on the sample. The temporal dependences of the

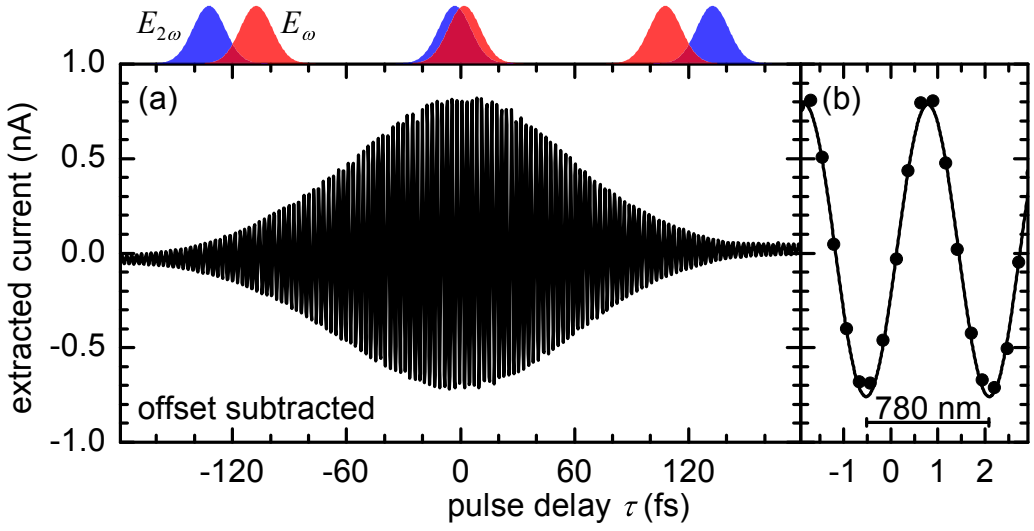

Fig. 3.3: (a) Exemplary current interferogram taken with the fiber laser FFS: Plot of the recorded current injection in LT-GaAs as a function of the relative delay τ between the impinging fundamental and second harmonic laser pulses. Their relative timing is illustrated in the top. A constant current offset is subtracted. The graph resembles a convolution of the pulse envelopes modulated by a carrier wave. (b) The closeup around $\tau = 0$ illustrates the temporal resolution of the measurement and the phase dependence of QUIC which manifests as oscillation.

respective electric fields read $E_\omega(t-\tau)$ for the fundamental beam in the variable arm and $E_{2\omega}(t)$ for the second harmonic beam in the fixed arm. Average current measurements translate into a time-integration of the current injection rate (2.12). Omitting the complex conjugated term for clarity, the resulting current relation reads:

$$I(\tau) \propto \int \dot{J}(t,\tau)\,\mathrm{d}t \propto \int \left[\overline{E_\omega(t-\tau)}\right]^2 E_{2\omega}(t)\,\mathrm{d}t \tag{3.2}$$

The current interferogram $I(\tau)$ displayed in Fig. 3.3(a) resembles a Gaussian envelope modulated by a carrier wave. It results from the phase-dependent convolution of Gaussian-like pulses. For illustration, their relative delay is sketched in the top of the figure. When the relative delay τ between the pulses is swept, the injected current periodically changes its direction and amplitude due to the explicit phase dependence of QUIC. In accordance with the phase dependence $\sin(2\phi_\omega - \phi_{2\omega})$ of the injection rate (2.13), the current oscillates with a temporal oscillation period that corresponds to the frequency of the second harmonic beam. The inset 3.3(b) exemplarily shows this carrier wave around $\tau \approx 0$.

The envelope of the current interferogram is given by the temporal overlap of the pulses. On the far left and right side in Fig. 3.3(a), the pulses are significantly delayed with respect to each other and there is consequently almost no current injected. The current increases with the pulses' temporal overlap. It reaches its maximum if both pulses impinge simultaneously on the sample.

As stated in the beginning, this chapter describes a prototype setup for measurements of QUIC in LT-GaAs. The following individual experiments require specific modifications that are elucidated in the respective chapters. For example, chapter 5 relies on a three-beam interferometer. Chapter 6 focuses on the pulse transmission through the sample rather than the resulting current injection.

Chapter 4

QUIC Beyond the $\chi^{(3)}$ Model

The initial theoretical model of QUIC is based on a time-dependent perturbation approach which effectively translates into a $\chi^{(3)}$ description, see chapter 2.2. With respect to the electric field amplitude E and relative phase ϕ of the exciting laser pulses, the power scaling is given by $\mathrm{d}J/\mathrm{d}t \propto E_\omega^2 E_{2\omega} \sin(2\phi_\omega - \phi_{2\omega})$. In essence, the scaling stems from interference of two transition paths, namely two-photon absorption of fundamental laser pulses and one-photon absorption of their second harmonics.

Theoretical studies of QUIC in one- and two-dimensional structures predict significant deviations of this $\chi^{(3)}$ picture at elevated excitation intensities due to higher-order effects, e.g. Pauli blocking of the optically addressed states [39–42]. Specifically, saturation effects and even the influence of Rabi oscillations are expected. The experimental accessibility of this regime is rather unexplored to date despite the ready availability of high-intensity ultrashort laser sources. Although previous experimental studies already observed deviations of the power scaling [8; 9; 19; 48], these were mainly attributed to carrier dynamics following the injection and not investigated in more detail.

In the following, an extensive study of QUIC in GaAs in the high-intensity regime is presented. The current injection in contacted LT-GaAs samples is experimentally investigated with respect to its irradiance scaling and temporal behavior. These measurements, presented in chapter 4.2, are supported by numerical simulations of QUIC in bulk GaAs under realistic experimental conditions. Therefore, the simulations allow to quantitatively assess the experimental accessibility of the high-intensity regime in which the $\chi^{(3)}$ picture breaks down. The simulation results as well as the underlying theory are briefly summarized in chapter 4.1. Finally, both the numerical as well as experimental findings are discussed regarding the origin of the observed deviations. Apart from mechanisms during injection, the discussion also includes the influence of the measurement process and the carrier dynamics that follow the injection.

Parts of the results that are presented within this chapter have already been published in references [43; 44] and are in preparation for publication elsewhere [46].

4.1 Numerical Simulations

The study of QUIC at high excitation intensities is supported by numerical simulations performed by Huynh Thanh Duc and Torsten Meier from the Ho Chi Minh City Institute of Physics and the University of Paderborn, respectively. In the present chapter, the simulation results as well as the underlying model are briefly summarized. A detailed description can be found in reference [44]. The numerical and experimental results are both discussed in chapter 4.3.

In contrast to the perturbative approach of QUIC that is discussed in chapter 2.2, the following simulations represent numerically exact solutions of multiband semiconductor Bloch equations. These equations specifically describe the light-matter interaction of semiconductors even in the nonlinear regime [77, ch. 12]. In particular, the simulations presented here follow the theoretical approach that has been previously applied by Duc, Meier *et al.* to analyze the temporal behavior of QUIC and predict deviations from the perturbative theory [39–42]: Simulations for one- and two-dimensional structures revealed a highly nonlinear behavior at elevated excitation intensities, e.g. in the form of saturation effects. These saturation effects are attributed to Pauli blocking of the optically addressed states and a field-induced redistribution of the carrier distribution. Ultimately, even an influence of Rabi oscillations on QUIC is predicted.

In order to quantitatively compare the simulations with the measurements in the following chapter and assess the experimental accessibility of the high-intensity regime, a realistic three-dimensional approach is required. To this end, the band structure of room-temperature bulk GaAs is calculated via a 14 band $\mathbf{k}\cdot\mathbf{p}$ theory [77, ch. 3.3]. The light-matter interaction is incorporated into the semiconductor Bloch equations via the minimal coupling Hamiltonian $H_\mathrm{I} \propto \mathbf{A}\cdot\mathbf{p}$ (cf. chapter 2.2). Furthermore, relaxation and dephasing of the carrier distribution are both treated phenomenologically with a typical decay time of 150 fs. As a consequence, carrier-carrier scattering is not explicitly included in the simulations.

The vector potential $\mathbf{A}(t)$ is derived from the electric field $E(t)$ of the superimposed fundamental and second harmonic laser pulses. These are described by plane waves with a Gaussian temporal envelope and a central frequency of ω and 2ω that correspond to a photon energy of 0.8 eV and 1.6 eV, respectively:

$$E(t) = E_\omega \exp\left(-t^2/2\tau_L^2\right)\cos\left(\omega t + \phi_\omega\right) + E_{2\omega}\exp\left(-t^2/2\tau_L^2\right)\cos\left(2\omega t + \phi_{2\omega}\right) \tag{4.1}$$

Here, $E_{\omega/2\omega}$ denotes the electric field amplitude of the pulses, $\phi_{\omega/2\omega}$ their relative phase and τ_L their width that is set to 100 fs for both pulses.

The temporal evolution of the injected current density $J(t)$ at $T = 300$ K is derived by integrating the calculated asymmetric carrier distribution weighted by the corresponding

momentum. In order to extract the maximum current, the relative phase of both electromagnetic waves is set to $\pi/2$. Fig. 4.1 depicts the injected current density 100 fs after the pulse maximum as a function of the fundamental field amplitude E_ω for different fixed field amplitudes of the second harmonic pulse $E_{2\omega}$. The covered intensity range is specifically chosen to match the intensities of the measurements presented in chapter 4.2.

In essence, the numerical simulations predict marked deviations from the perturbative approach in an experimentally accessible regime. As long as the fundamental field amplitudes are low enough, the curves follow the perturbative $\chi^{(3)}$ scaling $\mathrm{d}J/\mathrm{d}t \propto E_{2\omega}E_\omega^2$. Empirical parabolic fits are added to the graph for illustration. If the fundamental field amplitude exceeds 1 MV/cm, the numerically simulated current densities are significantly below the perturbative expectation and begin to saturate. A similar behavior is observed in the experimental study of QUIC in the high-intensity regime which is presented in the following chapter. A detailed discussion of both the numerical and experimental results concerning the underlying processes that cause the deviations is given in chapter 4.3.

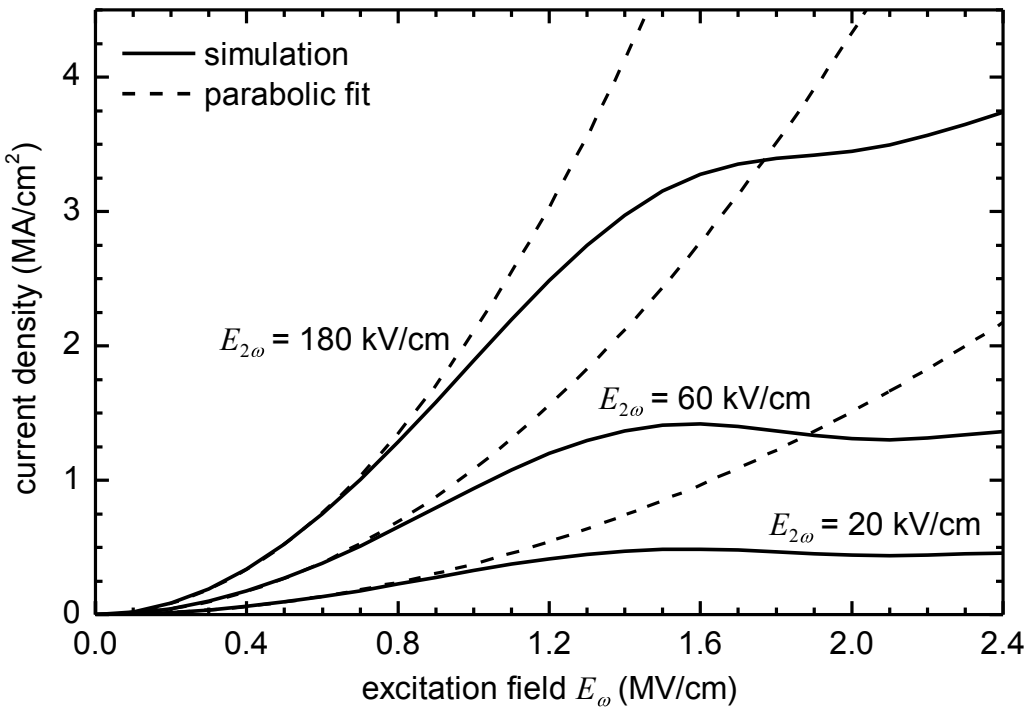

Fig. 4.1: Simulated density of injected currents in room-temperature GaAs 100 fs after the pulse maximum. The density is plotted against the electric field amplitude of the incident fundamental pulses for fixed amplitudes of the second harmonic pulses. Empirical parabolic fits illustrate deviations from the scaling of the perturbative $\chi^{(3)}$ model.

4.2 Experimental Study

The following chapter focuses on the experimental study of QUIC in the high-intensity regime. After a short introduction of the experimental setup, the dependence of the absolute current injection amplitude on the intensity of the exciting laser pulses is presented. Similar to the numerical simulations, it features marked deviations from the perturbative theory of QUIC. Additional time-resolved measurements allow to investigate the observed saturation effects and their underlying mechanisms in more detail.

Experimental Setup

The experimental setup that is mainly used to investigate QUIC in the high-intensity regime is similar to the setup which is described in chapter 3.2 and depicted in Fig. 3.1. A nonlinear crystal generates the second harmonic beam from the fundamental beam. Both beams are split up in a two-color interferometer that allows to manipulate the relative delay, the individual power and polarization of the pulses. Subsequently, the beams are collinearly focused onto a contacted LT-GaAs sample. Currents that are induced in a metallic contact pair are measured via a lock-in amplifier.

Special attention is paid to provide high and reproducible excitation intensities in the sample. Apart from strong focusing, this requires both beams to be precisely characterized as well as aligned on the sample. In this way, the excitation intensities can be assessed numerically allowing for a quantitative comparison with the simulations presented in chapter 4.1.

The measurements predominantly rely on the FFS fiber laser because of its long-term stability regarding output power as well as beam alignment. For this reason, the following description focuses on the specific setup of the fiber laser. However, additional measurements with the OPA laser system are also performed and addressed later in this chapter. The fiber laser provides 90 fs-wide pulses with a central wavelength of 1550 nm and a repetition rate of 75 MHz. An average output power of about 250 mW is able to generate more than 10 mW of second harmonic power via a 2 mm thick BiBO crystal. Owing to multiple reflections and absorption, e.g. by additional filters or polarization optics in the interferometer, the respective beam powers amount to a maximum of 80 mW for the fundamental beam and 8 mW for the second harmonic beam in front of the focusing lens of the sample.

An aspheric focusing lens with a focal length of 11 mm and a numerical aperture of 0.26 is used to achieve high excitation intensities in the sample. The resulting focal spot diameters are about 10 µm for the fundamental beam and 20 µm × 35 µm for the second harmonic beam. Differences in spot size and the asymmetry of the second harmonic beam result from chromatic aberration of the lens as well as anisotropy of SHG. These spot sizes

are measured by a beam profiler that is placed at the position of the LT-GaAs sample during adjustment. The beam profiler further allows to ensure that both beams propagate collinearly and their focal spots overlap.

The alignment of the focal spots is monitored via a camera that collects the reflected light of the sample surface with a beamsplitter in front of the focusing lens (cf. Fig. 3.1). Although the wavelength of the fundamental beam is beyond the detection range of the camera, the focal spot can still be observed by luminescence of the LT-GaAs sample. Electrons that are excited via two-photon absorption or from the defect states relax to the band minimum and recombine across the band gap. The corresponding emitted wavelength of about 870 nm can be detected by the camera. In fact, the luminescence is only detectable if the sample surface is positioned in the focal plane, making it a viable method for sample alignment.

If not stated otherwise, the following measurements are performed with a sample that consists of a 2 µm thick epilayer of LT-GaAs on top of an intrinsic (100) oriented GaAs substrate. The LT-GaAs layer was grown by molecular beam epitaxy well below the temperature for stoichiometric growth and afterwards annealed at about 600 °C. Metallic contacts on top of the LT-GaAs were defined by optical lithography and subsequent vapor deposition of titanium and gold. Two separate contacts with opposing parallel edges form a contact pair with a gap width of 50 µm (cf. Fig. 3.1). Finally, the sample was glued into a chip carrier and contacted via bond wires. These sample preparation steps were performed in the group of A. W. Holleitner at the Technische Universität München.

Intensity Dependence of the Current Injection Amplitude

As a first approach, the irradiance scaling of the time-integrated current injection is experimentally investigated. To this end, the maximum amplitude of current interferograms is extracted for different intensity combinations of the fundamental and the second harmonic beam. To ensure maximum intensity, the sample is placed into the focal plane with the above mentioned spot dimensions. Influence of parasitical illumination effects of the metal-semiconductor junction [25; 78] are minimized by positioning the focal spots exactly in the middle of the contact gap that exceeds the spot size. The polarization plane of the fundamental and second harmonic beam are both aligned along the width of the gap. In this way, the measurement probes the largest tensor element η_3^{xxxx}. For practical reasons, the sample is slightly tilted to reduce back reflections into the laser that may distort its operation.

Fig. 4.2 depicts the results of the current measurement series. The maximum current amplitude is plotted against the fundamental beam intensity for three exemplary fixed intensities of the second harmonic beam. Each data point corresponds to a measurement

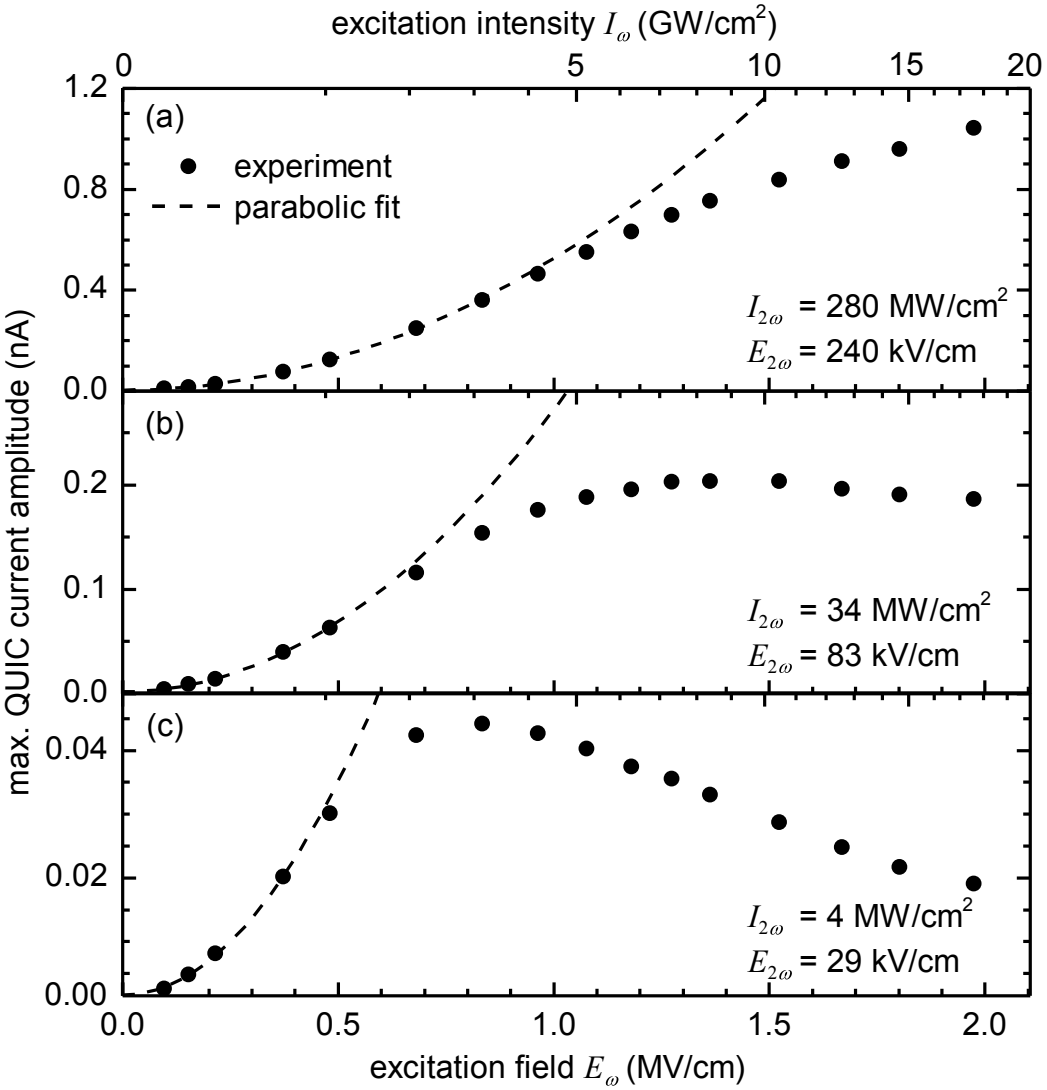

Fig. 4.2: Extracted maximum current amplitudes of QUIC in room-temperature LT-GaAs for different intensity combinations of the incident fundamental and second harmonic laser pulses. Each data point is derived from the oscillation amplitude of a current interferogram recorded around maximum pulse overlap (cf. Fig. 3.3) with the fiber laser setup. Empirical parabolic fits illustrate deviations from the scaling of the perturbative $\chi^{(3)}$ model.

of a current interferogram (cf. Fig. 3.3). In specific, the current values are extracted from the amplitude of the current oscillation at maximum pulse overlap (in Fig. 3.3 at $\tau \approx 0$). As already stated, the absolute current magnitude depends on a variety of parameters whose determination is beyond the scope of this thesis. In order to quantitatively analyze the functional dependence of current injection, the abscissa denotes the calculated peak amplitudes of the electric field. Corresponding peak intensities of the beams are also shown in the top scales. Both quantities are derived from the measured average beam power P_{avg}.

In order to calculate the peak intensity of the pulses, their temporal and spatial intensity distributions are approximated by simplified functions. The Gaussian-like temporal envelope is modeled by a step function. Its temporal width is determined by the FWHM t_{p} of the laser pulse. The spatial intensity distribution is approximated by a homogeneously illuminated ellipse. Its axes correspond to the $1/e$-widths of the actual intensity distributions. The latter are derived from the above mentioned beam profiler measurements. These yield the $1/e^2$-widths a and b that are related to the ellipse area A via $A = a \cdot b \cdot \pi/8$. In this case, the approximated focal spot areas amount to $A_\omega \approx 44\ \mu\mathrm{m}^2$ for the fundamental beam and $A_{2\omega} \approx 260\ \mu\mathrm{m}^2$ for the second harmonic beam.

The temporal width of the fundamental beam is determined via intensity autocorrelation (see also chapter 5.1). In a first approximation, the fundamental and second harmonic beam are both assigned the same FWHM of $t_{\mathrm{p}} \approx 90$ fs. Although the second harmonic pulses should be shorter than the fundamental pulses, the smaller central wavelength is more susceptible to dispersion, e.g. by the focusing lens, which in turn causes pulse broadening (see also chapter 5.1). Besides, it has to be taken into account that the fiber laser emits pulses with a repetition rate of $f_{\mathrm{rep}} = 75$ MHz. Owing to reflection losses at the lens as well as the sample surface, the average power in front of the focusing lens is corrected by a transmission factor of $T \approx 0.6$. Taken all together, the peak intensity I can be derived from the average beam power via

$$I = \frac{P_{\mathrm{avg}} T}{t_{\mathrm{p}} f_{\mathrm{rep}} A}. \tag{4.2}$$

In a next step, the peak amplitude E of the electric field is derived from the peak intensity. With respect to propagation of an electromagnetic wave in a material with refractive index n, both quantities are related via the Poynting vector [27, p. 165f]:

$$I = \frac{\epsilon_0 c_0 n}{2} |E|^2 \tag{4.3}$$

Here, ϵ_0 and c_0 denote the vacuum permittivity and the speed of light in vacuum, respectively. The refractive index n of GaAs amounts to 3.4 for the fundamental wavelength of 1550 nm and 3.7 for the second harmonic wavelength of 775 nm [9, and references within]. In the case of the fiber laser setup, the calculated excitation peak field amplitudes reach up

to $E_\omega = 2$ MV/cm and $E_{2\omega} = 240$ kV/cm, respectively. As intended, the fiber laser setup covers similar field amplitude ranges as the numerical simulations presented in chapter 4.1.

A plot of the current amplitude against the electric field amplitudes allows for a direct comparison with the predicted scaling law $\mathrm{d}J/\mathrm{d}t \propto \eta_3 E_\omega^2 E_{2\omega}$ as well as the numerical simulations. Indeed, for fixed excitation fields $E_{2\omega}$, the current amplitudes in Fig. 4.2 scale quadratically with low excitation fields E_ω, as illustrated by empirical parabolic fits. However, if the fundamental excitation field E_ω exceeds 0.5 MV/cm, the current amplitude is significantly lower than predicted by the perturbative theory. Eventually, the current amplitude even saturates and begins to decline again. These effects are the more pronounced, the lower the fixed intensity of the second harmonic beam is. Besides, a reduction of the second harmonic intensity results in an overall reduction of the current amplitude.

The experimental data in Fig. 4.2 features a similar dependence on the fundamental field amplitude E_ω as the numerical simulations in Fig. 4.1. Both show significant deviations from the parabolic behavior in the range of 1 MV/cm and above. Particularly at high second harmonic intensities, the functional dependence of the experimental curves and the theoretical simulations agree well. By contrast, the experimental measurements for the lowest second harmonic intensity show a much more pronounced current saturation than the simulations.

For further discussion, it is necessary to consider the validity of a direct comparison between the measurements and the numerical simulations of QUIC. The simulations describe the injected current density in intrinsic GaAs right after excitation by plane waves with a Gaussian temporal profile. In contrast, the measurements reflect the time-integrated current that is induced in metallic contacts on the sample. The current injection itself takes place in LT-GaAs at a spatially confined focal spot and is mediated via a charge dipole that is not included in the simulation. Such factors may additionally affect the current measurement.

In order to investigate the observed current saturation and above mentioned effects in more detail, additional measurements are performed. In particular, time-resolved measurements allow to distinguish between effects that influence the measurement process or the current injection itself. For example, the charge dipole is affected by the surrounding carrier density that increases with the illumination intensity.

Similar to the measurement series described above, the maximum current amplitude is also determined as a function of the second harmonic intensity for different fixed fundamental beam intensities. At second harmonic field amplitudes in the order of 100 kV/cm, the current begins to saturate and deviate from the expected linear scaling with respect to the electric field amplitude. In general, the current dependence on the second harmonic

field is more complicated than the current dependence on the fundamental field. With a photon energy that exceeds the band gap, the second harmonic beam is able to excite direct transitions between a valence band and the conduction band. As a consequence, the current measurement is more susceptible to disturbing effects induced by the second harmonic beam. For example, even low stray light of the second harmonic beam is able to generate significant photocurrents at the metal-semiconductor junction. For this reason, the present chapter focuses on current saturation by an increase of the fundamental intensity at a fixed second harmonic intensity.

To rule out that the saturation is not caused by a potential current limitation of the setup, for example by a decreasing current extraction efficiency of the metallic contacts, the measurement series depicted in Fig. 4.2 is repeated for different experimental conditions. First, measurements with a different LT-GaAs sample featuring a gap width of only 25 µm are carried out. Although the recorded currents are much larger with amplitudes of more than 10 nA, the current exhibits saturation effects at similar fundamental field intensities as in Fig. 4.2.

By probing the QUIC tensor element η_3^{xxyy} instead of η_3^{xxxx}, as in the previous measurements, the current injection amplitude can be reduced while keeping the illumination intensity the same. Such a measurement requires a simultaneous pulse triplet consisting of a vertically polarized second harmonic pulse, a vertically polarized fundamental pulse and a horizontally polarized fundamental pulse. Therefore, a third interferometer arm is added to the setup by placing a beamsplitter into the fundamental beam arm (cf. Fig. 4.4). Half-wave plates allow to adjust the relative polarization of the three pulses. For better comparison, the measurements at this three-beam setup employ the same sample as the measurements shown in Fig. 4.2.

As expected, the measurements which yield the η_3^{xxyy} current component feature significantly smaller amplitudes than the previous measurement series. Nevertheless, the current shows saturation effects at similar intensities. Therefore, it can be concluded that the saturation is indeed linked to the excitation intensities and not simply to the amplitude of the injected current.

To further investigate the reproducibility of current saturation, the measurement series depicted in Fig. 4.2 is also repeated with the OPA laser system employing a similar interferometric setup but a different LT-GaAs sample. In fact, with the LT-GaAs sample described at the beginning of this chapter, current injection by the OPA laser system is barely measurable. Apart from the lower average beam powers of the OPA system in the order of 1 mW, such behavior can be attributed to the lower repetition rate of 250 kHz. As detailed in chapter 3.3, the measurement of current injection can be explained by the generation of a long-living electronic dipole in the LT-GaAs that induces a compensating

current. If the repetition rate of the laser pulses is too low, the dipole may decay on time scales much shorter than the pulse separation and the current measurement is hampered. However, by using another LT-GaAs sample with different growth parameters and a smaller gap width of about 10 µm, a higher extraction efficiency can be achieved and it is possible to inject measurable currents with the OPA system.

Similar to the measurement series depicted in Fig. 4.2, the current injection amplitude is determined for different intensity combinations at the OPA setup. Fig. 4.3 shows the extracted current amplitude as a function of the fundamental excitation intensity for fixed intensities of the second harmonic beam. In the same way as in Fig. 4.2, the lower scale is linear in the peak amplitude of the electric field. The top scale shows the corresponding peak intensities. The respective wavelengths of both beams are similar to the measurement series at the fiber laser setup. Beam diameters in the focal spot are 15 µm for the fundamental beam and 34 µm × 44 µm for the second harmonic beam. Again, the temporal width of the fundamental pulses, here about 50 fs, is also used to calculate excitation intensities of the second harmonic pulses. Because of a lower repetition rate, beam powers in the order of 1 mW on the sample amount to even higher peak intensities and field amplitudes than in the fiber laser setup.

In general, the functional dependence of the OPA measurement series is in accordance

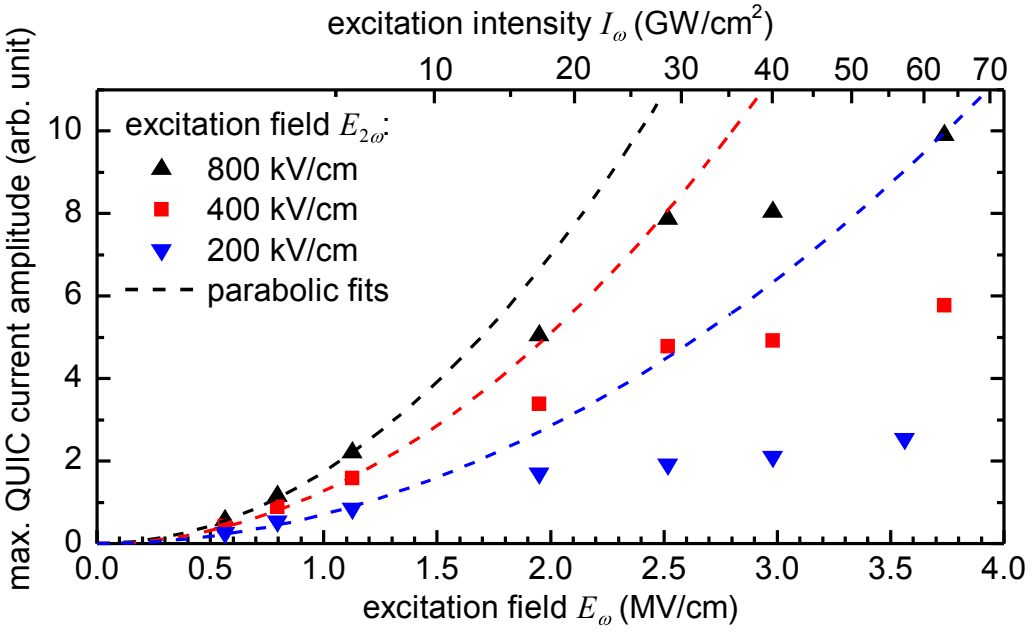

Fig. 4.3: Extracted maximum current amplitudes of QUIC in room-temperature LT-GaAs for different intensity combinations of the incident fundamental and second harmonic laser pulses. Each data point is derived from a current interferogram recorded around maximum pulse overlap at the OPA laser system. Empirical parabolic fits illustrate deviations from the scaling of the perturbative $\chi^{(3)}$ model. The depicted excitation fields $E_{2\omega}$ correspond to intensities $I_{2\omega}$ of 0.2 GW/cm^2, 0.8 GW/cm^2 and 3.2 GW/cm^2, respectively.

with the measurements at the fiber laser setup. An increase in the fixed second harmonic intensity also results in an overall increase of the current amplitudes. Here, the lowest second harmonic intensity approximately equals the highest second harmonic intensity in Fig. 4.2. The data points scale quadratically with low intensities of the fundamental beam, in accordance with the $\chi^{(3)}$ model. Empirical parabolic fits are added for illustration. Similar to the previous measurement series, the current begins to saturate at excitation fields in the order of 1 MV/cm. The upwards trend at the highest intensity is probably related to a slight misalignment by the filter wheel that is used to adjust the intensity and set to maximum transmission in this case.

Time-Resolved Measurements

In order to experimentally investigate the origin of the current saturation, further time-resolved measurements are carried out. Although the OPA laser system covers a broader intensity range, these measurements are predominantly performed with the fiber laser setup. The FFS is more stable regarding beam intensity as well as alignment and allows for reproducible measurement conditions. Furthermore, the low average powers of the OPA system complicate a precise intensity adjustment. For example, excitation amplitudes of $E_\omega = 1$ MV/cm and $E_{2\omega} = 200$ kV/cm correspond to an average OPA beam power of only 100 µW and 25 µW, respectively. Lastly, in contrast to the fiber laser setup, the focal spots of the OPA setup exceed the gap width of the corresponding LT-GaAs sample making it susceptible to potential illumination effects at the semiconductor-metal junction.

To get more insight into the microscopic processes that follow the pulsed laser excitation, the experimental setup is modified to perform pump-probe type measurements. Special focus is put on the influence of an increased irradiance on the measurement process. As stated above, the injected current is mediated by an electronic dipole whose dynamics are affected by carrier excitation. For this reason, the injected current amplitudes are determined as a function of an additional delayed fundamental pump pulse which causes an increase of the carrier density.

As displayed in Fig. 4.4, the additional pump beam is realized by adding a third interferometer arm to the setup. To this end, a second beamsplitter is placed into the fundamental beam arm. The transmitted beam serves as pump beam. Its relative delay τ_{pump} with respect to the pulse pairs can be adjusted via the motorized XM stage. The reflected fundamental and second harmonic beam provide the simultaneous pulse pairs for QUIC. By tuning the arm length of the second harmonic beam with a piezo actuator, the relative delay τ between the pulse pair components can be slightly adjusted. All beams are collinearly focused on the 50 µm gap of the LT-GaAs sample that is described at the beginning of this chapter. The polarization of the pulse pair is aligned along the width

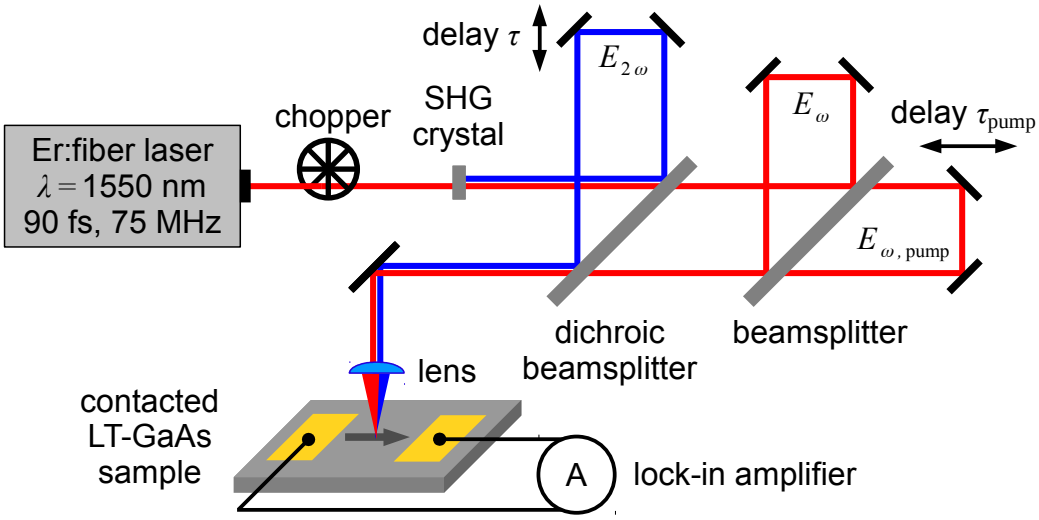

Fig. 4.4: Experimental scheme for time-resolved measurements of QUIC; the setup is similar to the prototypical setup displayed in Fig. 3.1: The emitted laser pulses are frequency-doubled in a nonlinear crystal and steered into an interferometer which allows to control the individual delay, polarization and intensity of the beams (optics not shown). Via a beamsplitter in the fundamental beam arm, an additional fundamental pump beam is provided. Its relative delay τ_{pump} with respect to the other beams can be controlled with a motorized stage. The other two arms provide the fundamental and second harmonic component of the overlapping pulse pairs which are used for QUIC. Their relative delay τ can be fine-tuned with a piezo-driven stage. All beams are collinearly focused on a contacted LT-GaAs sample; the photoresponse is recorded with a lock-in amplifier.

of the gap to maximize current injection. By contrast, the pump pulse is orthogonally polarized to the pulse pair to minimize interference effects.

Here, the pump-probe scheme is based on two probe beams, namely on the overlapping pulse pair whose time-averaged current injection is measured as a function of the additional pump beam. To this end, the relative delay τ between both pulse pair components is slightly varied while keeping the arm length of the additional pump beam and in turn τ_{pump} constant. The current amplitudes of the resulting current interferograms are extracted in the same way as above. Such measurements are repeated for different delay times τ_{pump} as well as different beam intensities.

Fig. 4.5 depicts the current amplitude of the interferograms as a function of the pump delay τ_{pump}. The pulse timing is illustrated in the top of the figure. At negative delay times τ_{pump}, the fundamental pump pulse impinges on the LT-GaAs before the pulse pair. The calculated excitation intensities are 10 GW/cm^2 for the pump pulse and 1 GW/cm^2 for the fundamental component of the pulse pair. As evident from Fig. 4.2, the pump intensity is in the range in which current saturation occurs. The intensity of the second harmonic beam differs for the three curves displayed in Fig. 4.5. The highest intensity approximately corresponds to the second harmonic intensity of Fig. 4.2(a). For better comparison, the

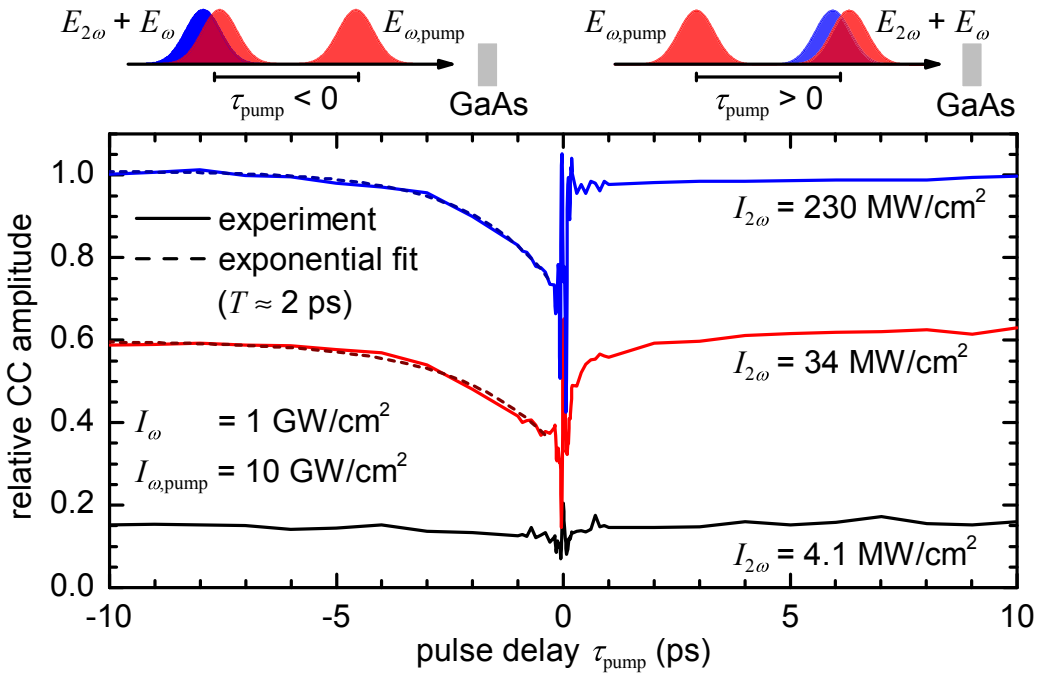

Fig. 4.5: Extracted current amplitudes of QUIC in LT-GaAs by a pulse pair ($E_{2\omega} + E_\omega$) as a function of the relative delay τ_{pump} of an additional fundamental pump pulse ($E_{\omega,\mathrm{pump}}$). The relative pulse ordering with respect to the sample is displayed in the top. At negative delay times, the pump pulse precedes the overlapping pulse pair. Current amplitudes are extracted from the amplitudes of current interferograms recorded by slightly varying the relative delay τ between the pulse pair components around maximum overlap while keeping the pump delay τ_{pump} constant. Afterwards, the current amplitudes are normalized to the corresponding amplitudes extracted for the same excitation intensities but with the pump beam blocked. Measurements are performed with fixed intensities of the fundamental beams and three different intensities of the second harmonic beam. Apart from a delay-independent reduction, the current amplitudes can be described by a one-sided exponential decay with a time constant in the order of 2 ps.

three curves are normalized to the corresponding unpumped current amplitudes. To this end, reference current interferograms are recorded with the pump beam blocked.

The data of Fig. 4.5 reveals two main effects of the pump beam. On the one hand, the pump pulse causes an overall decrease of the current amplitude that is almost independent of the pump delay. On the other hand, the curves contain a delay-dependent component for negative delay times. When τ_{pump} approaches zero, the current amplitude is more and more reduced. An empirical exponential fit of the form $-\exp(\tau_{\mathrm{pump}}/T)$ yields a decay constant of $T \approx 2$ ps. It should be emphasized that there is not such a distinct delay-dependent component for positive τ_{pump}. At $\tau_{\mathrm{pump}} \approx 0$, the data is distorted by residual interference effects of both fundamental beams. For this reason, the pump-probe scheme is not suited to identify additional effects on a timescale of 100 fs or less.

The relative magnitude of the delay-dependent and delay-independent current reduction

depends on the second harmonic intensity. For the lowest curve in Fig. 4.5 with $I_{2\omega} = 4.1\ \mathrm{MW/cm^2}$, a delay-independent reduction of about 85 % dominates. On the contrary, the current decrease is almost entirely determined by the delay-dependent component for the highest curve with $I_{2\omega} = 230\ \mathrm{MW/cm^2}$. At $\tau_{\mathrm{pump}} \approx -0.5$ ps, the corresponding current reduction amounts to about 25 %. The curve for an intermediate second harmonic intensity contains significant portions of both the delay-independent and the delay-dependent effect.

First, the following discussion focuses on the delay-independent current reduction. This effect can be attributed to a carrier-induced recombination of the electronic dipole. Such macroscopic charge separation forms after current injection and allows to measure the injection via metallic contacts, as discussed in chapter 3.3. If the fundamental pump pulse hits the LT-GaAs sample, it massively populates the conduction band via two-photon absorption and excitation of defect states. In essence, these free carriers may result in a short circuit of the dipole and in turn reduce the measured current amplitude.

A pump intensity of $I_\omega = 10\ \mathrm{GW/cm^2}$ results in an estimated carrier density in the order of $10^{18}\ \mathrm{cm^{-3}}$. The majority is generated via excitation of defect states. Transmission measurements on the same material yield a corresponding fundamental absorption constant of $\alpha = 750\ \mathrm{cm^{-1}}$ that gives rise to a corresponding excitation density of $5 \cdot 10^{18}\ \mathrm{cm^{-3}}$. However, such a density should only be regarded as an upper limit since the typical density of defect states in LT-GaAs is in the same range [69; 79]. Moreover, the calculation assumes that all photons are homogeneously absorbed within a volume given by the spot size and the absorption depth α^{-1}. Additionally, two-photon absorption generates a carrier density of $10^{17}\ \mathrm{cm^{-3}}$. This calculation is based on a two-photon absorption coefficient of $\beta = 3.5\ \mathrm{cm/GW}$ for GaAs that was determined via z-scan measurements with the same laser system [80] and agrees with previous studies [81]. Owing to the nonlinear behavior of two-photon absorption, the absorption length of two-photon absorption also depends on the peak intensity I via $(\beta I)^{-1}$.

While the picture of a pump-induced discharge mechanism is illustrative for positive delay times τ_{pump}, it is quite counterintuitive that the the pump pulse may result in the same current reduction if it precedes the current injection process. However, it must be taken into account that the laser emits pulses with a repetition rate of 75 MHz. Consequently, a slightly negative pump delay is equivalent to a delay of 13.6 ns with respect to the current injection of the previous pulse pair. If the recombination time of the dipole significantly exceeds the pulse separation, the discharge should be independent of the timing of the pump pulse.

A rough estimation of the discharge time of the unperturbed electronic dipole on the basis of its RC constant is given in the following. As already stated in chapter 3.3, the spatial charge distribution is immobilized by defect states with a separation given by the

beam diameter. In a first approximation, the electronic dipole can be modeled by a capacitor consisting of two oppositely charged parallel cylinders embedded in a GaAs matrix with $\epsilon_r \approx 13$ [53], as sketched in Fig. 4.6. The minimum beam diameter of about 10 µm determines the length l and distance s of both cylinders. Their diameter d defines the depth of the charge distribution. It is set by the absorption length of the second harmonic beam to 670 nm [9, and references within]. The resulting capacitance of both cylinders can be approximated to $C = \pi\epsilon_r\epsilon_0 l/\operatorname{arcosh}(s/d) \approx 1$ fF [82, p. 319].

Apart from the capacitance, the decay time of the capacitor is determined by the resistance between both cylinders. To this end, the interspace is modeled by a GaAs cuboid with the dimensions $d \times s \times l$. Presuming a typical specific resistance of 10^6 Ωcm for annealed LT-GaAs [68], the resistance amounts to $R \approx 15$ GΩ. Taken together, the RC time constant that determines the discharge of a capacitor can be computed to $\tau_{RC} = RC = 15$ µs. In comparison, the pulse separation of the fiber laser is three order of magnitude lower.

With the above calculated time constant, it is reasonable to assume that the electronic dipole is practically in a steady state. After initial buildup, the electronic dipole is merely slightly reinforced by the current injection of each succeeding pulse pair. For this reason, the current reduction by dipole recombination should not depend on the relative timing of the pump pulse and the pulse pair. By contrast, the pulse separation of the OPA laser system is in the same order as the calculated discharge time. This explains why the same sample generates barely measurable currents at the repetition rate of the OPA laser system.

Similar to the pump pulse, the dipole can also be partially discharged by the current generating pulse pair itself. Particularly the second harmonic pulse efficiently populates the conduction band since its energy exceeds the band gap. Indeed, the current amplitudes in Fig. 4.2 also deviate from the theoretically predicted proportionality to $E_{2\omega}$ and are lower than expected at high second harmonic intensities.

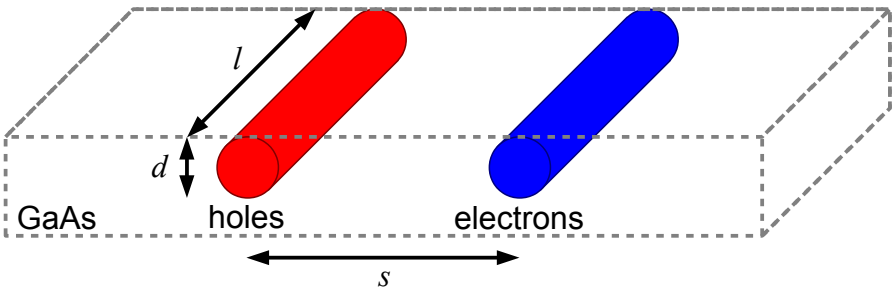

Fig. 4.6: Approximation of the frozen charge dipole by two oppositely charged parallel cylinders embedded in a GaAs matrix. The length l and distance s of the cylinders is given by the beam diameter (cf. Fig. 3.2). The diameter d of the cylinder and in turn the depth of the charge distribution is determined by the absorption length.

Such discharge effects would be in line with the observed intensity dependence of the delay-independent current reduction in Fig. 4.5. If the induced carrier density of the pulse pair is relatively small, the discharge is dominated by the high-intensity pump pulse. On the contrary, if the second harmonic intensity is very high, the pulse pair already results in an efficient partial discharge of the dipole. In this case, the additional influence of the pump pulse would be significantly reduced as observed for a second harmonic intensity of $I_{2\omega} = 230\,\mathrm{MW/cm^2}$. With an absorption constant of $1.5 \cdot 10^4\,\mathrm{cm^{-1}}$ for 775 nm [9, and references within] such a second harmonic intensity gives rise to a carrier density of $10^{18}\,\mathrm{cm^{-3}}$. However, concerning a direct comparison of the electron densities, it must be taken into account that the spot size of the second harmonic beam exceeds the spot size of the fundamental beam. In general, it should be noted that an exact deduction of the underlying discharge mechanism is not feasible on the basis of the data in Fig. 4.5 alone.

A central result of Fig. 4.5 is the observation that the delay-independent current reduction of the pump pulse vanishes at very high second harmonic intensities. This finding helps to interpret the data in Fig. 4.2. As already stated, the observed current saturation at low second harmonic intensities is much more pronounced than the saturation in the theoretical simulations in section 4.1. Such a deviation can be attributed to the above mentioned dipole discharge. On the contrary, the influence of the fundamental intensity on the dipole discharge should be negligible for the curve in Fig. 4.2(a).

Apart from the delay-independent reduction, the data in Fig. 4.5 also contains a component that depends on the timing of the pump beam. It is most pronounced if the delay-independent reduction is suppressed and can be approximated by a one-sided exponential decay. The decay constant of $T \approx 2$ ps matches the typical trapping time of defects in LT-GaAs [70; 72–74]. In specific, additional time-resolved transmission measurements at the same LT-GaAs material yield a trapping time in the order of 1 ps [43]. These features indicate that this current reduction component is directly related to an interaction of the pump-induced carrier density on the one side and the current injection by the pulse pair on the other side.

After excitation, the carriers rapidly relax to the band minimum and are trapped in defect states within the following picoseconds. As a result, for $\tau_{\mathrm{pump}} \ll -1$ ps, the pump-induced carriers have already been trapped in defect states when the pulse pair impinges. If τ_{pump} approaches zero, the residual density of free carriers increases and the current amplitude decreases. For $\tau_{\mathrm{pump}} > 0$, at which the pulse pair precedes the pump pulse, the current amplitude returns practically instantaneously to the baseline level. Because of the interference effects of the fundamental pump and probe pulse in Fig. 4.5, an exact deduction of the behavior at $\tau_{\mathrm{pump}} \approx 0$ is not feasible. Nevertheless, the data indicate that this current reduction component depends on the density of free carriers during the

current injection process which takes place on a time scale in the order of 100 fs, given by the width of the pulse pair. A detailed discussion of the processes on such a time scale is given in chapter 4.3.

The distortion by the interference of both fundamental pulses motivates another set of experiments with the two-beam setup depicted in Fig. 3.1. The current interferograms of the two-beam experiment reflect the current injection as a function of the temporal overlap of the approximately 100 fs wide pulses. In case that the current injection depends on the exact ordering of the fundamental and second harmonic pulse, such an effect should manifest in the envelope of the current interferogram. To this end, full interferograms as in Fig. 3.3 are recorded for different intensity combinations. Subsequently, the difference between the respective upper and lower envelopes of the oscillating current signal are numerically extracted.

Fig. 4.7(a) exemplarily displays these differential envelopes for different fundamental intensities and a fixed second harmonic intensity of $I_{2\omega} = 340$ MW/cm^2. For better comparison, all curves are normalized to unity. In this way, the delay-independent intensity dependence of the current injection, particularly the above mentioned dipole discharge effect, cancels out. As illustrated in the top of Fig. 3.3, the fundamental pulse precedes the second harmonic pulse for $\tau < 0$.

The curves reveal a significant influence of the fundamental intensity on the width of the envelopes. While the envelopes are almost unchanged for $\tau > 0$, an increase of the fundamental intensity results in a marked current reduction for $\tau < 0$ at which the fundamental pulse precedes. For example, at $\tau = -60$ fs the current is reduced by up to 15 %. Such a behavior is in line with the measurements of Fig. 4.5 and corroborates that the current reduction is sensitive to the pulse ordering. However, it should also be noted that both experiments are not directly comparable because of the different pulse combinations.

For a quantitative analysis, the widths (FWHM) of the envelopes are extracted. These are plotted in Fig. 4.7(b) as a function of the fundamental excitation intensity for different fixed second harmonic intensities. The latter are distinguished by different symbols. In general, the covered intensity range is similar to the range of Fig. 4.2. As expected, the envelope widths decrease with an increase of the fundamental intensity. In comparison to the data point at the lowest fundamental intensity, the widths decreases by up to 10 %.

The current envelopes are also evaluated for the measurements at the OPA laser system whose amplitudes are depicted in Fig. 4.3. In contrast to the measurements above, a significant and reproducible influence of the fundamental intensity on the envelopes cannot be determined. However, it should be noted that the current interferograms are much noisier, particularly at the lowest intensities, which impedes an exact analysis. Furthermore, the

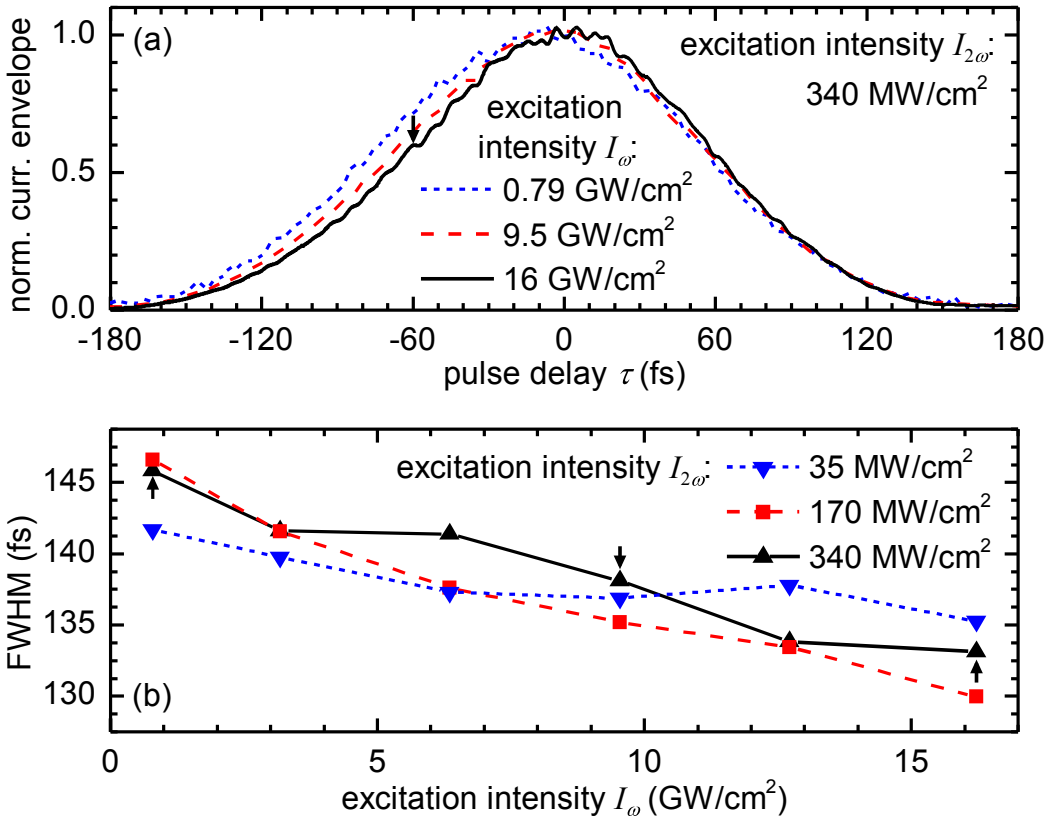

Fig. 4.7: (a) Envelopes of current interferograms recorded at the fiber laser setup for different intensities of the incident fundamental and second harmonic pulses. The curves represent the normalized difference of the upper and lower envelopes of current interferograms recorded by varying the relative delay τ between the fundamental and second harmonic pulses (cf. Fig. 3.3). At negative delay times τ, the fundamental pulses precede the second harmonic pulses. The relative current reduction at $\tau < 0$ is illustrated by an arrow at $\tau = -60$ fs. (b) Temporal width (FWHM) of the envelopes of the interferograms as a function of irradiance. Arrows denote the temporal width of the corresponding envelopes depicted in (a).

expected influence on the envelopes should be in general less pronounced since the pulses and in turn the current interferograms are only half as wide compared to the measurements at the fiber laser setup. Finally, the pulse intensities of the OPA system may be too high. As depicted in Fig. 4.3, the current amplitudes already begin to flatten after the third data point. In the case of maximum saturation, a further increase of the excitation intensity would not be expected to affect the envelopes.

4.3 Discussion of Ultrafast Dynamics

In this chapter, the underlying mechanisms of the saturation effects of the experimental measurements and the numerical simulations of QUIC are discussed. While the discussion in the previous chapter focuses on the influence of the rather long-living frozen

charge dipole, the present chapter addresses the dynamics on picosecond and femtosecond time scales. In particular the previously mentioned time-resolved measurements indicate a marked distortion of current injection on such time scales.

The delay-dependent component of the pump-probe measurements (cf. Fig. 4.5) implies a link between the current saturation and the density of free carriers during current injection. Such an influence can be attributed to different mechanisms. First, an enhanced carrier density affects the motion of the injected carriers. Second, a massive population of the bands influences electron transitions and therewith current injection. At the end of the chapter, the influence of a further higher-order effect, the intraband acceleration, is discussed.

Influence of Current Dynamics

After current injection by the pulse pair, the carriers form an electronic dipole in the LT-GaAs sample. Following the approach of Zhao *et al.*, the dynamics of such a dipole can be approximated by a rigid shift model [67]. To this end, the dipole is modeled by two slightly shifted Gaussian charge distributions describing electrons and holes. Both distributions attract each other via Coulomb forces of the resulting space-charge field that eventually leads to a dipole recombination. With the simplification that the width of the distributions is fixed, the dynamics can be shown to resemble a damped harmonic oscillator. In specific, the oscillation period is determined by the inverse plasma frequency Ω^{-1}. To apply such a model on the measurements presented above, the properties of LT-GaAs have to be taken into account since the study of Zhao *et al.* focuses on QUIC in GaAs/AlGaAs multi-quantum wells and bulk GaAs.

Defect states in LT-GaAs freeze the electronic dipole before it recombines and therefore allow for a measurement via external electrical contacts. In essence, the dynamics can be thought of as a competition between the carrier trapping on the one side and the dipole recombination on the other side. While the trapping time is more or less fixed with a time constant in the order of 1 ps, the plasma frequency increases with the carrier density. As a consequence, a high carrier density may result in a partial recombination before the dipole is immobilized by trap states.

The plasma frequency Ω of electrons with an effective mass m_e^* and a density of n_e in a solid is given by $\Omega^2 = n_\mathrm{e} e^2/(4\pi^2 \epsilon m_\mathrm{e}^*)$ [19; 47, ch. 7]. Consequently, the inverse plasma frequency Ω^{-1} is proportional to $1/\sqrt{n_\mathrm{e}}$. For GaAs and the above mentioned excitation densities of about $10^{18}\,\mathrm{cm}^{-3}$, the inverse plasma frequency is in the order of 1 ps and comparable to the trapping time. If the density decreases, the inverse plasma frequency prolongs.

Regarding the pump-probe measurements, the residual carrier density during current

injection increases if τ_{pump} of the preceding pump pulse approaches zero. As a result, Ω^{-1} decreases. Simultaneously, the current injection amplitude decreases. However, concerning positive delay times at which the pump pulse succeeds the pulse pair, the observed temporal dependence does not seem fully consistent with the dynamics of the rigid shift model. If such processes take place on a picosecond time scale during and after current injection, a high-intensity fundamental pulse would be expected to influence the current amplitude at least partially even if it slightly succeeds the pulse pair. The increase of the plasma frequency would just be slightly delayed. However, it must be emphasized that the rigid shift model is only intended to illustrate the carrier dynamics in a qualitative way and does not describe the exact dynamics [67].

Numerical calculations for multiple quantum wells by Sherman *et al.* that are based on a hydrodynamic model yield significant deviations of the dipole dynamics from the rigid shift model [83]. Particularly at high carrier densities, the behavior of an electron-hole plasma is predicted to be nonuniform and in general more complex because of carrier-carrier interactions, specifically Coulomb interaction and drag effects. Thus, it is not unexpected that the carrier dynamics may depend on the pulse ordering. At room temperature and moderate carrier densities, currents that are optically injected into LT-GaAs rapidly relax on a time scale in the order of 100 fs, predominantly by LO-phonon scattering and impurity scattering [9, and references within]. If a high-intensity fundamental pulse precedes the second harmonic pulse, the current is injected into an already existing electron-hole plasma that immediately affects the carrier motion. In the reverse case, however, the current may have already relaxed when the additional electron-hole plasma is generated.

The specific influence of an enhanced carrier density on the decay of the injected current has also been theoretically investigated by Duc *et al.* [39; 40]. Indeed, the studies reveal that while the current relaxation is dominated by interaction with LO-phonons at low densities, the influence of carrier-carrier scattering increases with the electron density. However, a quantitative comparison with the measurements presented here is not feasible because the simulations only cover one- and two-dimensional structures.

Band Filling Effects

The simulations presented in chapter 4.1 are specifically based on a three-dimensional model with excitation conditions similar to those of the experimental study. These simulations yield the current density right after injection without the influence of succeeding dipole dynamics. Since relaxation processes are treated in a phenomenological way with a constant relaxation time, the influence of an intensity-dependent scattering is also not explicitly included in the simulations. By switching off these subsequent current dynamics, the simulations specifically allow to investigate the behavior of QUIC itself at high

intensities. As the simulations still predict a current saturation for elevated intensities (cf. Fig. 4.1), it can be concluded that the injection process itself deviates from the perturbative theory at such excitation intensities.

At high excitation intensities, electron transitions and therewith QUIC are predicted to be influenced by band filling effects during the light-matter interaction [39; 40]. According to Pauli's exclusion principle, there is only a finite number of Bloch states available in a band. Furthermore, optical transitions only address a relatively small portion of these states that is determined by the photon energy. Therefore, a high-intensity pulse is able to excite a high percentage of the addressed electrons in the valence bands into the conduction band. As a consequence, the absorption of a succeeding pulse is reduced as there are less electrons in the valence bands and less free states in the conduction band left. With respect to a pump pulse whose energy exceeds the band gap, such bleaching effects have already been observed in GaAs [84–86]. Since QUIC is based on the simultaneous absorption of two pulses that address the same states, it is also predicted to be affected by state blocking.

In a first approximation, band filling effects can be estimated by calculating the number of addressed states. According to the effective-mass approximation, the energy dispersion $E(\mathbf{k})$ and the resulting density of states $D(E)$ at the Γ-point ($\mathbf{k} = 0$) can be described by a parabolic band [87, ch. 6.15] with

$$E = \frac{\hbar^2 |\mathbf{k}|^2}{2m_\mathrm{e}^*} \quad \text{and} \quad D(E) = \frac{1}{2\pi^2} \left(\frac{2m_\mathrm{e}^*}{\hbar^2} \right)^{\frac{3}{2}} \sqrt{E}. \tag{4.4}$$

Here, m_e^* denotes the effective electron mass. Concerning optically induced transitions, the excess energy E is determined by the photon energy. Owing to the negligible photon momentum, a transition from a hole to the conduction band connects states with virtually the same $\mathbf{k}$-vector. The excess kinetic energy of the excited electrons and holes can be calculated on the basis of the energy conservation taking the band gap E_G into account. In essence, the excess energy of electrons and holes is weighted by their effective masses. For GaAs and an excitation energy of 1.6 eV, as used in the experiments in chapter 4.2, the excess energy amounts to 160 meV for electrons in the conduction band and 20 meV for heavy holes. Because of their high effective mass, the hole density of states is dominated by heavy holes and exceeds the corresponding density in the conduction band. Therefore, the number of addressed states is mainly limited by the conduction band.

The energy bandwidth of optically addressed states in a band is determined by the temporal pulse width t_p (FWHM). According to the time-bandwidth product (see also chapter 5.1), the minimum frequency bandwidth of a laser pulse is given by $\Delta f = 0.44/t_\mathrm{p}$. In turn, the energy bandwidth can be calculated via $\Delta E = h\,\Delta f$ which results in 20 meV for a 90 fs pulse width. As a first approximation, the total number of addressed states in the conduction band can be estimated by multiplying the energy bandwidth ΔE with the

density of states $D(E)$. With the above calculated parameters, the density amounts to $9 \cdot 10^{17}$ cm^{-3} for electrons and $7 \cdot 10^{18}$ cm^{-3} for heavy holes.

The density of potentially addressed states compares with the number of excited carriers that is estimated on the basis of the absorption coefficients. The calculation is performed in the same way as in chapter 4.2. It is assumed that all photons are absorbed within a volume determined by the spot size and the absorption length. Regarding the fiber laser setup and the corresponding simulations, an excitation with the fundamental wavelength of 1550 nm and an intensity of 18 GW/cm^2 gives rise to a density of $4 \cdot 10^{17}$ cm^{-3} via two-photon absorption. As mentioned in chapter 4.2, direct absorption of a second harmonic beam with a peak intensity of 230 MW/cm^2 generates a carrier density of 10^{18} cm^{-3}. Furthermore, the fundamental beam may excite carriers in the order of 10^{18} cm^{-3} from defect states in LT-GaAs that are not included in the simulations. However, since these defect states are scattered in the band gap [68–70], their excitation does not necessarily address the same states as the interband transitions.

Regarding the measurements at the OPA setup, the calculated carrier densities are even higher. At the highest intensities displayed in Fig. 4.3, the densities are $3 \cdot 10^{18}$ cm^{-3} for two-photon absorption and $9 \cdot 10^{18}$ cm^{-3} for direct interband absorption. On the other side, the energy bandwidth and in turn the number of addressed states is doubled due to the shorter pulse length of about 50 fs.

The comparison of the number of potentially addressed states on the one hand and the calculated number of excited carriers on the other hand implies that absorption saturation has a significant influence at such excitation intensities. Obviously, the calculation of the excited carriers is only a rough estimation and should be regarded as an upper limit, not least since these partially exceed the number of addressable states. Nevertheless, it can be concluded that increasing the excitation intensity should indeed significantly reduce the number of available states and therefore influence QUIC.

In order to investigate experimentally whether increased fundamental excitation results in substantial Pauli blocking via two-photon transitions alone, the transmission of intrinsic GaAs is probed by time-resolved measurements. These measurements are performed at the interferometric fiber laser setup (cf. Fig. 3.1) to provide the same range of excitation intensities as in the current measurements and in the simulations. The LT-GaAs sample is exchanged with a 400 nm thick layer of GaAs glued on a thin glass substrate since the thickness of the contacted LT-GaAs clearly exceeds the absorption length of the second harmonic beam and would impede transmission measurements. Also, by using nominally intrinsic GaAs, the influence of defect states is minimized.

By changing the relative length of one interferometer arm, the transmission of a weak second harmonic probe beam is measured as a function of the delay of a high-intensity

fundamental pump beam. To this end, the transmitted beams are filtered with a shortpass and focused with a lens onto a silicon photodiode. Its photocurrent is proportional to the intensity of the incident light and recorded by a lock-in amplifier. Since both beams address the same states in the conduction band, the transmission of the second harmonic beam reflects the state occupation induced by the fundamental beam.

Fig. 4.8(a) displays the pump-induced relative transmission change of the second harmonic beam as a function of the relative delay τ between the pump and probe pulses. Peak intensities of the fundamental pump beam and the second harmonic probe beam are 7.5 GW/cm^2 and 4.2 MW/cm^2, respectively. The transmission change is measured by referencing the lock-in amplifier to a chopper that is placed into the fundamental beam arm. The measured data is divided by the absolute transmission of the second harmonic beam to calculate the differential transmission. Additionally, by multiplying by a factor of ≈ 4, the transmission is corrected for the smaller spot size of the pump pulse compared to the probe spot. The solid black curve represents a smooth function that is applied to filter noise and interference effects. The latter probably stems from residual second harmonic intensity in the fundamental arm or SHG by the pump beam.

The curves reveal a significant τ-dependent influence of the fundamental pump beam. If

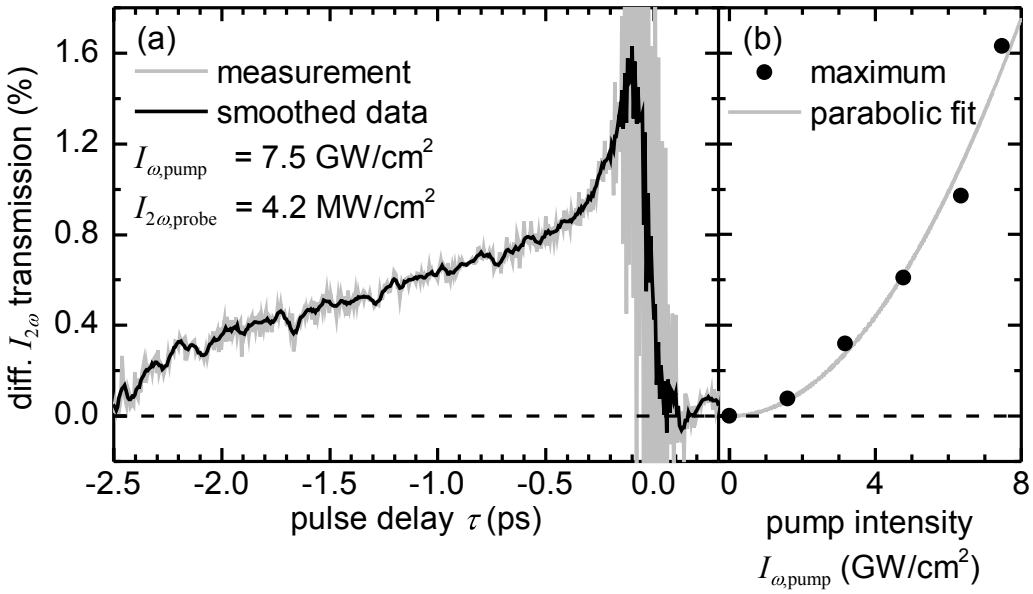

Fig. 4.8: (a) Differential transmission of a second harmonic probe beam through a 400 nm thick layer of GaAs as a function of the relative delay of a high-intensity fundamental pump beam. At negative delay times, the pump pulses precede the probe pulses. The transmission is corrected for the different spot sizes of the pump and probe beam. The decay of the transmission increase at negative delay times can be approximated by a biexponential function with decay constants in the order of 100 fs and 2 ps. (b) Maximum differential transmission (in (a) at $\tau \approx -0.1$ ps) as a function of the fundamental pump beam intensity with an empirical parabolic fit.

a probe pulse precedes a pump pulse, the transmission is unchanged. However, if the pulses impinge simultaneously, the transmission is increased by up to 1.6 %. Fig. 4.8(b) plots the measured maximum transmission change as a function of the fundamental pump intensity. As expected for excitation by two-photon absorption and illustrated by an empirical parabolic fit, the transmission change rises approximately quadratically.

The relative transmission change is comparable to previous studies of absorption saturation in GaAs induced by a pump pulse whose energy exceeds the band gap [85]. An extrapolation on the basis of the data in reference [85] yields an excitation density of $1.7 \cdot 10^{17}$ cm^{-3} by two-photon absorption. It is in the same order as the density of $7 \cdot 10^{16}$ cm^{-3} calculated by the two-photon absorption coefficient. Taking the simplifications of the calculations and the uncertainty of the nonlinear two-photon absorption coefficient into account, both densities agree quite well.

After pump excitation, the transmission decays with two time constants, 100 fs and 2 ps. The former decay constant can be attributed to the electron and hole relaxation to the band minimum and maximum, respectively [71]. Similar thermalization times have also been observed for absorption saturation induced by a pump beam whose energy exceeds the band gap [84; 86]. The longer decay component can be attributed to interband recombination, e.g. by electron-phonon scattering.

The longer decay component implies a significant occupation of the optically addressed states even if the carrier distribution is thermalized. The required density to completely fill the corresponding bands from their minimum or maximum to the optically addressed states can be calculated by integrating the density of states. With the above mentioned parameters, the total density amounts to $5 \cdot 10^{18}$ cm^{-3} for electrons and heavy holes each. However, since the distribution is smeared out due to thermalization, even lower excitation densities are sufficient to influence the absorption. The broadening at room temperature can be approximated by $k_\mathrm{B}T = 26$ meV. It is comparable to the energetic pulse width and the excess energy of the optically excited heavy holes. In comparison, the excess energy of excited electrons is 160 meV. Therefore, the longer decay component of the observed transmission decrease can be predominantly attributed to state blocking in the heavy hole band.

In general, the temporal behavior of the transmission measurements in Fig. 4.8 is consistent with the temporal behavior of the current measurements in Fig. 4.5 and Fig. 4.7. If the second harmonic pulse hits the sample first, its absorption is not affected by the succeeding high-intensity fundamental pulse and the current injection is only reduced by a delay-independent component. If the fundamental pulse impinges on the sample first, there is already a substantial number of states occupied when the second harmonic beam arrives. At such delay times the second harmonic absorption as well as the measured current is reduced. When the fundamental pump pulse precedes the second harmonic pulse by about

1 ps, the absorption and the current are influenced by a thermalized carrier distribution that has partially recombined.

In conclusion, the transmission measurements corroborate that state blocking by two-photon absorption has indeed a significant influence at such excitation intensities. A quantitative comparison of the observed transmission changes on the one side and the measured and simulated current injection on the other side reveals that the relative current reduction is higher than the corresponding absorption reduction. However, it must be taken into account that QUIC is a nonlinear process that cannot be directly compared to the transmission measurements. Probably, the influence of state blocking is higher for QUIC since it relies on two transition paths, one-photon and two-photon absorption, that both depend on the number of available states. Furthermore, the transmission measurements do not include the influence of a high-intensity second harmonic pulse and, in case of the measurements, LT-GaAs defect states.

Influence of Intraband Acceleration

Concerning the second harmonic intensity, the theoretical simulations shown in Fig. 4.1 predict a weak influence on the current saturation. Although the peak electric field amplitude of the second harmonic beam varies by an order of magnitude, the onset of the saturation does not significantly change. Indeed, the onset of the current saturation measured at the OPA setup and shown in Fig. 4.3 does not considerably depend on the second harmonic intensity, either. As already stated, the corresponding measurements at the fiber laser setup in Fig. 4.2 cannot be directly compared because of additional discharge effects at low second harmonic intensities. However, the reduction of the current envelope width in Fig. 4.7, wherein delay-independent effects cancel out, also reveals a weak influence of the second harmonic intensity.

If current saturation solely depended on the total number of excited carriers, a more pronounced influence of the second harmonic intensity would be expected. In the investigated intensity range, one-photon absorption of a second harmonic pulse is estimated to excite a comparable or even higher number of carriers than two-photon absorption of a fundamental pulse. In order to excite a fixed number of carriers by a pulse pair, the required intensity of the fundamental component is reduced if the intensity of the second harmonic component increases. As a consequence, an increase of the second harmonic intensity would be expected to shift the onset of the current saturation to lower intensities of the fundamental beam. However, the measurements and particularly the simulations that do not include additional current dynamics or potential influence of LT-GaAs defect states do not reveal such a pronounced behavior.

For the discussion of these observations it is instructive to recall the underlying theory

of the perturbative approach of QUIC on the one hand and the numerical simulations on the other hand. As detailed in chapter 2.2, the perturbative approach of QUIC is based on two interfering transition paths based on two-photon absorption of a fundamental beam and one-photon absorption of a second harmonic beam. Regarding the band structure (c.f. Fig. 2.1(a)), the corresponding processes are illustrated by vertical transitions. However, strictly speaking, these transitions only represent the lowest orders of the time-dependent perturbation expansion. One-photon absorption is described by a first order perturbation term and two-photon absorption by a second order perturbation term. While this approximation is valid at low intensities and correctly predicts QUIC in this regime, a perturbative approach principally does not describe the full light-matter interaction. This also applies to the above mentioned influence of Pauli blocking that has been treated in the same perturbative picture by two transitions that address the same states.

In contrast to the perturbative theory, the theoretical simulations in chapter 4.1 represent exact solutions of the semiconductor Bloch equations. With respect to the underlying model, the simulations fully describe the light-matter interaction and the injected current. If the excitation intensities increase, the perturbative theory deviates more and more from the exact solution and the simple picture of two vertical transitions breaks down. In fact, it can be shown that QUIC also relies on intraband interactions of states with different quasimomenta $\mathbf{k}$ [40]. Specifically, it can be shown that the interaction of an electric field with carriers in a semiconductor can be described by an explicit intraband acceleration term which modifies the quasimomentum [40; 88–90]:

$$\tilde{\mathbf{k}} = \mathbf{k} + \frac{e}{\hbar} \int \mathbf{E}(t)\,\mathrm{d}t \tag{4.5}$$

Taken alone, the term leads to a $\mathbf{k}$-shift of the carriers and in case of a light wave to an oscillation that broadens the carrier distribution in the $\mathbf{k}$-space [40]. In the case of optical excitation, the maximum $\mathbf{k}$-shift can be estimated by integrating the maximum field amplitude over half an oscillation period:

$$\Delta k = \frac{e}{\hbar} \int_0^{T/2} E\,\sin(2\pi f t)\,\mathrm{d}t = \frac{eE}{\hbar \pi f} \tag{4.6}$$

If the equation is evaluated for a fundamental pulse with the frequency $f = c/\lambda$ and a peak field amplitude of $E_\omega = 1$ MV/cm at which current saturation occurs, the maximum $\mathbf{k}$-shift amounts to $\Delta k_\omega = 2.5 \cdot 10^8$ 1/m. Remarkably, such a shift corresponds to about 1 % of the width of the first Brillouin zone of GaAs [53] and is accompanied by a significant energy shift. In comparison, a second harmonic pulse with a maximum field amplitude in the order of 200 kV/cm yields a $\mathbf{k}$-shift of only $\Delta k_{2\omega} = 2.5 \cdot 10^7$ 1/m.

In the following, a qualitative estimation of the influence of a significant $\mathbf{k}$-shift on

QUIC is given. It must be noted that a quantitative evaluation of the influence of a single interaction term on the resulting current injection is difficult, not least since there are other interaction terms involved, such as interband excitation. Furthermore, interference effects of the electric fields contribute to QUIC. On the basis of the parabolic band approximation (4.4), the excess energy and energy bandwidth of the optically addressed states in the conduction band can be calculated to 160 meV and 20 meV, respectively. Their corresponding quasimomentum is in the order of $5 \cdot 10^8$ 1/m and therefore comparable to the additional **k**-shift by the fundamental pulse. Consequently, it is reasonable to assume that at such excitation intensities the transitions are significantly affected by the **k**-shift and the perturbative theory of QUIC breaks down. Furthermore, such a **k**-shift of the occupied states would also complicate the Pauli blocking mechanism.

Concerning the dependence of the current saturation on the second harmonic pulse, it is important to note the intensity dependence of the intraband acceleration term (4.5). In contrast to carrier excitation by one-photon and two-photon absorption, the intraband acceleration term features the same linear dependence on the electric field amplitude for both the fundamental and the second harmonic beam. Therefore, the maximum **k**-shift of the second harmonic beam is lower than the corresponding maximum of the fundamental beam in the investigated intensity range. Such a relative weak influence of the second harmonic intensity is consistent with the intensity dependence of the simulations in Fig. 4.1.

In conclusion, the comparison of the theoretical simulations with the estimated intraband acceleration terms indicates that the perturbative theory of QUIC indeed breaks down in the investigated intensity range and Pauli blocking alone is not sufficient to completely describe the deviations. Since the intraband acceleration only occurs during the light-matter interaction, it can obviously not be attributed to all experimental measurements, in particular not to the current reduction by a preceding pump pulse.

4.4 Conclusion and Outlook

The behavior of QUIC in GaAs in the high-intensity regime is extensively studied. As predicted by numerical simulations, measurements of the current injection amplitude show pronounced saturation effects if the peak intensity of the fundamental beam exceeds 5 GW/cm^2, which corresponds to an electric field amplitude of 1 MV/cm. Additional time-resolved measurements as well as theoretical estimates are conducted to discuss the cause of these deviations from the perturbative approach of QUIC.

In practice, current injection is measured via contacted LT-GaAs samples. Pump-probe type measurements reveal that the observed current reduction can partly be attributed to carrier dynamics that follow the current injection. In essence, an increase of the intensity results in a higher carrier density that in turn reduces the magnitude of the measured

charge dipole.

The theoretical simulations specifically address the current injection process itself in bulk GaAs. They represent exact solutions of the semiconductor Bloch equations that describe the light-matter interaction. The excitation conditions of the underlying three-dimensional model are similar to those of the experimental study. Therefore, saturation features in the simulations reflect deviations of QUIC from the perturbative approach at experimentally accessible intensities.

In a first approach, the influence of Pauli blocking via a massive population of the optically addressed states is investigated. A comparison of the calculated number of potentially addressed states on the one side and the number of excited states on the other side implies a significant influence of state blocking at such intensities. Experimentally, this influence is corroborated by time-resolved transmission measurements at a thin GaAs layer that reveal a significant absorption saturation. Such effects are also consistent with features of the current injection measurements.

The intensity dependence of the simulated current injection implies further deviations of QUIC beyond Pauli blocking. It can be shown that QUIC also relies on intraband interaction of states with different quasimomentum. Specifically, such a light-matter interaction can be described by an explicit intraband acceleration term. A calculation of this term for the investigated intensity regime yields a substantial shift of the carriers' quasimomentum implying a significant influence on QUIC.

In conclusion, the study indicates significant deviations of QUIC from the perturbative $\chi^{(3)}$ picture at experimentally accessible excitation intensities. An experimental implementation of a terahertz detection scheme for QUIC would allow for further investigations from a different point of view. Since terahertz emission originates from the accelerated carriers, it would be less influenced by the formation of the carrier dipole.

Chapter 5

Phase-Retrieval of Ultrashort Laser Pulses via QUIC

The invention of ultrashort pulse lasers with pulse durations in the picosecond and femtosecond range [12; 13] triggered the development of new optical applications in research and industry. The high peak intensity of ultrashort laser pulses allows to investigate novel nonlinear optical effects [64], such as QUIC. Furthermore, the high peak intensities can be utilized for precise material processing [91–93]. In essence, the short pulse widths minimize damage of adjacent material. Besides, ultrashort pulses allow for time-resolved measurements with a temporal resolution determined by the pulse length [64; 94]. Therefore, a precise temporal characterization of ultrashort pulses is of central importance.

Because of their short duration, the temporal characterization of femtosecond laser pulses is a non-trivial task. The temporal intensity profile of such a pulse cannot simply be recorded by electronic means, e.g. with a photodiode, as these measurements are limited to at least picoseconds by parasitic capacitances. Apart from that, a time-resolved intensity measurement of a laser pulse only yields the envelope of the electric field component. However, if the duration of a pulse corresponds to only a few dozens optical wavelengths, as for femtosecond pulses, the spectral phase of the electromagnetic wave is also essential for the temporal characterization.

Ultrashort laser pulses are generated via modelocking, that is an in-phase superposition of different electromagnetic waves centered around a central frequency [28, ch. 8.3]. Owing to a wavelength-dependent speed of light, propagation of a laser pulse through a dispersive material, for example glass, induces a phase difference of the spectral components that in turn results in temporal pulse broadening [28, ch. 17.1]. In order to compensate for such effects, it is desirable to know about the spectral phase of the pulses.

In order to overcome the aforementioned challenges, sophisticated methods for temporal pulse characterization have been developed [30; 31]. Typically, these methods are based on the spectral response of a nonlinear optical effect which allows to deduce the spectral

phase. In the case of SHG-FROG (second harmonic generation – frequency-resolved optical gating) [32–34], the employed nonlinearity is second harmonic generation. The required temporal resolution is achieved by sampling a pulse with a replica of itself. Finally, the spectral phase can be extracted from the spectral response via an iterative algorithm.

In the following, a novel phase-retrieval method based on QUIC is presented. Similar to SHG-FROG, the pulse is sampled by a replica of itself and its second harmonic. However, because of its explicit phase dependence, QUIC directly allows to extract the spectral phase of the pulses by calculating the Fourier transform of one current interferogram without the need for a complex algorithm.

The underlying theoretical concept of phase-retrieval is outlined in chapter 5.1 after a short introduction into the general characterization of ultrashort laser pulses. Chapter 5.2 focuses on the experimental implementation of the new method as well as SHG-FROG that is used as reference. By a comparison of both methods for laser pulses with different spectral phases, phase-retrieval via QUIC is finally evaluated in chapter 5.3.

Parts of the results that are presented within this chapter have already been published in reference [45] and are in preparation for publication elsewhere [46].

5.1 Theoretical Background of Spectral Phase-Retrieval

The proposed method to retrieve the spectral phase of a pulse is based on QUIC. It utilizes the interference of a fundamental laser beam and its second harmonic. The underlying theory of the method is presented in detail in this chapter. But first, a short introduction into the characterization of ultrashort laser pulses is given.

Characterization of Ultrashort Laser Pulses

Concerning the temporal behavior, the electric field amplitude of a laser pulse can typically be approximated by a Gaussian envelope which is modulated by a carrier wave [27, ch. 22.1]:

$$E(t) \propto \exp\left[-2\ln(2)\left(\frac{t}{t_\mathrm{p}}\right)^2\right] \exp\left(\mathrm{i}\omega_0 t\right) + \text{c.c.} \tag{5.1}$$

The angular frequency ω_0 determines the central wavelength of the wave packet. Here, the envelope is chosen in such a way that t_p represents the common definition of the pulse duration, the full width at half maximum (FWHM) of the intensity given by $I \propto |E|^2$.

Intensity autocorrelation constitutes a typical method to determine the FWHM experimentally [27, p. 1002f; 28, p. 489ff]. As sketched in Fig. 5.1, the laser pulse is split up and superimposed with itself in a nonlinear crystal. One of the three emerging frequency-doubled beams is generated by frequency-mixing of both incoming pulses and only present

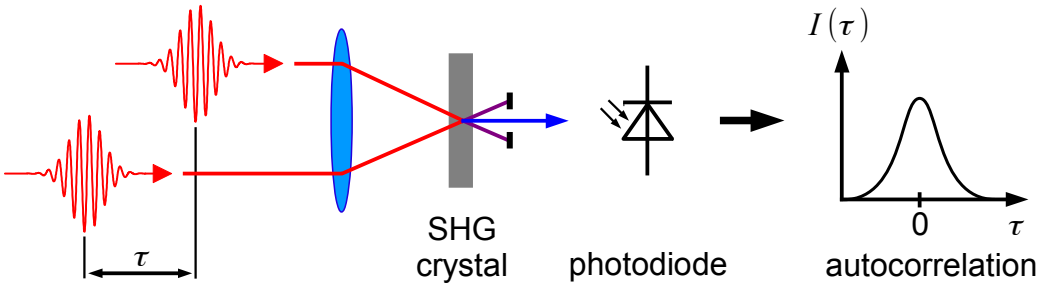

Fig. 5.1: Experimental scheme of intensity autocorrelation: Two delayed laser pulse replicas are superimposed in a nonlinear crystal. The intensity of the central emerging frequency-mixed beam is recorded with a photodiode as a function of the relative delay τ. The temporal width of the resulting autocorrelation signal is related to the laser pulse width.

if these overlap spatially as well as temporally. Its intensity is recorded by a photodiode as a function of the delay τ between the two incoming pulses. The resulting curve corresponds to an autocorrelation, thus giving the method its name. With respect to laser pulses with a Gaussian envelope as described in equation 5.1, the FWHM of the autocorrelation signal ($\mathrm{FWHM_A}$) is directly related to the pulse duration t_p via $t_\mathrm{p} = \mathrm{FWHM_A}/\sqrt{2}$.

While intensity autocorrelation is an appealing method owing to its simple setup, it also inherits critical limitations that have to be taken into account. Obviously, an autocorrelation is always symmetric with respect to the time axis. Therefore, it does not allow to reconstruct the actual pulse envelope and may conceal a deviation from the typical assumption of a Gaussian. As a direct consequence, it is impossible to derive the spectral phase of a laser pulse from intensity autocorrelation.

The spectral phase is related to the Fourier representation of $E(t)$:

$$E(t) = \int \hat{E}(\omega) \exp(\mathrm{i}\omega t)\mathrm{d}\omega \tag{5.2}$$

Here, $\hat{E}(\omega)$ denotes the Fourier transform of $E(t)$. As a complex function, $\hat{E}(\omega)$ can also be expressed as $\hat{E}(\omega) = |\hat{E}(\omega)| \cdot \exp\left(-\mathrm{i}\phi(\omega)\right)$, separating the spectral amplitude $|\hat{E}(\omega)|$ from the spectral phase $\phi(\omega)$. The spectral amplitude $|\hat{E}(\omega)|$ can easily be retrieved from a spectral measurement of a pulse. To illustrate the influence of the spectral phase, two exemplary laser pulses are discussed.

Fig. 5.2 depicts the electric field amplitude of two pulses in time-domain as well as frequency-domain connected via Fourier transformation. Both pulses feature the same Gaussian spectral amplitude. However, their temporal shapes differ because of the different spectral phases. The left pulse exhibits a flat spectral phase, that is, all spectral components are in phase, also called mode-locked. In this case, the pulse duration is only determined by the width of the spectrum via the time-bandwidth product $\Delta\omega \cdot t_\mathrm{p} = 2\pi \cdot 0.44$ [27, p. 938]. Consequently, such pulses are called transform-limited or bandwidth-limited. For

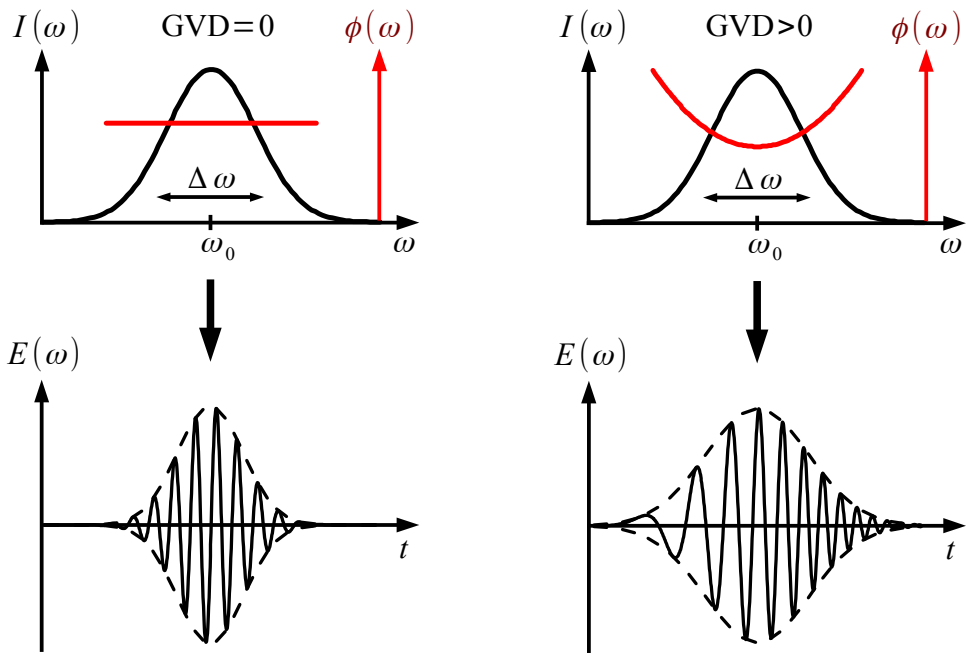

Fig. 5.2: Spectral and temporal representation of a transform-limited pulse (left) and a pulse with positive GVD (right). Both pulses feature the same spectral bandwidth $\Delta\omega$. The phase curvature on the right side results in temporal broadening.

a fixed spectral width $\Delta\omega$, the equation also marks the minimum possible pulse duration. A deviation from the Gaussian spectral amplitude or the flat phase results in a longer pulse duration.

If the pulse propagates through a dispersive medium, the spectral phase changes. Owing to the frequency-dependent speed of light, different frequency components propagate with a different velocity. To quantify this dispersion, the Taylor expansion of the spectral phase centered around the central frequency ω_0 is employed [28, p. 466ff]:

$$\phi_{\omega_0}(\omega) = \phi(\omega_0) + \phi'(\omega_0)(\omega - \omega_0) + \frac{1}{2}\phi''(\omega_0)(\omega - \omega_0)^2 + \mathcal{O}(\omega^3) \tag{5.3}$$

Linear terms correspond to an overall delay of the pulse that does not affect the envelope of the pulse. Concerning the pulse duration, only the quadratic and higher-order terms are relevant. If these are nonzero, the pulse is said to be "chirped". For typical experimental scenarios involving dispersion by common glass substrates, the quadratic term dominates [29, p. A150ff]. It is characterized by the curvature $\phi''(\omega_0)$, the group velocity dispersion (GVD) which is denoted by ϕ''_{ω_0} in the following. Higher-order terms are usually at least an order of magnitude smaller.

The right part of Fig. 5.2 depicts a chirped pulse with a positively curved spectral phase (GVD > 0). In contrast to the unchirped transform-limited pulse on the left, the spectral components are out of phase and delayed with respect to each other; the longer

wavelength components precede the shorter wavelength parts. As a direct consequence, the pulse broadens. For a purely quadratic phase the resulting pulse duration t_p can be calculated via the following analytic expression with t_0 denoting the FWHM of the corresponding transform-limited pulse [28, p. 470ff]:

$$t_\mathrm{p} = t_0 \left[1 + \left(\frac{4 \ln(2)\, \phi''_{\omega_0}}{t_0^2} \right)^2 \right]^{1/2} \tag{5.4}$$

Evidently, broadening by GVD becomes more relevant with shorter pulses, specifically in the range of 100 fs or less. On the one hand, short pulses feature a broad spectrum according to the time-bandwidth product, making them susceptible to dispersion. On the other hand, a slight broadening by a few femtoseconds has only a relatively small impact if the pulse duration is in the order of picoseconds.

Since phase-induced pulse broadening is a reversible process, a positive phase curvature may be compensated by introducing a material with a negative GVD. Therefore, it is desirable to know about the spectral phase. However, the phase is not directly accessible as only the intensity of the pulses ($I \propto |E|^2$) can directly be measured wherein the phase cancels out. This has led to the development of more advanced concepts [30; 31], most notably the class of MIIPS (multiphoton intrapulse interference phase scan) [95; 96], FROG (frequency-resolved optical gating) [32–34; 97] and SPIDER (spectral phase interferometry for direct electric field reconstruction) [98–101]. In the case of MIIPS, the spectral phase is derived from the response of SHG to an additional phase modification by a pulse shaper. Similar to intensity autocorrelation, the latter two methods are based on a superposition of pulse replicas employing non-linear effects. The spectral phase is retrieved with the use of additional information, namely the spectrum as well as interference. A detailed description of SHG-FROG (second harmonic generation – FROG) is given in chapter 5.2.

Here, a new method for phase-retrieval based on QUIC is proposed and experimentally demonstrated. Most notably, the underlying nonlinearity explicitly depends on the spectral phase. In essence, the spectral phase of the pulses can be directly retrieved from the Fourier transform of only one current interferogram.

Derivation of Phase-Retrieval via QUIC

In the following, the theoretical derivation of the proposed phase-retrieval method is sketched. To begin with, it is instructive to recall equation (2.12) that describes the current injection rate of QUIC. For reasons of clarity, the complex conjugated terms are omitted in the following:

$$\frac{\mathrm{d}J^a}{\mathrm{d}t} = \eta_3^{abcd}(\omega)\, \overline{E^b(\omega)}\, \overline{E^c(\omega)}\, E^d(2\omega) \tag{5.5}$$

In comparison with the relation $I \propto E \cdot \overline{E}$ that describes the intensity of an electric field, the current injection rate additionally depends linearly on the electric field amplitude of the second harmonic field. As a consequence, current injection explicitly depends on the optical phase, in contrast to an intensity measurement where the phase cancels out. The explicit phase dependence of QUIC has been previously utilized for optical spectroscopy of a material by placing it into the interferometer [23; 24]. In that case, the laser pulses are merely a tool to characterize the material.

Here, it is shown that the phase dependence of QUIC can be further utilized to retrieve the absolute phase of the incoming laser pulses on the basis of one current interferogram. To this end, the delay between a certain combination of fundamental and second harmonic electric field components is swept during the measurement. It should be emphasized that the aim of the proposed method is to characterize the fundamental beam; the second harmonic field $E_{2\omega}$ merely serves as an intermediate product. For this reason, whenever the GVD is mentioned, it refers to the fundamental pulses if not stated otherwise.

In practice, the fundamental laser pulses are frequency-doubled in a nonlinear crystal to provide $E_{2\omega}$. Subsequently, the beams are split up in an interferometer as displayed in Fig. 5.3. An arm with a fixed length contains a portion of the fundamental beam with the electric field amplitude $E_\omega^{(2)}(t)$. The other arm contains a simultaneous pulse pair consisting of both the fundamental beam and its second harmonic. Their respective electric field amplitudes are denoted with $E_\omega^{(1)}(t+\tau)$ and $E_{2\omega}(t+\tau)$. By varying the length of the second arm, the delay τ is adjusted. Finally, the pulse triplet is collinearly focused

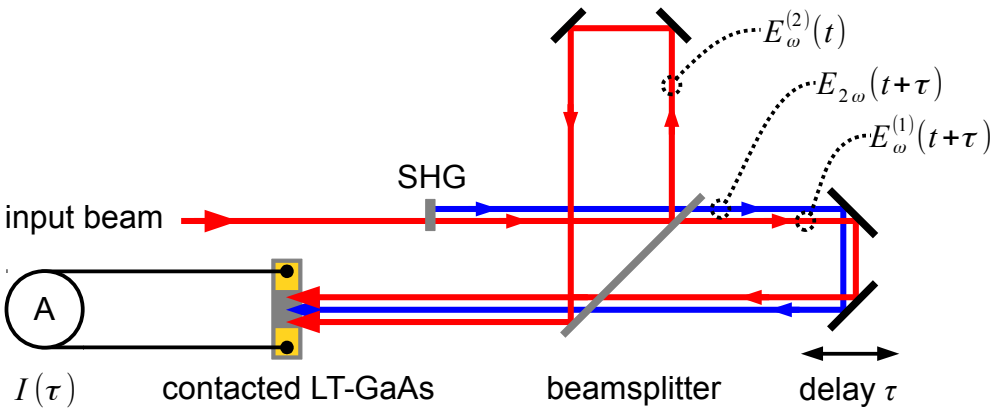

Fig. 5.3: Experimental scheme of the proposed phase-retrieval method: The pulses to be characterized are frequency-doubled in a nonlinear crystal. An interferometer allows to control the relative delay τ between a portion of the fundamental field component $E_\omega^{(2)}(t)$ and an overlapping pulse pair consisting of both a fundamental component $E_\omega^{(1)}(t+\tau)$ and the second harmonic component $E_{2\omega}(t+\tau)$. All beams are collinearly focused on a contacted LT-GaAs sample. The injected current $I(\tau)$ is measured as a function of the relative delay τ.

onto a contacted LT-GaAs sample; the injected current is measured as a function of the delay τ. Every data point of the resulting current interferogram corresponds to a temporal integration of the current injection rate (5.5) for a fixed delay τ: $I(\tau) \propto \int \dot{J}(t,\tau)\,\mathrm{d}t$.

Since there are two separate fundamental laser beams, there are three different potential field combinations for equation (5.5):

1. $\overline{E_\omega^{(2)}(t)}\,\overline{E_\omega^{(2)}(t)}\,E_{2\omega}(t+\tau)$
2. $\overline{E_\omega^{(2)}(t)}\,\overline{E_\omega^{(1)}(t+\tau)}\,E_{2\omega}(t+\tau)$
3. $\overline{E_\omega^{(1)}(t+\tau)}\,\overline{E_\omega^{(1)}(t+\tau)}\,E_{2\omega}(t+\tau)$

In the first and third case, the fundamental electric field components both stem from only one fundamental beam, $E_\omega^{(1)}$ or $E_\omega^{(2)}$, respectively. In the second case, the fundamental field components originate from different interferometer arms. Obviously, there is only one option for $E_{2\omega}$.

Different field combinations result in different dependences of the corresponding current components on the delay τ. If all field amplitudes stem from one interferometer arm, as in the third case, the resulting current is independent of the delay τ. Consequently, it manifests as a constant offset in the current interferogram and does not contain any phase information. In contrast, the other two contributions oscillate with respect to the delay τ. The first case is equivalent to the interferometric current injection discussed in chapter 3.3. As both fundamental field amplitudes are delayed with respect to $E_{2\omega}$, the corresponding current interferogram oscillates with the central angular frequency $2\omega_0$. In the second case, however, only one fundamental field component is delayed with respect to the remaining fields resulting in the oscillation frequency ω_0. Utilizing the substitution $t' = t+\tau$ both current components can be expressed as convolutions of the form $(f*g)(\tau) = \int f(\tau - t')g(t')\,\mathrm{d}t'$:

$$I_1(\tau) \propto \int_{-\infty}^{+\infty} \overline{E_\omega^{(2)}(t'-\tau)}\,\overline{E_\omega^{(2)}(t'-\tau)}\,E_{2\omega}(t')\,\mathrm{d}t' = \left(\overline{E_\omega^{(2)}(-\tau)}\right)^2 * E_{2\omega}(\tau) \tag{5.6}$$

$$I_2(\tau) \propto \int_{-\infty}^{+\infty} \overline{E_\omega^{(2)}(t'-\tau)}\,\overline{E_\omega^{(1)}(t')}\,E_{2\omega}(t')\,\mathrm{d}t' = \overline{E_\omega^{(2)}(-\tau)} * \left(\overline{E_\omega^{(1)}(\tau)} \cdot E_{2\omega}(\tau)\right) \tag{5.7}$$

In the following, it is shown that the spectral phase of the fundamental laser pulse, particularly its GVD, is deducible from the spectral phases of the two oscillating current contributions by rather simple relations. The spectral phases of both current contributions are in turn accessible from the Fourier transform $\mathcal{F}$ of only one current interferogram. Since the injected currents of both components can be described as vectors, it is assumed that they are superimposed linearly in the interferogram. The exact relation depends on

experimental extraction efficiencies, the injection amplitude and injection direction given by the tensor η_3. However, an exact quantification of the current amplitudes is not necessary since only the spectral phase of the Fourier transform is crucial for the following derivation.

Fig. 5.4 displays the general concept for the retrieval of the spectral phase from the Fourier transform of the measured current interferogram. The envelope of the interferogram results from the convolution of the three pulses. The different frequencies of the two current components manifest as beating pattern. By taking the Fourier transform, both current components can be separated. They appear as peaks at the frequencies ω_0 and $2\omega_0$ with the respective spectral phases Φ_ω and $\Phi_{2\omega}$. For this reason, both components can be treated separately in the theoretical approach. Finally, the spectral phase of the laser pulses, in specific their GVD, can be computed on the basis of Φ_ω and $\Phi_{2\omega}$.

Owing to the convolution theorem $\mathcal{F}\{f * g\} = \mathcal{F}\{f\} \cdot \mathcal{F}\{g\}$ and its equivalent $\mathcal{F}\{f \cdot g\} = \mathcal{F}\{f\} * \mathcal{F}\{g\}$, the Fourier transforms factorize into the Fourier transforms of the electric fields:

$$\mathcal{F}\{I_1\}(\omega) \propto \mathcal{F}\left\{\left(\overline{E_\omega^{(2)}(-\tau)}\right)^2\right\} \cdot \mathcal{F}\left\{E_{2\omega}(\tau)\right\} = \left(\overline{\hat{E}_\omega^{(2)}(\omega)} * \overline{\hat{E}_\omega^{(2)}(\omega)}\right) \cdot \hat{E}_{2\omega}(\omega) \tag{5.8}$$

$$\mathcal{F}\{I_2\}(\omega) \propto \mathcal{F}\left\{\overline{E_\omega^{(2)}(-\tau)}\right\} \cdot \mathcal{F}\left\{\overline{E_\omega^{(1)}(\tau)} \cdot E_{2\omega}(\tau)\right\} = \overline{\hat{E}_\omega^{(2)}(\omega)} \cdot \left(\overline{\hat{E}_\omega^{(1)}(-\omega)} * \hat{E}_{2\omega}(\omega)\right) \tag{5.9}$$

Here, $\hat{E}(\omega)$ denotes the Fourier transform of $E(\tau)$. The arguments τ and ω refer to the delay and the angular frequency of the Fourier transform, respectively. The argument ω should not be confused with the index that distinguishes fundamental and second harmonic

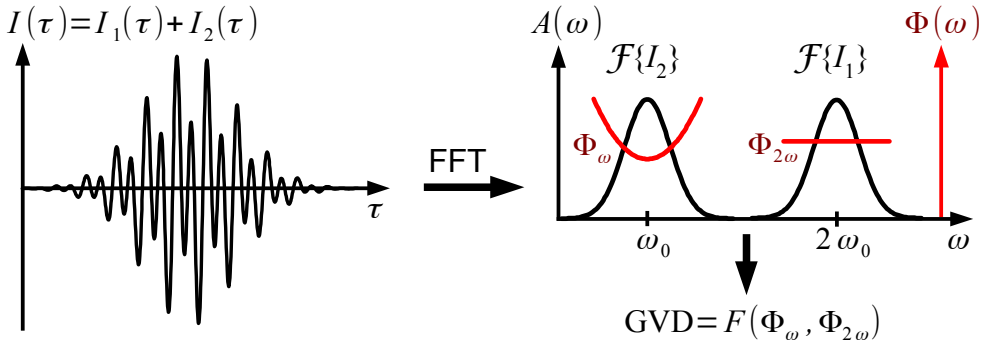

Fig. 5.4: Procedure for phase-retrieval of a laser pulse based on QUIC: A specific combination of the fundamental laser pulse and its second harmonic is superimposed on a contacted LT-GaAs sample (cf. Fig. 5.3). The photoresponse is recorded as a function of the relative pulse delay τ. The resulting current interferogram corresponds to a superposition of two convoluted electric field combinations that feature different oscillation periods. Both convolutions I_1 and I_2 are separated by calculating the Fourier transform. Based on the spectral phases Φ_ω and $\Phi_{2\omega}$ of the Fourier transform centered around the respective oscillations frequency, the spectral phase of the incident laser pulses, particularly their GVD, can be computed.

components. Furthermore, it is important to pay attention to the sign of the arguments. For example, the expression $\hat{E}(-\omega)$ represents the Fourier transform of $E(\tau)$, wherein the sign of ω is inverted afterwards. Moreover, the order of the Fourier transform and the complex conjugation is interchanged in the above expressions according to the relation $\mathcal{F}\{\,\overline{f(\tau)}\,\} = \overline{\hat{f}(-\omega)}$. If the pulses experience the same, preferably negligible, dispersion in the interferometer arms, it can be assumed that $\hat{E}_\omega^{(1)} = \hat{E}_\omega^{(2)} = \hat{E}_\omega$. The resulting equations directly relate the Fourier transforms of the experimental current interferograms on the left-hand-side with the Fourier transforms of the pulses' electric fields on the right-hand side.

Initially, the theory of QUIC is formulated for monochromatic waves. Here, it is assumed that equation (5.5) and subsequently the two equations above are also valid for wave packets, implying a frequency-independent constant η_3. As the spectral width of laser pulses is relatively small ($\Delta\omega = 7 \cdot 10^{11}$ Hz for a 100 fs pulse, according to the time-bandwidth product) the assumption seems justified. Furthermore, the good agreement of the experimental results with the reference measurements (see chapter 5.3) corroborates the assumption a posteriori.

To derive the relation of the spectral phases, the Fourier transforms in equations (5.8) and (5.9) are each expressed as a product of the corresponding spectral amplitude and an exponential phase factor. For clarity, the phase of the current interferogram is denoted with Φ and the phase of the electric fields with ϕ. In the following, the spectral amplitudes $|\hat{E}(\omega)|$ of the fundamental and second harmonic pulses are modeled by Gaussian envelopes centered around ω_0 and $2\omega_0$, respectively. In principal, the two equations above can also be solved numerically for other pulse envelopes. However, a Gaussian spectrum constitutes the typical situation for an ultrashort pulse laser. In this case, the equations for the GVD can be solved analytically and result in simple relations.

Mathematically, the Fourier transforms $\hat{E}(\omega)$ of the fundamental electric wave packet and its second harmonic are described by Gaussian functions. As above, the index ω and 2ω mark the fundamental and second harmonic pulse:

$$\hat{E}_\omega(\omega) \propto \exp\left(-\frac{t_{\mathrm{p}_0,\omega}^2(\omega-\omega_0)^2}{\ln(256)}\right)\exp(-\mathrm{i}\phi_\omega(\omega)) \tag{5.10}$$

$$\hat{E}_{2\omega}(\omega) \propto \exp\left(-\frac{t_{\mathrm{p}_0,2\omega}^2(\omega-2\omega_0)^2}{\ln(256)}\right)\exp(-\mathrm{i}\phi_{2\omega}(\omega)) \tag{5.11}$$

The first factors in equation (5.10) and (5.11) correspond to Fourier transforms of bandwidth-limited pulses described by equation (5.1). Via the exponential phase factors, the influence of dispersion is incorporated (cf. equation (5.2)). The phases $\phi_\omega(\omega)$ and $\phi_{2\omega}(\omega)$ are represented by the Taylor expansion (5.3). As mentioned above, GVD is

typically the dominant influence on the pulse duration as long as the dispersion is not too high. If the higher-order terms are neglected, the equations (5.8) and (5.9) can be solved analytically for the resulting Fourier transforms $\hat{E}_{\omega}(\omega)$ and $\hat{E}_{2\omega}(\omega)$.

First, the convolutions and products of the Fourier transforms on the right-hand side of equations (5.8) and (5.9) are calculated. This results in two Gaussian-like peaks that are centered around ω_0 and $2\omega_0$. The corresponding exponential phase factors are sorted by the order of ω whereby only the second order ω^2 of the phase factor is relevant for the pulse duration. Hence, the right-hand sides of the equations are rewritten in the form $A_{\omega_0} \cdot \exp\left[\mathrm{i}/2 \cdot D_{\omega_0} \cdot (\omega - \omega_0)^2\right]$ and $A_{2\omega_0} \cdot \exp\left[\mathrm{i}/2 \cdot D_{2\omega_0} \cdot (\omega - 2\omega_0)^2\right]$. Evidently, D_{ω_0} and $D_{2\omega_0}$ correspond to the curvature of the spectral phase on the left-hand side, i.e. to the Fourier transform of the current components. Therefore, the calculations directly relate the phase curvature of the current interferogram to the respective GVD ϕ''_{ω_0} and $\phi''_{2\omega_0}$ of the fundamental and second harmonic pulses:

$$D_{\omega_0} = \frac{\ln(16)\left(\phi''_{\omega_0}\left(16\ln(2)^2(\phi''_{2\omega_0}-\phi''_{\omega_0})^2+\left(t^2_{\mathrm{p}_0,2\omega}+t^2_{\mathrm{p}_0,\omega}\right)^2\right)+16\phi''_{2\omega_0}\phi''_{\omega_0}\ln(2)^2(\phi''_{2\omega_0}-\phi''_{\omega_0})-\phi''_{2\omega_0}t^4_{\mathrm{p}_0,\omega}+\phi''_{\omega_0}t^4_{\mathrm{p}_0,2\omega}\right)}{64\ln(2)^3(\phi''_{2\omega_0}-\phi''_{\omega_0})^2+4\ln(2)\left(t^2_{\mathrm{p}_0,2\omega}+t^2_{\mathrm{p}_0,\omega}\right)^2} \tag{5.12}$$

$$D_{2\omega_0} = \frac{1}{2}\phi''_{\omega_0} - \phi''_{2\omega_0} \tag{5.13}$$

The widths t_{p_0} refer to the respective transform-limited pulse length that can be extracted from a spectral measurement utilizing the time-bandwidth product. If the dispersion is not too high, i.e. if $|\phi''_{\omega_0}|, |\phi''_{2\omega_0}| \ll t^2_{\mathrm{p}_0,\omega}, t^2_{\mathrm{p}_0,2\omega}$, equation (5.12) can be simplified further. On the one hand, it can be assumed that the width of the fundamental pulse and its second harmonic, generated with a thin nonlinear crystal, are related via $t_{\mathrm{p}_0,2\omega} = t_{\mathrm{p}_0,\omega}/\sqrt{2}$ [102]. On the other hand, the terms ϕ'' can be neglected with respect to $t^2_{\mathrm{p}_0}$. Mathematically, these assumptions are equivalent to the calculation of the limit $t_{\mathrm{p}_0,2\omega} = t_{\mathrm{p}_0,\omega}/\sqrt{2} \to \infty$ that simplifies the equation for D_{ω_0}:

$$D_{\omega_0} = \frac{10}{9}\phi''_{\omega_0} - \frac{4}{9}\phi''_{2\omega_0} \tag{5.14}$$

By rearranging the two linear equations (5.13) and (5.14), the relations for the GVD can be obtained:

$$\phi''_{\omega_0} = \frac{9}{8}D_{\omega_0} - \frac{1}{2}D_{2\omega_0} \tag{5.15}$$

$$\phi''_{2\omega_0} = \frac{9}{16}D_{\omega_0} - \frac{5}{4}D_{2\omega_0} \tag{5.16}$$

Ideally, the pulses do not experience additional dispersion in the interferometer. In this case, the GVD of the second harmonic pulse should be half the GVD of the fundamental pulse [102] implying $D_{2\omega_0} = 0$ according to equation (5.13). As a result, the system of two equations simplifies to only one equation; the GVD of the pulses only depends on the

phase curvature of the current's Fourier transform centered around the angular frequency ω_0. Therefore, the curvature centered around the angular frequency $2\omega_0$ is not needed in this approximation:

$$\phi''_{\omega_0} = \frac{9}{8} D_{\omega_0} \tag{5.17}$$

Although not as instructive as the analytic derivation above, the relation of the spectral phases can also be calculated numerically. To this end, the electric field amplitudes $E(t)$ in the current injection equation (5.5) are modeled by chirped pulses with a Gaussian envelope. Afterwards, the respective Fourier transforms of the current interferograms are computed numerically. Their spectral phases are extracted under the above mentioned assumption of low chirp and with the relation $t_{\mathrm{p}_0,2\omega} = t_{\mathrm{p}_0,\omega}/\sqrt{2} \to \infty$. Besides a confirmation of the analytic equations, the computation reveals that there are similar relations for the third order of the phase. The third derivatives of the Fourier transform phase $D^{(3)}$ and the third derivatives ϕ''' of the pulse phase also depend linearly on each other:

$$D^{(3)}_{\omega_0} = \frac{26}{27}\phi'''_{\omega_0} - \frac{8}{27}\phi'''_{2\omega_0} \tag{5.18}$$

$$D^{(3)}_{2\omega_0} = \frac{1}{4}\phi'''_{\omega_0} - \phi'''_{2\omega_0} \tag{5.19}$$

In conclusion, the proposed method constitutes a straightforward technique to reconstruct the phase of laser pulses, particularly their GVD. Because of the explicit phase dependence of QUIC, the phase information of the pulses can be extracted directly from the Fourier transform of one current interferogram without the need for a complex algorithm. The experimental realization of this method is described in the following chapter. The results and the validity of the simplifying assumptions are discussed in chapter 5.3. In essence, the results are in good agreement with the reference measurements for typical experimental scenarios and the simplifications prove to be justified.

5.2 Experimental Implementation

In order to benchmark the proposed phase-retrieval concept, it is compared with an already well-established method. To this end, differently chirped pulses are consecutively characterized via the proposed method and SHG-FROG. The experimental setup can be divided into three parts (see Fig. 5.5): The spectral phase of the pulses is directly manipulated at the laser output by inserting glass slabs into the beam path. The slabs simulate the typical origin of pulse broadening, namely propagation through dispersive components like lenses. Subsequently, a flip-mirror allows to alternatively steer the manipulated laser beam into

the QUIC setup or an SHG-FROG setup that is used for reference. The details of these three parts are elucidated in the following.

Phase Manipulation of Ultrashort Laser Pulses

The phase-retrieval method is exemplarily demonstrated at the OPA laser system described in chapter 3.1. It delivers ultrashort laser pulses with a duration of 45 fs at a repetition rate of 250 kHz. The central wavelength is tuned to 1450 nm and satisfies the energy relation $\hbar\omega < E_\mathrm{G} < 2\hbar\omega$ for GaAs. A telescope is used to compensate the beam divergence; polarization optics ensure a well-defined vertical polarization of the beam.

The chirp of the pulses is manipulated by inserting different glass slabs into the beam path. Upon their propagation through the glass, the pulses acquire a significantly different spectral phase $\phi(\omega)$, particularly a different GVD. Essentially, the sign of the GVD is determined by the choice of the material; the magnitude is determined by the thickness of the inserted glass slab. To identify the appropriate materials and to calculate the expected change of the GVD, the Sellmeier equation is used. The Sellmeier equation describes a material's refractive index n as a function of the (vacuum) wavelength λ via the empirical material-dependent Sellmeier coefficients A_i and B_i [103]:

$$n^2 = 1 + \frac{A_1\lambda^2}{\lambda^2 - B_1^2} + \frac{A_2\lambda^2}{\lambda^2 - B_2^2} + \frac{A_3\lambda^2}{\lambda^2 - B_3^2} \tag{5.20}$$

A pulse that passes through a material with refractive index n and thickness d experiences a phase difference given by $\Delta\phi = 2\pi/\lambda \cdot (n-1) \cdot d$ when compared to propagation through a volume of air with the same thickness ($n_\mathrm{air} \approx 1$). Substituting $\lambda = 2\pi \cdot c/\omega$ allows to derive the GVD, the second derivative of the phase with respect to the angular frequency ω. Here, c denotes the vacuum speed of light. Like the refractive index n, the GVD depends on the wavelength. Typically, a material is characterized by the GVD per length in units of $\mathrm{fs}^2/\mathrm{cm}$.

To impose a positive as well as a negative GVD, two different types of glass are chosen, namely SF11 made by *SCHOTT* and the quartz glass Infrasil made by *HERAEUS*. For the given central wavelength of 1450 nm, they exhibit a GVD of $+620\ \mathrm{fs}^2/\mathrm{cm}$ and $-160\ \mathrm{fs}^2/\mathrm{cm}$, respectively. Slabs with different thicknesses in the range from a few millimeters to several centimeters are prepared to provide a GVD change in the range from about $-500\ \mathrm{fs}^2$ to $+1000\ \mathrm{fs}^2$. Each set of slabs is cut from the same bar to ensure that all pieces of the same material exhibit the same optical properties. Special care is taken during the polishing process to maintain plane parallelism of the opposing surfaces. Otherwise, the beam would be deflected by one of the surfaces.

The glass slabs are mounted in a special holder that allows to accurately adjust their rotation in order to minimize beam deflection. For this purpose, the slab is tilted until

the surface reflections are directed into the path of the incoming beam indicating normal incidence. The deflection can be monitored with a camera in the QUIC setup.

After adjustment of a glass slab, the laser beam is consecutively directed into the QUIC setup as well as into the SHG-FROG setup via a flip mirror. Both measurement procedures only take a few minutes. In this way, it is ensured that neither a different alignment of the glass slabs nor long-term instabilities of the laser may distort the comparison.

QUIC Setup

Conceptually, the experimental setup for the proposed phase-retrieval method is similar to the setup described in chapter 3.2. However, there are some significant modifications with respect to the interferometer and the detection. The method requires one electric field component $E_\omega^{(2)}$ of the fundamental beam to be delayed against a pulse pair consisting of another portion $E_\omega^{(1)}$ of the fundamental beam and a field component $E_{2\omega}$ of the second harmonic beam. One way to realize such a scheme is to construct a three arm interferometer wherein every field component propagates through its own arm. Here, a modified two-arm interferometer is used with the advantage of reduced complexity. The apparent downside of such a setup is that it requires low dispersion to ensure a simultaneous propagation of the pulse pair. However, as the method's aim is to derive the phase of the pulses, this condition must be fulfilled in any case. Otherwise, the phase would be significantly altered by the setup itself. For this reason, reflective or thin optics are used whenever possible.

The experimental setup is sketched in Fig. 5.5. After modification by glass slabs, the beam is focused into a 0.5 mm thick BBO crystal to generate the second harmonic beam. Although BiBO has a higher conversion efficiency, a BBO crystal is chosen since it results in a lower dispersion for both beams. For example, the GVD of the second harmonic beam, induced by the 0.5 mm thick BBO crystal, is only a few tens fs^2 compared to almost 100 fs^2, induced by a BiBO crystal of the same thickness. Yet, the BBO crystal is sufficient to generate about 1 mW of second harmonic beam from the incoming 20 mW fundamental beam. Both, the vertically polarized fundamental beam and the horizontally polarized second harmonic beam are collimated by a spherical mirror and directed into the subsequent interferometer.

Two pellicles serve as beamsplitter and combiner in the interferometer. The pellicles consist of 2 µm nitrocellulose films, causing negligible dispersion. In contrast to a dichroic beamsplitter, the pellicles transmit and reflect portions of both beams. Consequently, the second harmonic beam in one arm must be filtered to realize the desired field combinations. Besides, interference of two second harmonic beams would severely perturb the measurement as their photon energy exceeds the band gap of GaAs.

The strong absorption of photons exceeding the band gap can in turn be utilized to

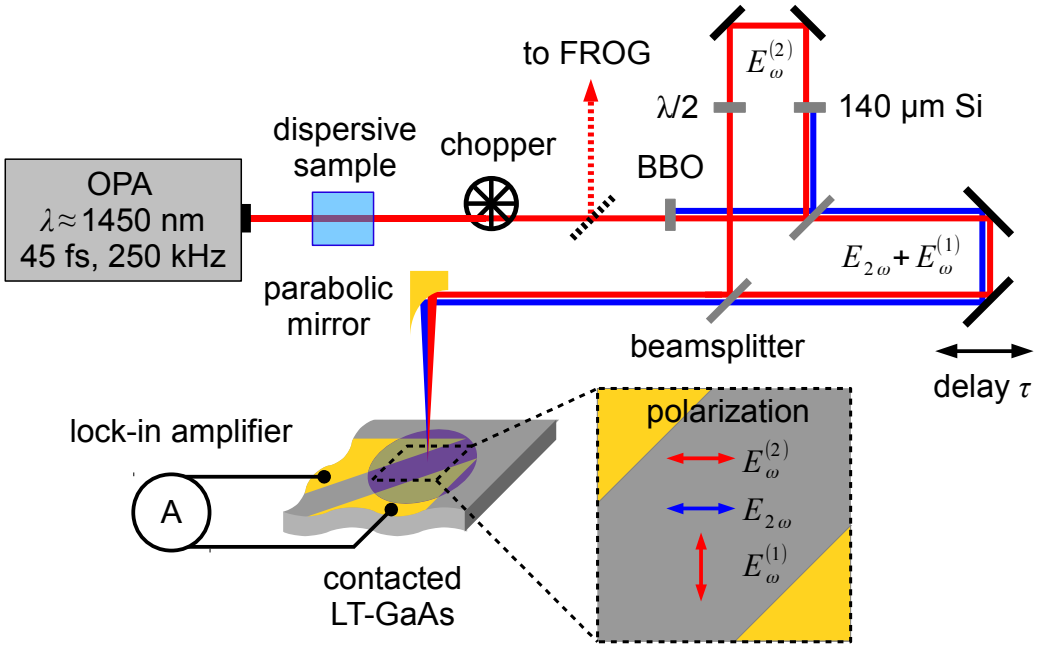

Fig. 5.5: Experimental setup of the proposed phase-retrieval method: The pulses of an ultrashort laser source are frequency-doubled in a 0.5 mm thick BBO. An interferometer allows to control the relative polarization and delay τ of a portion of the fundamental field component $E_\omega^{(2)}$ and an overlapping pulse pair consisting of both a fundamental component $E_\omega^{(1)}$ and the second harmonic component $E_{2\omega}$. All beams are collinearly focused on the ≈ 10 µm wide gap of two metallic contacts on top of an LT-GaAs sample. The inset illustrates the alignment of the sample and the optical polarizations. A lock-in amplifier records the injected current. A flip-mirror in front of the BBO allows to steer the laser pulses into a reference SHG-FROG setup. Dispersive glass samples put right behind the laser output allow to control the pulses' spectral phase. To minimize dispersion of the setup itself, reflective or thin optics are used.

realize an efficient low-dispersive longpass filter. Placing a 140 µm thick silicon wafer piece into the reflected path of the interferometer is sufficient to entirely block the second harmonic beam while attenuating the fundamental beam only slightly and adding a GVD of only 140 fs^2 to the latter beam. To further minimize reflection losses at the surface, the wafer piece is oriented at Brewster's angle. Additionally, the polarization of this fundamental beam is rotated by 90° with a 90 µm thick half-wave plate for reasons that are elucidated below. The electric field component of the fundamental beam in this arm with a fixed length is denoted with $E_\omega^{(2)}(t)$.

The electric field components of the pulse pair in the other arm are denoted with $E_\omega^{(1)}(t+\tau)$ and $E_{2\omega}(t+\tau)$. Apart from a retroreflector, there are no additional optical components in the arm to prevent dispersion of the pulse pair. The retroreflector is mounted on the motorized stage that allows to precisely adjust the delay τ of the pulse pair with respect to the field component $E_\omega^{(2)}(t)$.

All three beams are superimposed by the second pellicle at the exit of the interferometer.

Subsequently, they are focused on a contacted LT-GaAs detector by a parabolic mirror with a focal length of 25 mm. It should be noted that the resulting peak intensities are much lower than in the study of the high-intensity regime of QUIC presented in chapter 4.2 because of the longer focal length. Current measurements are performed with a lock-in amplifier which is connected to the two gold contacts that are spaced about 10 µm apart.

In order to derive the spectral phase of the pulses, it is necessary to measure two different current components simultaneously. As described in chapter 5.1, the current components result from different combinations of the electric fields $E_\omega^{(1)}(t+\tau)$, $E_{2\omega}(t+\tau)$ and $E_\omega^{(2)}(t)$. Depending on whether the fundamental field components in equation (5.5) stem from both interferometer arms or only from one arm, the current component oscillates with the central frequency ω_0 or $2\omega_0$ with respect to the delay τ. The direction and amplitude of the injected current in the GaAs detector is governed by the polarization-dependent tensor η_3. For the given material and wavelength, theoretical calculations predict the nonzero components to be $\eta_3^{xxxx} \approx 2\eta_3^{xxyy} = 2\eta_3^{xyxy}$ and $\eta_3^{xyyx} \ll \eta_3^{xxyy}$ [7] (see also chapter 2.2). Here, the first index determines the current direction, the last index denotes the polarization of the second harmonic beam and the remaining two indices denote the polarization of the fundamental beams; x and y represent perpendicular directions.

To ensure an efficient detection of both current components, the electric field polarizations and the detector have to be aligned according to the tensor components. With the configuration displayed in Fig. 5.5, the current components address the largest tensor elements η_3^{xxxx} and η_3^{yyxx}. The former corresponds to the two beam setup described in chapter 3.2, whereby both horizontal polarized fundamental field components stem from the fixed arm. The second current component is perpendicularly oriented and originates from fundamental field components of differently polarized arms. Turning the detector by about 45° as indicated by the inset in Fig. 5.5 optimizes the simultaneous detection of both current components. If the polarization of $E_\omega^{(2)}(t)$ were not altered by a wave-plate, only the smallest non-zero element η_3^{xyyx} would be addressed. It should be noted that the considerations above assume the x and y directions to coincide with the crystallographic axes. Although this condition is not taken care of, the general conclusions do not change. A deviation from the crystallographic axes can be thought of as superposition of the situations discussed above.

In addition to the current interferogram, the proposed method requires a measurement of the fundamental beam's spectrum to compute the theoretical unchirped pulse length $t_{\mathrm{p}_0,\omega}$. To this end, the spectrum is acquired right behind the glass slabs by a conventional fiber-coupled spectrometer.

SHG-FROG Setup

SHG-FROG (second harmonic generation – FROG), an implementation of the general FROG method (frequency-resolved optical gating), serves as benchmark for the proposed phase-retrieval method. The general concept of FROG was developed by the group of R. Trebino in 1993 [32; 33]. The underlying principle of all FROG methods is the numerical reconstruction of the electric field of a pulse based on its spectrally-resolved response to a nonlinear optical effect. First, FROG was demonstrated utilizing nonlinearities of the refractive index. Shortly after, SHG-FROG was demonstrated [104]. As the name implies, it is based on second harmonic generation [34].

The SHG-FROG setup, sketched in Fig. 5.6, is similar to the setup of intensity autocorrelation (cf. Fig. 5.1). Two pulse replicas with a variable delay τ are noncollinearly superimposed in a nonlinear crystal causing frequency-mixing. In essence, the nonlinear response of one pulse is gated by the second pulse. Unlike intensity autocorrelation, the mixing signal is spectrally resolved as a function of the pulses' delay τ. The resulting dataset is called FROG trace, a 2D map depicting the spectral amplitude of the second harmonic beam as a function of the wavelength and the relative delay τ. The phase information is implicitly incorporated in the trace. An iterative algorithm is able to reconstruct the electric field of the pulse including its spectral phase from the FROG trace.

The algorithm is based on the fact that the field of the mixing signal must comply with two constraints [34]. On the one hand, the signal is generated via frequency-mixing of two identical pulses that are delayed with respect to each other. It follows that the signal field E_{Sig} must be expressible as an autocorrelation of the electric field E of the pulses. Here, E_{Sig} is a two-dimensional function, describing the envelope of the electric field as a function

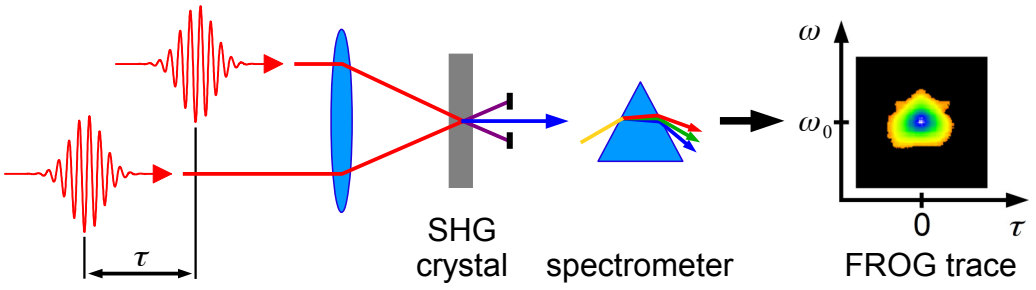

Fig. 5.6: Experimental scheme of SHG-FROG: Similar to intensity autocorrelation (cf. Fig. 5.1) two laser pulse replicas are superimposed in a nonlinear crystal. The emerging central frequency-mixed beam is fed into a spectrometer. The measurement yields a color-coded intensity map as a function of the optical frequency ω and the relative delay τ. Based on this FROG trace, an iterative algorithm is able to reconstruct the input pulse.

of the time t and the delay τ:

$$E_{\mathrm{Sig}}(t,\tau) \propto E(t)E(t-\tau) \tag{5.21}$$

On the other hand, the spectral intensity of E_{Sig} must correspond to the experimental FROG trace. Because of its influence on the pulses' envelope, the spectral phase manifests implicitly in the FROG trace. As stated above, a deviation from a flat phase corresponds to a delay of the spectral components (cf. Fig. 5.2). Therefore, the leading and trailing edge of a chirped pulse feature different central wavelengths. If these wavelengths superimpose in the nonlinear crystal, the spectrum of the resulting frequency-mixing signal will deviate from the case of a transform-limited pulse. The relation between the electric field amplitude of the mixing signal and the FROG trace reads

$$I_{\mathrm{FROG}}(\omega,\tau) \propto |E_{\mathrm{Sig}}(\omega,\tau)|^2. \tag{5.22}$$

Both constraints correspond to a subset of potential functions describing the electric field of the pulse. Apart from the time-reversal ambiguity described below, there is theoretically only one solution that complies with both constraints.

As illustrated in Fig. 5.7, the FROG algorithm tries to find the solution iteratively. Starting with an initial guess for the electric field, the algorithm systematically adapts the field in such a way that it successively complies with one of the two constraints. Thereby, the resulting field of each iteration is used as input for the next step. The modifications to be made decrease with every step and the reconstructed field approaches the correct solution E^{final}.

In fact, the electric field of a pulse cannot be reconstructed precisely since FROG traces stem from discrete spectral measurements that are always subjected to experimental errors. Eventually, the algorithm gets stuck in a loop calculating neighboring solutions. The degree of convergence can be assessed via the G-error. It is defined as the root-mean-square

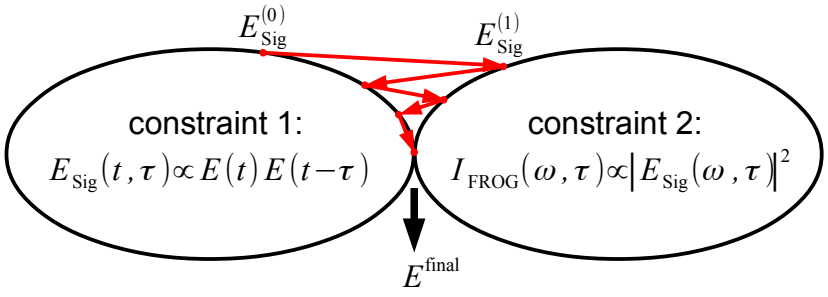

Fig. 5.7: Schematic of the SHG-FROG algorithm: Starting with an initial guess for the electric field, the algorithm consecutively modifies the function to alternatively comply with the two constraints. The final solution corresponds to the intersection of both subsets. (Fig. adapted from [34].)

deviation of the reconstructed FROG trace from the experimental FROG trace I_{FROG} [34]. In this context, both the experimental and the reconstructed trace must be normalized to unity:

$$G = \left[\frac{1}{N^2} \sum_{\omega,\tau=1}^{N} \left[I_{\mathrm{FROG}}(\omega,\tau) - |E_{\mathrm{Sig}}(\omega,\tau)|^2 \right]^2 \right]^{1/2} \tag{5.23}$$

While the fundamental concept of the FROG algorithm is quite intuitive, its concrete implementation is very sophisticated. It must be ensured that the iteration converges reliably and efficiently. With respect to Fig. 5.7, this condition translates into a monotonous decline in the distance of the iterated solution from the intersection of both subsets. A brief summary of the basic concepts of the SHG-algorithm is given in the following; a full description can be found elsewhere [34].

First, the algorithm must be initialized with an electric field $E^{(0)}$ that can be a Gaussian envelope or simply noise. Subsequently, the signal field $E^{(0)}_{\mathrm{Sig}}$ is computed with equation (5.21). Its Fourier transform is modified in order to comply with equation (5.22) and the experimental FROG trace. For this purpose, the spectral amplitude of the signal field is replaced with the square root of the FROG trace while keeping the spectral phase unchanged. Via inverse-Fourier transformation the new field $E^{(1)}_{\mathrm{Sig}}$ is converted into time-domain.

In the next step, the electric field $E^{(2)}$ is determined that describes $E^{(1)}_{\mathrm{Sig}}$ best on the basis of equation (5.21). Mathematically, this step corresponds to the minimization of the Z-error that is defined as the sum of the normalized squared deviations:

$$Z = \sum_{t,\tau=1}^{N} |E_{\mathrm{sig}}(t,\tau) - E(t)E(t-\tau)|^2 \tag{5.24}$$

In practice, it is sufficient to perform a one-dimensional minimization with the direction given by the gradient of Z. The resulting electric field $E^{(2)}$, in turn, serves as input for the first iteration step above, substituting $E^{(0)}$. This iteration cycle is repeated until the desired degree of convergence is achieved.

The data analysis, presented in the next chapter, is based on an implementation of the FROG algorithm in *MATLAB*. The code is freely accessible from the group of R. Trebino [105]. The FROG traces are acquired by a setup that is based on a fiber-coupled spectrometer: After appropriate attenuation, the laser beam to be characterized is split up into two paths. The delay τ is controlled by changing the length of one path with a retroreflector mounted on a motorized stage. Both beams are focused into a nonlinear crystal by spherical mirrors that minimize dispersion. Furthermore, the nonlinear crystal, a 0.5 mm thick BBO crystal, is identical to the one used in the coherent control setup and exhibits the same dispersion. During adjustment, the BBO crystal is exchanged with a

beam profiler that allows to measure the beams' position and size. In this way, it can be ensured that the beams fully overlap in the focus. Otherwise, the measurement may be distorted by spatial dispersion of the laser source [106; 107], i.e. the phase of the pulse changes across the beam width. Here, spatial dispersion would become most influential in the BBO crystal if the two beams barely overlapped.

The BBO crystal emits three frequency-doubled beams. Only the central one is generated by frequency-mixing of both incoming beams and only present if these spatially and temporally overlap. This central beam is focused into a fiber-coupled spectrometer; the other beams are independent on the delay τ and blocked. It should be noted that dispersion by the fiber and the lens in front of the spectrometer does not influence the FROG trace as the spectrometer only records the time-integrated spectral intensity. In contrast, dispersion in front of the BBO may influence the measurement as frequency mixing is implicitly sensitive to a pulse's phase. In fact, this phase sensitivity is the basis of the FROG method.

The FROG trace is a two-dimensional matrix. Each row corresponds to a spectrum of the mixing signal for a fixed delay τ that increases with the row number. To ensure a reliable pulse reconstruction, it is necessary to capture the full nonlinear response of the pulse superposition. Therefore, a spectrometer with a sufficient detection range and resolution is required. Here, a fiber-coupled spectrometer with a 2048 pixel detector is used spanning a wavelength range from 520 nm to 1200 nm. In comparison, the bandwidth of a transform-limited 50 fs second harmonic pulse centered around 750 nm is 17 nm. Apart from that, the travel range of the motorized stage must be chosen such that the two pulses are entirely shifted against each other and no longer overlap at the first and last measurement. If recorded correctly, the spectral response should be centered in the FROG trace and its edges should not contain any signal.

The FROG trace is imported into the *MATLAB* application after it has been modified to match the input format. For example, the code requires the trace to be a square matrix that is a function of frequency instead of wavelength. Additionally, the background noise of the spectrometer is subtracted beforehand to minimize artifacts. Fig. 5.8 depicts the graphical user interface of the *MATLAB* application for an exemplary FROG trace. The experimental FROG trace itself is shown in the upper left corner. The horizontal and vertical axes correspond to the delay τ in units of fs and the frequency in units of 10^{15} Hz, respectively. A logarithmic color scale visualizes the spectral intensity. Proceeding counterclockwise, the interface displays the reconstructed FROG trace, the deviation between those two traces, the G- and Z-error plotted against the iteration step and finally the reconstructed pulse in frequency-domain in units of 10^{15} Hz as well as time-domain in units of fs.

Fig. 5.8 depicts a situation where the iteration has already converged. As can be

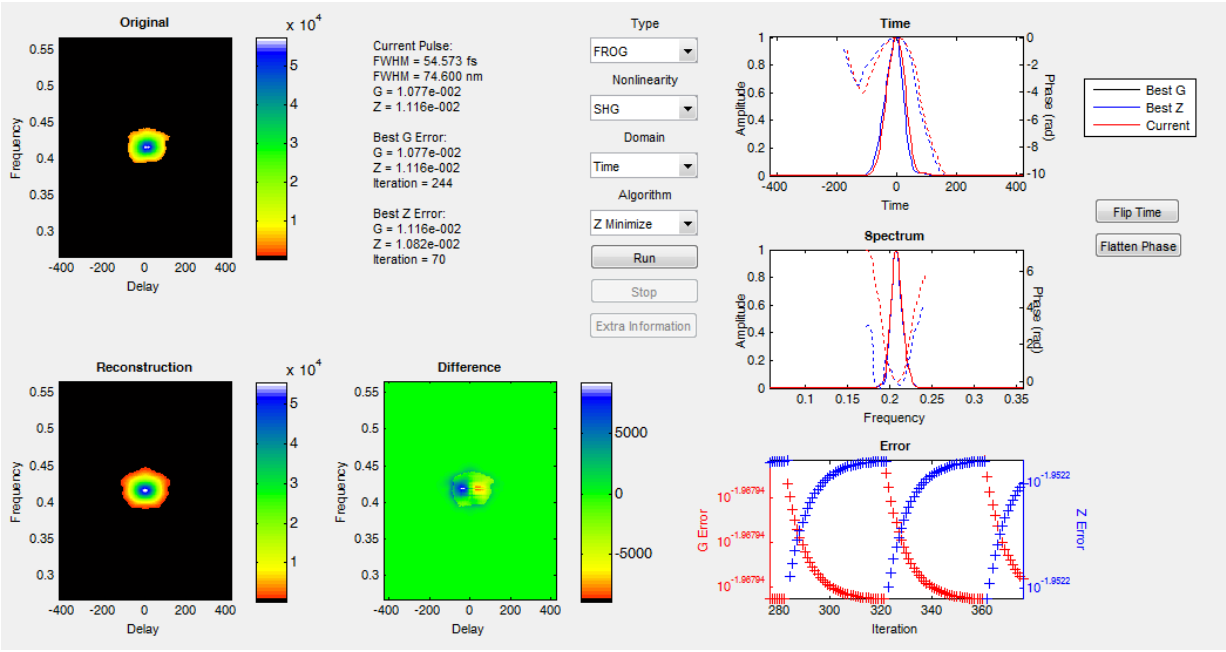

Fig. 5.8: Interface of the freely available *MATLAB* implementation of a FROG algorithm [105]: The input FROG trace is shown in the top left, the reconstructed trace is shown below. Proceeding counter-clockwise the screenshot displays the difference of both traces, the G- and Z-error as a function of the iteration and the amplitude as well as phase of the reconstructed laser pulse in frequency- and time-domain. In this case, the FROG trace stems from the output of the OPA laser system with a positive GVD induced by an SF11 slab. The GVD manifests as phase curvature in the frequency-domain of the pulse reconstruction.

seen from the error, the algorithm is stuck in a loop and the error does not decrease any further. This is why the program was stopped after a few hundred iteration steps which take less than one minute on a modern desktop computer. The resulting Gaussian-like pulse is displayed in phase and amplitude featuring a FWHM of 55 fs. With respect to the frequency-domain, the phase exhibits a strong curvature indicating a significant GVD which is induced by an SF11 slab. However, the actual sign of the GVD cannot be deduced from the FROG trace because of the time-reversal ambiguity of SHG-FROG [34].

As evident from equation (5.21), the mixing signal is a symmetric autocorrelation that manifests in the symmetry of the FROG trace with respect to the time axis. In consequence, it is not possible to deduce the sign of the time axis of the pulse reconstruction. Equivalently, it is not possible to derive the sign of even terms in the Taylor expansion of the phase, like the GVD (cf. equation (5.3)). However, this shortcoming can easily be overcome by performing two measurements. In between, the pulses' GVD is altered by a known value. In practice, this can easily be realized by putting a dispersive material like glass into the beam path. Subsequently, the sign of the time axis can be deduced from the difference of the measurements.

5.3 Experimental Evaluation of the Proposed Method

This chapter focuses on the practical application of the proposed phase-retrieval method. The specific influence of three differently chirped pulse trains on the spectral phase of the current interferogram is exemplarily discussed. Subsequently, the proposed method is compared to SHG-FROG measurements. By introducing different glass slabs into the beam path, the GVD of nominally 45 fs wide pulses with a central wavelength of 1450 nm is varied between about -500 fs^2 and $+1000$ fs^2. The validity of the simplifying assumptions that are made during the derivation are discussed at the end of this chapter.

Exemplary Application

Once set up, the measurement procedure of the proposed method is similar to that of the two-beam interferometer as described in chapter 3.3. By varying the length of one interferometer arm, the injected current is measured as a function of the relative pulse delay τ. An exemplary resulting current interferogram is depicted in Fig. 5.9(a). In this case, the corresponding laser pulses are not altered by an additional glass slab. A constant current offset, caused by the phase-independent current injection term (cf. chapter 5.1) or conventional photocurrents, is subtracted. Special care is taken during alignment of the focal spot on the sample to minimize the influence of additional photocurrents that may occur at the illuminated metal-semiconductor junction.

The current interferogram exhibits a Gaussian-like envelope that resembles the one from the two-beam interferometer. However, the interferogram in Fig. 5.9(a) results from two overlying convolutions of different field combinations. Since both current contributions oscillate with different frequencies with respect to the delay τ, the envelope of the interferogram is modulated by two carrier waves which manifest as beating pattern. Owing to the symmetry of the interferogram, it can be concluded that the pulse pair impinges simultaneously on the sample, as claimed by the theoretical approach in chapter 5.1.

Fig. 5.9(b) depicts the amplitude of the interferogram's Fourier transform. It reveals the two predicted Gaussian-like peaks at the central angular frequencies $\omega_0 \approx 1.3 \cdot 10^{15}$ Hz and $2\omega_0 \approx 2.6 \cdot 10^{15}$ Hz. These correspond to wavelengths of 1450 nm and 725 nm that coincide with the fundamental and second harmonic beam. The similar amplitude of both peaks confirms that the tilted sample geometry allows to measure both current contributions with similar efficiency. Apart from noise, the Fourier transform does not contain any other peaks.

The proposed method relies on the spectral phase of the Fourier transform, that is exemplarily depicted in Fig. 5.10. Black circles mark the spectral phase of the current interferogram in Fig. 5.9(a) that is recorded with unaltered laser pulses. Red triangles facing upwards and blue triangles facing downwards correspond to measurements with laser pulses

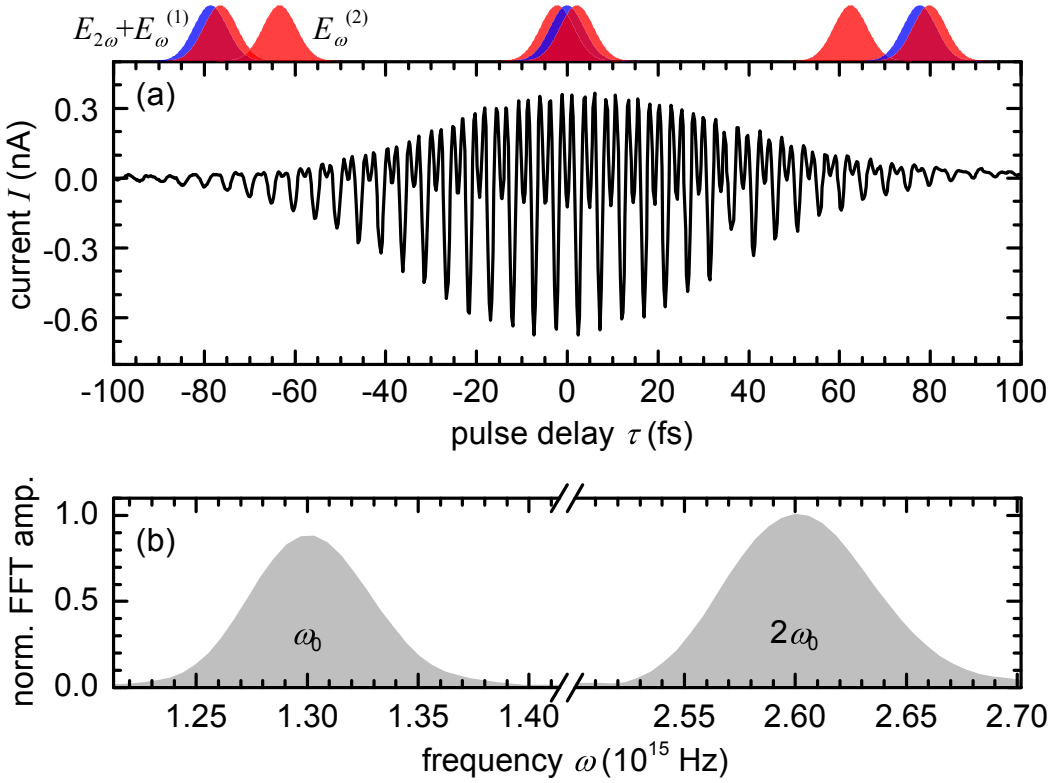

Fig. 5.9: (a) Current interferogram recorded at the three-beam setup with 45 fs-wide fundamental laser pulses at 1.45 µm. The relative timing τ of the two fundamental pulses and the second harmonic pulse is illustrated above the diagram. Different field combinations result in two current contributions that oscillate with a different frequency. A constant current offset is subtracted for analysis. (b) The Fourier amplitude of the current interferogram reveals the central angular frequencies ω_0 and $2\omega_0$ of the two carrier waves.

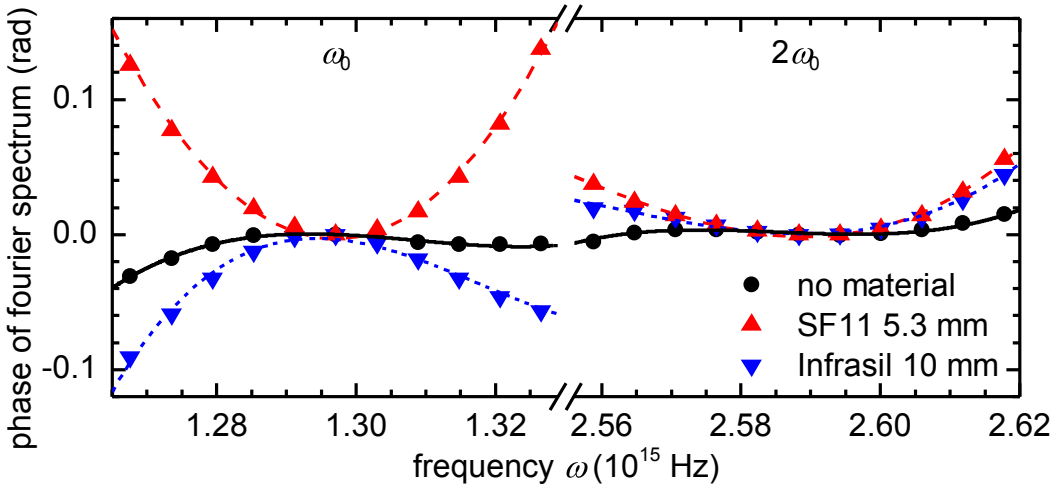

Fig. 5.10: Spectral phases of the current interferograms' Fourier transforms centered around the peaks of the Fourier amplitude at ω_0 and $2\omega_0$ (cf. Fig. 5.9(b)). The introduction of a positive (negative) GVD by pulse propagation through SF11 (Infrasil) significantly influences the spectral phase. The curves correspond to polynomial fits.

that propagate through an additional slab of 5.3 mm SF11 or 10 mm Infrasil, respectively, inducing a positive or negative GVD. The depicted frequency range corresponds to the inner part of both peaks in Fig. 5.9(b). If the signal-to-noise ratio is too low as in the outer parts of the peaks, the spectral phase is not well-resolved. An offset that is constant or linear in the frequency is subtracted from all data points. This offset merely corresponds to a shift of the whole current interferogram on the time axis and does not alter the pulse shape.

Prior to calculating the Fourier transform, the current interferograms are padded with zeros on one side of the time axis. While these do not add any information, the reduced step size of the Fourier transform prevents the FFT algorithm from introducing arbitrary phase jumps of 2π. Although the resulting spectral phases are equivalent, phase jumps would complicate the further analysis. It should be noted that alternatively the measurement range of the current interferogram could be extended. However, as the pulses would not overlap at such delay times there would not be any signal, either. Therefore, the additional zeros do not add any false information.

Introducing a material into the beam path significantly influences the spectral phase centered around ω_0. While the spectral phase of the measurement with unaltered laser pulses corresponds to an almost flat curve, the other two curves exhibit a significant curvature with opposite signs. With a calculated GVD modification of $+330$ fs^2 for the SF11 slab and -160 fs^2 for the Infrasil slab, the opposite curvature of the according curves is in line with the theoretical prediction. Recalling the simplified equation (5.17), the curvature D_{ω_0} of the spectral phase is predicted to be proportional to the GVD of the laser pulses: $\phi''_{\omega_0} = 9/8 \cdot D_{\omega_0}$. Based on this equation, it can already be deduced from Fig. 5.10 that the unaltered laser pulses are almost transform-limited.

In contrast, the spectral phase at $2\omega_0$ changes little by the introduction of additional slabs. The phase is generally relatively flat, compared to the phase at ω_0. If the assumption $\phi''_{2\omega_0} = 1/2 \cdot \phi''_{\omega_0}$ for thin nonlinear crystals holds [102], a flat phase agrees with the theoretical prediction of equation (5.13): $D_{2\omega_0} = 1/2 \cdot \phi''_{\omega_0} - \phi''_{2\omega_0}$. The slight deviation from a straight flat phase may result from residual dispersion differences in the interferometer, e.g. the silicon filter, or it may indicate that the assumption above is not fully fulfilled for a 0.5 mm thick BBO crystal. However, both shortcomings could easily be overcome. Owing to the high conversion efficiency of BBO and the high absorption of silicon with respect to the second harmonic beam, much thinner pieces would be sufficient. In fact, the BBO crystal in the above mentioned setup is shifted out of focus to lower the intensity and prevent generation of a white-light continuum. The components used in the setup are partly chosen based on availability.

To account for the phase deviations at $2\omega_0$, the following calculation of the GVD of the

fundamental beam employs equation (5.15) which is not further simplified:

$$\phi''_{\omega_0} = \frac{9}{8} D_{\omega_0} - \frac{1}{2} D_{2\omega_0} \tag{5.25}$$

Nevertheless, it should be emphasized that the deviations from the flat phase are generally relatively small. Taking into account that the GVD depends much less on the curvature at $2\omega_0$ than at ω_0, the approximation $D_{2\omega_0} \approx 0$ can be considered as justified. As a direct consequence, the derivation of the GVD does not require the corresponding current component to be measured at all. However, in practice, the spectral phase at $2\omega_0$ can be regarded as a useful indicator for the validity of the measurement.

In order to evaluate the measurements quantitatively, third-order polynomial functions that are centered around ω_0 or $2\omega_0$ are fitted to the spectral phase. The corresponding curves are depicted in Fig. 5.10. Evidently, these are dominated by the quadratic terms $1/2 \cdot D_{\omega_0} \cdot (\omega - \omega_0)^2$ as well as $1/2 \cdot D_{2\omega_0} \cdot (\omega - 2\omega_0)^2$ and agree very well with the data points. As predicted, the influence of the introduced material on the cubic components of the phase is small compared to the quadratic component. For this reason, the following discussion focuses on the derived GVD. At the same time, these findings corroborate that the GVD is sufficient to describe propagation of Gaussian-like pulses with a duration of about 50 fs through typical experimental setups.

Comparison with SHG-FROG

For a sophisticated evaluation, the proposed method is applied to laser pulses with different chirp induced by additional glass slabs. The curvatures of the interferograms' spectral phases are derived as explained above and inserted into equation (5.25) to calculate the GVD. For comparison, the laser pulses are also characterized by the SHG-FROG setup. To minimize influence of laser instabilities or alignment of the glass slab, both methods are subsequently applied without changing the glass slab in between. Reference measurements with unaltered pulses at the beginning and at the end of each measurement series ensure that there is no long-term drift of the laser which may disturb the measurement.

The FROG measurements are processed as described in chapter 5.2. The GVD is derived by fitting a polynomial function to the spectral phase of the reconstructed laser pulse (cf. Fig. 5.8). The sign of the GVD cannot be deduced from one FROG measurement alone. However, it can be determined from the comparison of two measurements if the GVD is changed by a known value, in this case with glass slabs.

Fig. 5.11 depicts the results of both phase-retrieval methods. The derived GVD is plotted against the expected GVD change. The latter is calculated from the thickness of the inserted glass slabs on the basis of the Sellmeier equation (5.20). Negative values correspond to an additional pulse propagation through Infrasil; positive values correspond

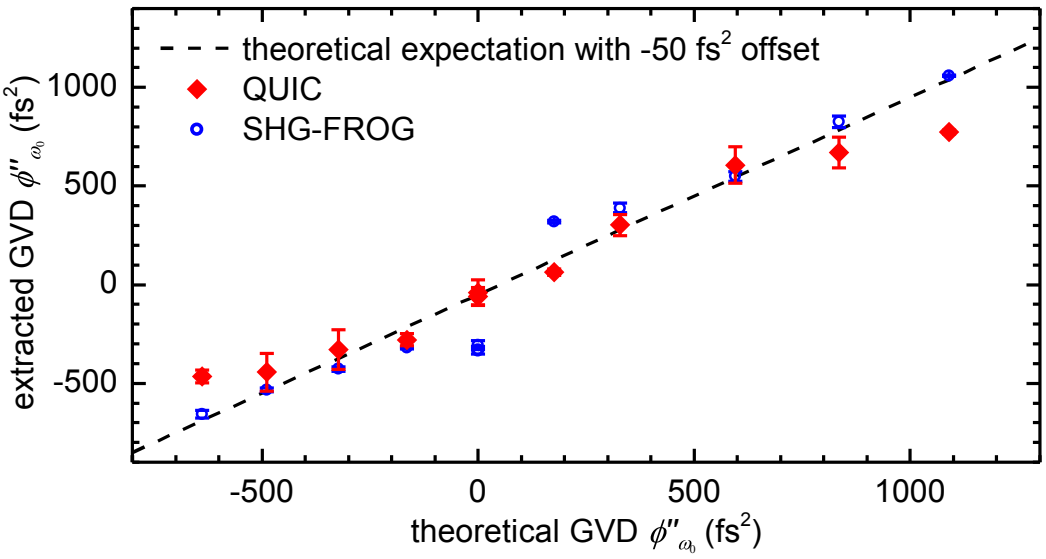

Fig. 5.11: Quantitative comparison of the GVD retrieval via SHG-FROG and the proposed method based on QUIC. Measurements are performed at the OPA laser system with nominally 45 fs-wide laser pulses at a central wavelength of 1.45 µm. The determined GVD is plotted against the theoretically expected GVD introduced by glass slabs and calculated by their Sellmeier coefficients. Error bars correspond to the standard deviation of three measurements. The linear theoretical expectation is corrected by an empirical offset of -50 fs^2 that corresponds to the residual GVD of the laser output.

to measurements with SF11 slabs. The data points are based on three consecutive measurement series that are carried out to assess the variance of both methods. Red diamonds mark the average GVD that is derived from the three individual current interferograms via the proposed method. Error bars quantify the respective standard deviations. The corresponding FROG data are indicated by blue circles. A straight line represents the theoretical expectation for the experimental GVD. Since the GVD of the unaltered laser pulses is unknown a priori, an empirical offset of -50 fs^2 is added that is based on the experimental data points from the FROG measurements.

The reference FROG measurements exhibit a low scatter and follow the linear theoretical expectation. Significant deviations only occur for low absolute values of the GVD. Such deviations may result from the specific setup or the SHG-FROG algorithm. On the one hand, the FROG trace may be distorted by phase-mismatch that increases with the thickness of the employed nonlinear crystal [34]. As stated above, the 0.5 mm thick BBO crystal is chosen on the basis of availability and could be exchanged with a thinner one. On the other hand, the SHG-FROG algorithm itself has difficulties to reconstruct pulses with a flat phase [34]. Nevertheless, the FROG measurements allow to derive the GVD of the unaltered laser pulses which is required to determine the above mentioned offset of the theoretical expectation.

In general, the results of the proposed phase-retrieval method agree well with the FROG data and the theoretical expectation. Particularly, the determination of low absolute values of the GVD including their sign proves the validity and accuracy of the proposed method. On the contrary, the highest values tend to be underestimated. Such a flattening is expected from the employed simplified equation (5.25) and is addressed in more detail below. The variance of the data points is higher than for the corresponding FROG measurements. However, it must be mentioned that the specific QUIC setup exhibits much longer path lengths and is consequently more susceptible to misalignment of the input beam.

Although special care is taken, a slight misalignment of the slabs or deviation from plane parallelism of the glass surfaces may amount to a substantial misalignment in the setup. In fact, there are also measurements with glass slabs of up to 60 mm length corresponding to higher GVD values that are excluded from Fig. 5.11 because of the high scatter. Such an influence of misalignment could be reduced by shortening the path lengths of the setup. In general, it should be emphasized that the specific setup represents a first prototype for the proposed method. Taking this into account, the measurements agree quite well.

Theoretical Limitations of the Proposed Method

The aforementioned underestimation of a high GVD results from the simplifications of equation (5.25). The latter is an approximation of the more complex equations (5.12) and (5.13) which is only valid if the condition $|\phi''_{\omega_0}|, |\phi''_{2\omega_0}| \ll t^2_{\mathrm{p}_0,\omega}, t^2_{\mathrm{p}_0,2\omega}$ is fulfilled. Both relations are exemplarily depicted in Fig. 5.12. The calculated phase curvature D_{ω_0} at ω_0 is plotted against the GVD ϕ''_{ω_0} that serves as variable in this case. To simplify the illustration, $\phi''_{2\omega_0} = \phi''_{\omega_0}/2$ is assumed. The three exemplary curves are calculated for pulse durations $t_{\mathrm{p}_0,\omega} = \sqrt{2} \cdot t_{\mathrm{p}_0,2\omega}$ of 30 fs, 45 fs and the limit $t_{\mathrm{p}_0,\omega} \to \infty$. In practice, the pulse duration can be derived from the spectral width of the pulse utilizing the time-bandwith product. For example, the OPA features a Gaussian spectrum that is centered around 1.45 µm with a FWHM of 70 nm. The resulting pulse duration $t_{\mathrm{p}_0,\omega}$ calculates to 45 fs and thus corresponds to the middle curve in Fig. 5.12.

The calculated curvature D_{ω_0} scales approximately linearly with the GVD ϕ''_{ω_0} if its absolute values are not too high. At higher values, the curves in Fig. 5.12 begin to flatten. The longer the pulse length $t_{\mathrm{p}_0,\omega}$ is, the more shifts the onset point to higher GVD values. Ultimately, the relation becomes completely linear in the limit $t_{\mathrm{p}_0,\omega} \to \infty$. It corresponds to the simplified linear equation (5.17): $\phi''_{\omega_0} = 9/8 \cdot D_{\omega_0}$. The curve for $t_{\mathrm{p}_0,\omega} = 45$ fs begins to significantly flatten for absolute GVD values exceeding 500 fs^2. As a result, high GVD values are underestimated if they are derived from the phase curvature via the simplified linear equation. Indeed, Fig. 5.11 exhibits such a behavior. While absolute values below 500 fs^2 agree well with the theoretical expectation, higher values are systematically

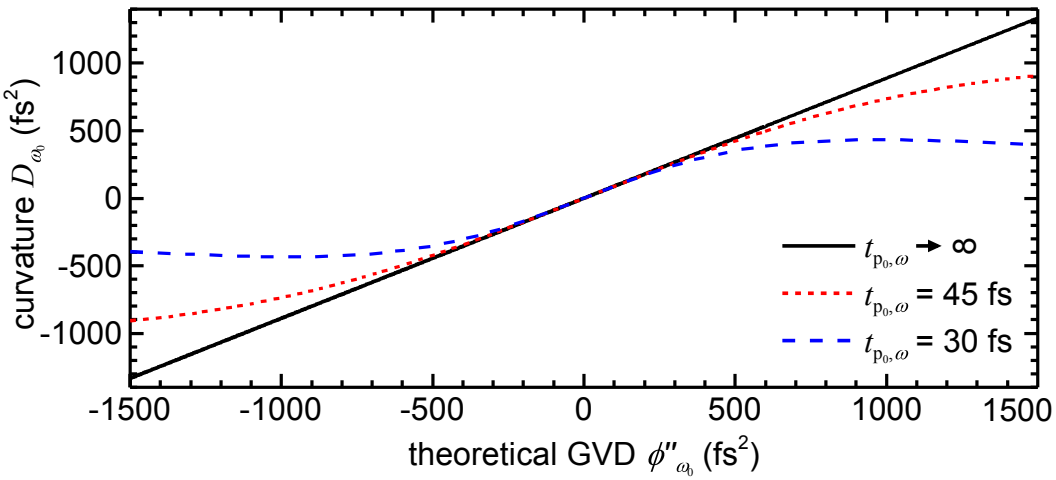

Fig. 5.12: Numerical calculation of the phase curvature of the Fourier transform at ω_0 as a function of the GVD of the fundamental laser pulse. With respect to the second harmonic pulse, $\phi''_{2\omega_0} = 1/2 \cdot \phi''_{\omega_0}$ as well as $t_{p_0,2\omega} = 1/\sqrt{2} \cdot t_{p_0,\omega}$ is assumed. The curvature is calculated for two explicit fundamental pulse durations and the limit $t_{p_0,\omega} \rightarrow \infty$. The latter corresponds to the linear relation $D_{\omega_0} = 8/9 \cdot \phi''_{\omega_0}$.

underestimated.

If the GVD is derived via equation (5.13), the underestimation of high values can be corrected. In this way, the accuracy of the proposed method can be extended to a broader range of GVD values. However, there is still an upper limit. As evident from the curve for $t_{p_0,\omega} = 30$ fs^2 in Fig. 5.12, the curvature eventually passes through a maximum and declines. In this case, the derived GVD is very sensitive to small changes of the curvature and there is an ambiguous relation between both.

To conclude, the practical relevance of the theoretical limitations is discussed. A difference of ± 500 fs^2, at which the linear approximation begins to break down, amounts to a propagation through 31 mm Infrasil in the above mentioned setup. Such quartz glasses or borosilicate glasses, e.g. BK-7 by *SCHOTT*, with comparable GVD are typically used for optical components like lenses [29, p. A152]. For comparison, the lenses that are used in the experiments presented here exhibit a thickness of a few millimeters. Furthermore, it is instructive to calculate the induced pulse broadening. According to equation (5.4), a GVD of 500 fs^2 broadens a 45 fs pulse by 20%. In conclusion, even the linear equation (5.25) is suitable for typical experimental setups, employing Gaussian-like pulses.

5.4 Conclusion and Outlook

A novel phase-retrieval method for ultrashort laser pulses is theoretically proposed as well as experimentally demonstrated. It is based on QUIC in LT-GaAs by a superposition of the beam to be characterized and its second harmonic. In essence, the GVD of the pulses

can be directly retrieved from the Fourier transform of a single current interferogram.

The phase-retrieval method is applied to nominally 45 fs long pulses with a central wavelength of 1.45 µm. In order to benchmark this technique, it is compared with an SHG-FROG setup. By introducing different glass slabs into the beam path, the chirp of the pulses is systematically altered. Although the underlying theory is based on some simplifications and the setup is only a prototype, the proposed method proves quite accurate with respect to typical experimental scenarios. Especially small absolute GVD values and the change of the GVD sign can be precisely derived.

Such sensitivity can be explained by the explicit phase dependence of the method. In contrast to other methods, such as SHG-FROG, the underlying QUIC process explicitly depends on the optical phase. Amplitude and direction of the injected currents are directly influenced by the relative phase of the fundamental and second harmonic beam. In comparison, SHG-FROG is based on an iterative algorithm that extracts the phase from implicitly phase dependent spectra of a mixing signal.

The prototype setup could be further improved by shrinking the setup size or optimizing the choice of components. For example, such a long high precision stage as in the prototype setup is not necessary; a much cheaper piezo stage with a travel range of a few tens of micrometers corresponding to the pulse duration should be sufficient. Choosing appropriate semiconductors for current injection with another band gap than GaAs [108], could extend the method to other optical wavelengths ranges.

In principal, the method should also be applicable to other pulse durations. QUIC has been demonstrated for laser pulses with a duration of up to 175 fs [8], though the influence of the spectral phase on such long pulses is much less pronounced. In the opposite regime, the method should benefit from the fact that the spectral width of a pulse scales inversely with its duration.

Chapter 6

Optical Current Detection via QUIC

Current measurements typically rely on the detection of a voltage drop across a resistor. Alternative measurement schemes are based on the detection of the surrounding magnetic field, for example with a Hall sensor or via induction [37; 38]. Utilizing the Faraday effect – a magnetically induced rotation of the light polarization – a current's magnetic field can also be detected optically. Similar to the aforementioned methods, the latter method requires an external probe, in this case a fiber coil, which limits the spatial resolution to macroscopic scales [37; 38; 109].

An optical measurement scheme which is based on direct interaction between a current and a light wave would allow to detect currents on arbitrary microscopic spots via tightly focused laser beams. Furthermore, all-optical methods are not limited by electronic RC constants and enable ultrafast time-resolved measurements by using femtosecond laser pulses. However, such an optical current detection is non-trivial as it requires a sensitivity to the anisotropy of the carrier distribution. Linear transmission measurements are only sensitive to the total density of excited carriers since one-photon absorption is symmetric with respect to the crystal momentum (cf. chapter 2.2).

The crystal momentum of occupied electronic states can be detected indirectly by angle-resolved photoemission spectroscopy, i.e. angle-resolved velocity measurements of photoemitted electrons [110]. Femtosecond time-resolved two-photon photoemission, a subtype, is based on an optical excitation of electrons via ultrashort laser pulses [111]. For example, such techniques have previously been utilized for time-resolved measurements of coherently controlled surface currents in copper [18]. The drawbacks of angle-resolved photoemission methods are their sophisticated detection schemes which require electron optics and vacuum conditions for electron propagation.

An optical current measurement technique which is based on the analysis of transmitted or reflected laser beams would simplify the detection scheme. However, for the reason mentioned above, such a method may not rely on linear transmission or reflection alone. Recently, current-induced second harmonic generation in GaAs has been demonstrated for

current detection [112; 113].

There is a theoretical proposal by Liu *et al.* for current detection utilizing QUIC [35; 36]. This proposal is based on the fact that both the carrier distribution of the current as well as the induced transition rates of QUIC are asymmetric with respect to the crystal momentum. Depending on whether both exhibit the same or opposite asymmetry, the transmission of the input beams is expected to be either more or less increased by state blocking. By controlling the asymmetry of the transition rates via the relative phase of the pulse pair, QUIC could be utilized to probe an anisotropic charge distribution via transmission measurements. In turn, this technique would allow to investigate ultrafast current dynamics by all-optical means.

In the following, the proposal for electrical current detection via QUIC is experimentally investigated and discussed with respect to its practicability. After a brief explanation of the theoretical proposal in chapter 6.1, an experimental implementation is presented in chapter 6.2. Measurements which are performed with this implementation are discussed in chapter 6.3.

Parts of this chapter are in preparation for publication elsewhere [46].

6.1 Theoretical Proposal

Current detection via QUIC relies on the interaction of the current's asymmetric carrier distribution with the optically induced transitions. The present chapter illustrates the underlying theoretical concept of the proposal by Liu *et al.* [35; 36]. Within this context, the fundamentally differing mechanisms of current generation via a static electric field on the one side and via QUIC on the other side are discussed.

The application of a static voltage to a semiconductor results in a current flow which is mediated by free carriers, i.e. electrons in the conduction band or holes in the valence bands. Strictly speaking, an ideal semiconductor at $T = 0\,\mathrm{K}$ is insulating by definition since all bands are either entirely filled or empty. However, in realistic scenarios there is always a finite number of thermally excited carriers. Additionally, the density of free carriers can be enhanced permanently by doping or temporarily by optical excitation as in the setup described in chapter 6.2.

With respect to the carriers' energy dispersion $E(\mathbf{k})$, the application of an external electric field $\mathbf{E}$ results in a shift of the carriers' crystal momentum $\mathbf{k}$ [87, ch. 8.2]:

$$\frac{\mathrm{d}\mathbf{k}}{\mathrm{d}t} = -e\mathbf{E} \tag{6.1}$$

Without scattering, an external field would cause a monotonic increase of the crystal

momentum. Carrier scattering limits the average **k**-shift to a constant value which is linear in the current relaxation time τ_r. The resulting asymmetry of the carrier distribution corresponds to a directed charge current.

Fig. 6.1(a) illustrates the voltage-induced **k**-shift of a thermally or optically excited carrier distribution in the conduction and valence band. For simplicity, the displayed crystal momentum k is restricted to one dimension and only two bands are shown. Both the electron and hole distribution are shifted in the same direction. The behavior of the hole distribution can also be interpreted as a positive k-shift of an electron distribution with respect to the energy minimum of the valence band. Owing to the opposite slope of both bands, electrons and holes move into opposite directions and their current contributions add up. It should be mentioned that the displayed k-shift is exaggerated for clarity. Typically, the asymmetry of a voltage-induced current is relatively low and only a small number of carriers which are not compensated by carriers with opposite velocities contribute to the current.

The average **k**-shift of the electron distribution typically exceeds the shift of the hole distribution as the relaxation times differ. The relaxation time τ_r and in turn the distribu-

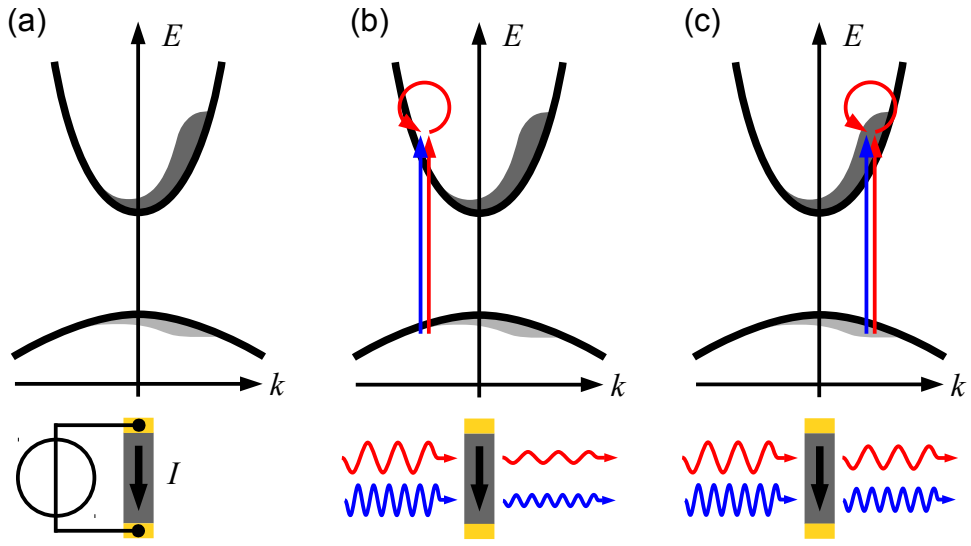

Fig. 6.1: Illustration of optical current detection in a direct band gap semiconductor utilizing QUIC. The upper panels depict simplified band diagrams; differently shaded areas mark the electron and hole distribution. The lower panels represent side views of the sample. (a) The generation of a current via application of an external voltage corresponds to a **k**-shift of the electron and hole distribution. (b) The coherent superposition of a fundamental beam and its second harmonic induces transitions whose addressed crystal momentum **k** can be controlled by the relative phase of the beams. If the transitions at $+k$ are suppressed, the absorption of the beams is hardly influenced by the carrier distribution of the current. (c) If the transitions are excited at $+k$, the absorption is reduced since the addressed states are already occupied by the carrier distribution of the current.

tions' asymmetry can be approximated on the basis of the carriers' mobility $\mu = e\,\tau_\mathrm{r}/m_\mathrm{e}^*$, which is 8800 $\mathrm{cm}^2/\mathrm{Vs}$ for electrons and 400 $\mathrm{cm}^2/\mathrm{Vs}$ for holes in room-temperature GaAs [87, ch. 8.3]. With an effective mass of $m_\mathrm{e}^* = 0.067 \cdot m_\mathrm{e}$ for electrons and $m_\mathrm{h}^* = 0.5 \cdot m_\mathrm{e}$ for heavy holes, the calculation yields relaxation times of about 300 fs for electrons and 100 fs for holes. Because of their lower density of states, the contribution of light holes is neglected.

In contrast to voltage-induced current generation, QUIC is an all-optical process. As described in chapter 2.2, the coherent absorption of a fundamental beam and its second harmonic causes interfering one-photon and two-photon transitions at crystal momenta with opposite sign. The absolute value of the crystal momentum is determined by the photon energy. Controlled by the relative phase and the polarization of the beams, carriers are predominantly excited at $+k$ or $-k$. The resulting asymmetric electron and hole distributions correspond to directed electron and hole currents which add up. In contrast to voltage-induced current generation, the asymmetry of the distributions is much more pronounced and a majority of the excited carriers may contribute to the current.

If both current generation processes are combined, the voltage-induced current may influence the optical transitions. Fig. 6.1(b) as well as (c) show situations in which a fundamental beam and its second harmonic are perpendicularly focused onto a thin GaAs sample. Simultaneously, an external voltage induces a current in the sample. The external voltage causes a positive k-shift of the previously excited carrier distribution. The excitation could be either induced thermally or optically by an additional pump beam which must not be confused with the two beams for QUIC. Via appropriate polarization adjustment of the latter beams, the current is injected parallel to the voltage-induced current. Governed by the optical phase, the corresponding transitions are predominantly induced at $-k$, as in Fig. 6.1(b), or at $+k$, as in (c).

Depending on whether the optical transitions at $+k$ or $-k$ dominate, the transmission of the beams is expected to be either more or less influenced by current-induced state blocking. In the latter case, as depicted in Fig. 6.1(b), optical transitions are induced between mostly unoccupied electronic states. The absorption of the beams is hardly influenced by the current's carrier distributions which are centered at $k > 0$. However, if the optically addressed states are predominantly located at $+k$, as depicted in Fig. 6.1(c), they are significantly influenced by the current. Owing to the occupation of electron and hole states at $+k$ by the current, there are less states available for optical excitation. As a consequence, the absorption of the beams is reduced. In practice, this effect should be more pronounced for the second harmonic beam as one-photon transition rates are typically higher than two-photon transitions rates of the corresponding fundamental beam.

By analyzing the transmission of the beams as a function of their relative phase, QUIC allows to probe the current direction optically. Since the in-plane angle of the coherently

injected current can be controlled by the beams' polarization, it should also be possible to derive an angle-resolved current map. In comparison, one- or two-photon absorption alone is only sensitive to the density of free carriers. As the induced transitions are symmetric with respect to the crystal momentum $\mathbf{k}$, only the average occupation in the bands is probed. The average occupation, however, does not change by application of an external voltage.

QUIC only accounts for a small portion of the beams' interaction with the semiconductor. In practice, the individual one- and two-photon absorption of the beams significantly exceed the current-induced absorption saturation. However, the proposed current detection technique benefits from the explicit phase dependence of QUIC. By measuring the differential transmission with respect to the optical phase, the contribution of phase-independent one- and two-photon absorption cancels out and the current-induced transmission change remains. Therefore, Liu *et al.* predict a high sensitivity of this technique [35; 36].

With respect to a quantitative analysis, it must be taken into account that the transmission signal represents an integrated response. It contains both the asymmetric electron and hole distribution and depends on the input pulses which determine the optically addressed states. If excess carriers are provided by n-doping, as in the proposal by Liu *et al.*, the hole distribution can be neglected. In this case, the transmission signal only reflects the electron current. The experimental implementation which is presented in the following chapter relies on optical carrier generation. Therefore, it resembles the situation depicted in Fig. 6.1.

6.2 Experimental Implementation

The optical current detection technique is exemplarily applied to a GaAs sample in which a current is induced via application of an external voltage. Since the optical detection relies on QUIC, the experimental implementation partly resembles the prototypical QUIC setup presented in chapter 3.2. In essence, a pulse train of coherent two-color laser pulse pairs, manipulated by an interferometer, is focused on the current in the GaAs sample. The beam transmission through the sample is expected to be influenced by the current and is measured as a function of the relative optical phase. More specifically, the transmission signal should oscillate with respect to the relative delay τ between the pulse pair components, similar to the oscillation in the current interferogram shown in Fig. 3.3. Such a transmission measurement sets special requirements on the setup and particularly on the sample. This requirements are addressed in more detail below.

Experimental Setup

Fig. 6.2 depicts the experimental implementation of the current detection technique that is developed as part of this thesis. The FFS fiber laser is used as a light source. On the one side, it features a stable output with respect to beam intensity and alignment. On the other side, it features a second synchronized beam output that is able to generate an additional second harmonic pump beam for current generation, as is explained further below. Both outputs emit about 100 fs-wide pulses with a central wavelength of 1550 nm.

One output beam is frequency-doubled in a nonlinear crystal to provide a train of two-color pulse pairs for QUIC. Via a subsequent interferometer, both components can be manipulated with respect to their individual intensity, polarization and relative delay τ. In particular, a half-wave plate in one arm is used to achieve a parallel horizontal polarization of both harmonics. Furthermore, the interferometer allows to ensure a collinear propagation

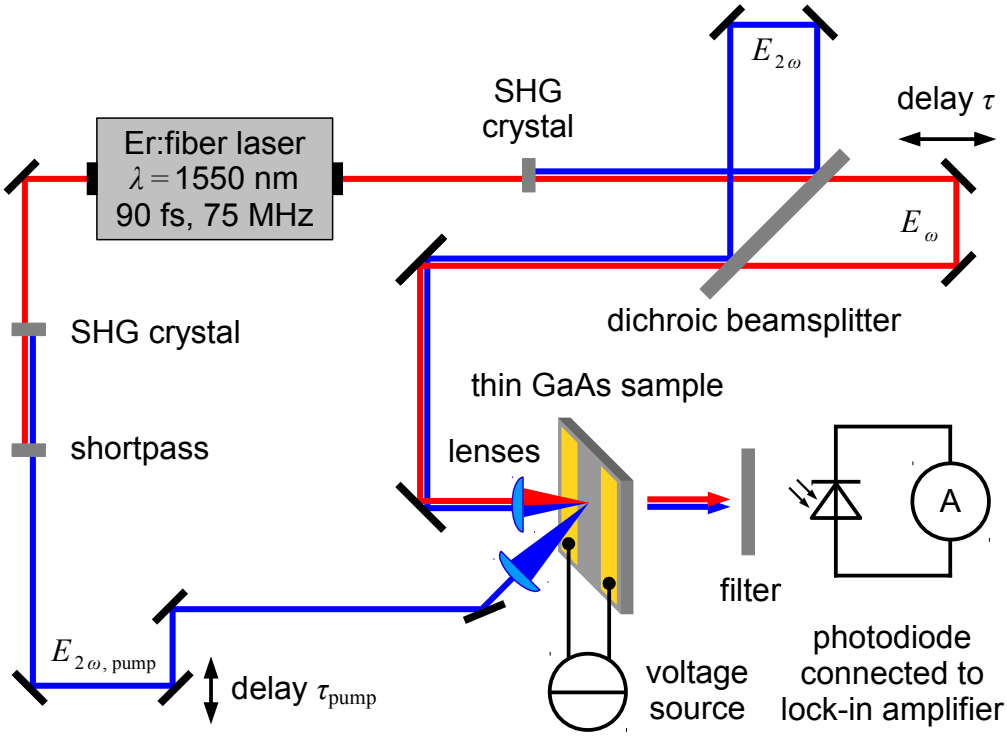

Fig. 6.2: Experimental scheme for current detection utilizing QUIC: One output beam of the fiber laser source is frequency-doubled in a nonlinear crystal and steered into a two-color interferometer which allows to control the probe beams' individual delay τ, their polarization and intensity (optics not shown). Both beams are collinearly focused on the ≈ 10 µm wide gap of two metal contacts on top of a thin GaAs sample. The second synchronized laser output is also frequency-doubled to provide an additional second harmonic pump beam. It is focused on the same spot as the other beams to generate a spatial confined distribution of free carriers which is accelerated by an external voltage. The intensity of the transmitted probe beams is recorded with a photodiode. A filter in front of the photodiode allows to select a specific beam.

of both beams before these are perpendicularly focused on a GaAs sample. To reduce back reflections that may distort the laser source, the sample is slightly tilted.

Basically, the sample consists of a thin layer of GaAs with vertical gold stripes on top. The pulse pairs are collinearly focused on the gap of two parallel metallic contacts. The focal spot diameters are approximately 20 µm for the fundamental beam and 30 µm × 20 µm for the second harmonic component. Simultaneously, an external voltage supply induces a horizontal current between the contacts. Because of the horizontal polarization of the beams, both the pulse pairs and the voltage-induced current address the same crystal momenta. To measure the current's influence on the beam transmission, the sample thickness has to be in the order of the absorption length or less. In the case of GaAs and a second harmonic wavelength of 775 nm, the absorption length amounts to 670 nm [9, and references within]. The absorption length of the fundamental beam is significantly higher since its photon energy is below the band gap. A detailed description of the preparation and characterization of the employed GaAs sample is given below.

To enhance the amplitude of the voltage-induced current, the conductivity of the intrinsic GaAs layer is locally increased by optical excitation. For that purpose, the second synchronized laser output is also frequency-doubled in a nonlinear crystal, resulting in a second harmonic beam power in the order of 20 mW. A shortpass filter blocks the fundamental beam. The additional second harmonic pump beam allows to directly excite carriers in GaAs from a valence to the conduction band. It is focused on the same spot between the metal contacts as the pulse pairs. The minimum focal spot diameter of the pump beam is about 20 µm. A different angle of incidence minimizes disturbance of the pulse pair transmission measurement. The delay τ_{pump} of the pump beam with respect to the pulse pairs is controlled with a motorized stage.

The transmitted pulse pairs are collected with a lens behind the sample and focused on a photodiode. An additional shortpass or longpass filter allows to select a specific beam. The induced photocurrent is proportional to the irradiance and recorded with a lock-in amplifier. The amplifier is either referenced to a chopper in a beam path or to a square-wave voltage which is applied to the sample to induce a modulated current. The latter is generated by a waveform generator which is connected to the contact pair. Alternatively, a constant-voltage source is used which is simultaneously able to precisely measure the induced current. In conclusion, the measurement setup allows to analyze the individual beam transmission and the induced current as a function of various variables, such as irradiance, optical phase or current amplitude.

Sample Fabrication and Characterization

The employed sample is based on a polished GaAs wafer with locally etched windows. These windows have a thickness in the order of the absorption length of the second harmonic beam and allow for measurements of the pulse pair transmission. The lateral dimensions of the windows are 200 µm × 300 µm. Metallic contact pairs on top of the windows are used to apply a voltage and induce a current. It should be noted that the sample does not have to be made from LT-GaAs since the current detection technique is based on a measurement of the beam transmission instead of a measurement of the injected current.

Most parts of the sample preparation steps were performed in the group of Technische Physik 1 at the Friedrich-Alexander-Universität Erlangen-Nürnberg. First, a 380 µm thick substrate of (100) oriented GaAs was overgrown with a thin layer of AlAs and a GaAs layer with a thickness in the order of 1 µm. Afterwards, the substrate was locally removed from the back side via selective etching of predefined areas. The AlAs layer acted as etch stop and prevented the removal of the upper GaAs layer. Gold contacts on top of the windows were defined via optical lithography and metallic evaporation. To enhance mechanical stability, the sample was glued on a transparent glass substrate which in turn was glued into a sample holder with macroscopic electrical contacts. Later, the metallic contacts were connected to the sample holder via tungsten wires and conductive adhesive.

Fig. 6.3 shows a top view of an exemplary section of the sample. The windows appear as shaded areas because of their different thickness. The depicted metallic contact pair which

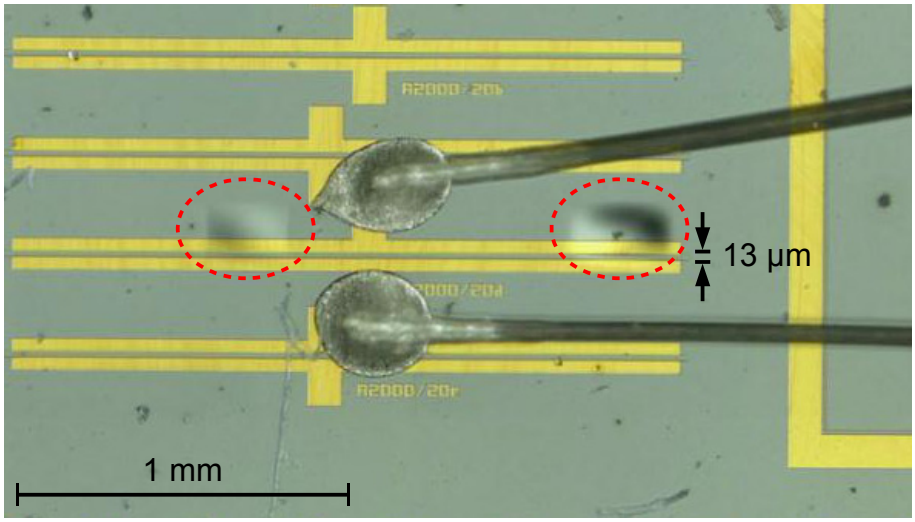

Fig. 6.3: Exemplary top view of the GaAs sample used for transmission measurements. Windows were etched from the back side and appear as shaded areas with dimensions of 200 µm × 300 µm (encircled for clarity). The metallic contact pairs on top of the windows exhibit a gap width of about 13 µm. An external voltage can be applied via tungsten wires which are glued to the contacts. Only contact pairs that lay on top of a window are used in the experiments.

lies on top of the windows has a gap size of about 13 µm. Both contacts are connected to the sample holder with separate wires. The sample also features other windows with metallic contact pairs on top that have a gap width of up to 200 µm.

To characterize the contact pairs with respect to the induction of an electric field in the GaAs window underneath, the Franz-Keldysh effect is employed [47, ch. 3.3.5; 114–116]. This effect can be thought of as a reduction of the effective band gap by application of an electric field. The reduction of the band gap is accompanied by an energetic shift of the density of states. As a result, the absorption of a beam increases if its energy is slightly below the unperturbed band gap. By contrast, the absorption of a beam with an energy slightly above the band gap is reduced. Therefore, the electric field amplitude in the windows can be compared on the basis of voltage-dependent transmission measurements.

Measurements of the Franz-Keldysh effect are performed with a titanium-sapphire laser. Its output spectrum is tuned to ≈ 870 nm to match the band gap of GaAs. Utilizing a narrow bandpass filter, a specific spectral component of the laser output can be selected whose central wavelength is shifted by -10 nm or $+10$ nm with respect to the band gap. A weak portion of the selected spectral component is focused on the gap of a contact pair with a GaAs window underneath. The contact pair is connected to a waveform generator that provides a square-wave voltage alternating between 0 V and up to $+10$ V or -10 V. The voltage-dependent transmission of the windows is recorded with a photodiode and a lock-in amplifier. The latter is referenced to the frequency of the square-wave voltage. This measurement technique suppresses voltage-independent transmission components and ensures a high sensitivity.

While a quantitative analysis of the Franz-Keldysh effect is quite extensive, the transmission measurements allow to qualitatively compare different contact pairs. The strongest responses are recorded at the windows depicted in Fig. 6.3. These exhibit a transmission change of up to 0.15 % at a voltage amplitude of $+10$ V or -10 V. As expected, the sign of the differential transmission changes if the wavelength is shifted across the band gap. These findings are comparable with studies of the Franz-Keldysh effect in similar structures consisting of an LT-GaAs layer and a contact pair with a gap width of 25 µm [117].

By contrast, the response of the other windows is weaker by at least a factor of 2. Partially, the differential transmission signals of the other contacts exhibit a pronounced asymmetry with respect to the applied voltage and unexpected sign changes. These observations indicate that the field distribution in those windows is relatively weak and inhomogeneous compared to the windows depicted in Fig. 6.3.

The contact pairs and GaAs windows are also characterized with respect to their current-voltage characteristic. In particular, it is tested whether the additional second harmonic pump pulse is able to significantly reduce the resistance and enhance the induced

current. An additional excitation is necessary since the metal-semiconductor junction and the intrinsic GaAs in between result in a high resistance. Indeed, if a constant voltage of 10 V is applied to the windows depicted in Fig. 6.3 without optical excitation, a current of only 20 nA is measured. If the polarity is reversed, the current amplitude drops to 3 nA. This asymmetry indicates that the junction rather behaves like a Schottky contact.

The current measurements at the two windows are consecutively repeated with additional optical excitation by the second harmonic pump beam. With a spot diameter of about 20 µm, the optically excited area exceeds the gap width of 12 µm. The peak intensity is in the order of 1 GW/cm^2 and results in an approximated carrier density of $5 \cdot 10^{18}$ cm^{-3} in GaAs (cf. chapter 4.2 for calculation). As detailed in chapter 4.3, such a carrier density results in an observable absorption saturation of the second harmonic beam. Therefore, such a carrier density should also be sufficient to result in a significant voltage-induced occupation asymmetry of the optically addressed states.

As a consequence of the optical excitation, the current in the GaAs windows is significantly increased. If a voltage of 10 V is applied to the contact pair, an average current of about 20 µA is induced. With a beam diameter of 20 µm and an absorption length of 670 nm, the current density calculates to 150 A/cm^2. The peak density may even by higher since the optical excitation is pulsed. If the polarity of the voltage is inverted, the maximum current changes by only a few microampere, indicating a rather ohmic behavior of the illuminated junction.

In conclusion, it can be shown that the sample geometry is suitable to induce significant currents in the GaAs windows. On the basis of the aforementioned measurement series, the two windows which are depicted in Fig. 6.3 are chosen for an exemplary application of the optical current detection technique. The experimental results are presented and discussed in the following chapter.

6.3 Application of the Current Detection Technique

The proposed optical current detection technique is based on the phase-dependent influence of a current on the transmission of a coherent two-color pulse pair. Such transmission measurements are presented and discussed in the following. Within this context, disturbing influences by second harmonic generation in the sample itself are investigated.

Voltage-Dependent Transmission Measurements

The optical current detection technique is consecutively applied to the two GaAs windows depicted in Fig. 6.3. In essence, the pulse pair transmission is measured as a function of their relative optical phase and the current amplitude which is induced in the window.

As detailed in chapter 6.1, the latter determines the asymmetry of the carrier distribution of the current with respect to the crystal momentum. The relative phase of the pulse pair components determines the asymmetry of the optical transitions. If the transitions predominantly address electronic states which are already occupied by the current, the transmission is expected to be increased because of absorption saturation.

The absorption saturation and thus the sensitivity of the current detection technique depend on the mutual coherence of the pulse pair components. Therefore, special attention is paid to ensure collinear propagation and focusing of the pulse pair. To this end, the GaAs sample is exchanged with a beam profiler during adjustment. Furthermore, it is verified that the polarization of both pulse pair components coincides with the direction of the voltage-induced current. In this way, the pulse pairs and the current address the same electronic states.

By monitoring the beam transmission with a photodiode, the foci of the beams can be accurately aligned on a GaAs window. The transmission signal reaches its maximum if the beams are focused on the center of the gap. An unintended illumination of the neighboring metal contacts or the thicker GaAs substrate can be directly identified by a reduced transmission.

In order to adjust the temporal overlap of the pulse pair components, the amplitude of the coherently injected current is measured. For this purpose, the contact pairs are connected to a lock-in amplifier that is referenced to a chopper at the laser output. By changing the length of the fundamental beam arm, current interferograms similar to the one depicted in Fig. 3.3 are recorded. During these measurements, the second harmonic pump beam is blocked. Although the windows consist of nominally intrinsic GaAs instead of LT-GaAs, both windows yield relatively high current amplitudes. At peak intensities of about 6 GW/cm^2 for the fundamental beam and 200 MW/cm^2 for the second harmonic component, the maximum peak to peak current amplitudes are in the order of 200 nA. These relatively high current amplitudes are probably related to the low gap width and defect states that act similar to the defects in LT-GaAs.

The current to be probed is generated by an external voltage at a position which is determined by the second harmonic pump beam. Therefore, it is desirable to optimize the overlap of the foci of the pulse pair components on the one hand and the focus of the second harmonic pump beam on the other hand. To this end, the pulse pair transmission is monitored while adjusting the alignment and the delay τ_{pump} of the second harmonic pump beam. Even without application of an external voltage, the massive carrier excitation by the pump pulse results in a transmission change due to absorption saturation. While the spatial alignment of the pump beam is adjusted to maximize absorption saturation, τ_{pump} is set such that each pump pulse precedes a pulse pair by a few picoseconds. In this way, it is on the one hand ensured that the coherent transitions by the pulse pair are induced in an

already quasi-thermalized carrier distribution with a well-defined asymmetry, determined by the external voltage. On the other hand, such a delay is not long enough for the distribution to fully recombine across the band gap.

After adjustment, the GaAs windows and the current within are probed by phase-resolved measurements of the transmission of one pulse pair component. For this purpose, the relative delay τ between the pulse pair components is slightly varied around maximum temporal overlap while keeping the delay τ_{pump} of the pump beam constant. A photodiode behind the sample records the intensity of the transmitted beam. The pulse pair component to be monitored is selected by an additional longpass or shortpass filter in front of the photodiode. To check for reproducibility, the measurements are performed at both windows depicted in Fig. 6.3.

Despite careful alignment, measurements with the fundamental beam component do not show a significant and reproducible phase-dependent transmission signal. However, this observation is not unexpected since the fundamental beam may only interact via two-photon transitions. Given the same illumination intensity, these are less likely than corresponding one-photon transitions. Therefore, the following measurements concentrate on the transmission of the second harmonic beam.

Fig. 6.4(a) exemplarily depicts the transmission of the second harmonic pulse pair component. A lock-in amplifier records the response of the photodiode. It is referenced to a chopper in the arm of the fundamental pulse pair component. In this way, stray light by the second harmonic pump beam is suppressed. During the measurement, a fixed voltage of -10 V, 0 V or $+10$ V is applied to the contacts. The delay τ_{pump} is set such that each pump pulse precedes a pulse pair by 2.5 ps. The approximated peak illumination intensities on the window are 6 GW/cm^2 for the fundamental pulse pair component, 200 MW/cm^2 for the second harmonic pulse pair component and 700 MW/cm^2 for the additional second harmonic pump beam. It should be noted that the current saturation which is presented and discussed in chapter 4 is rather small at such pulse pair intensities (cf. Fig. 4.2(a)).

Fig. 6.4(a) reveals distinct oscillations of the transmission with respect to the delay τ. Similar to the measurements of QUIC (cf. Fig. 3.3(b)), the oscillation period corresponds to the wavelength of the second harmonic pulse pair component. The oscillation amplitudes are in the order of 10^{-3}. These are calculated by normalizing the signal to the total intensity of the transmitted second harmonic pulse pair component. The latter is determined by referencing the lock-in amplifier to a chopper in the corresponding beam arm.

Apart from the oscillating signal, the recorded transmissions also contain phase-independent components in the order of 10^{-2}. These may for instance be caused by the optically induced increase of the total carrier density. Since the proposed optical current detection explicitly depends on the relative phase, the constant components are not

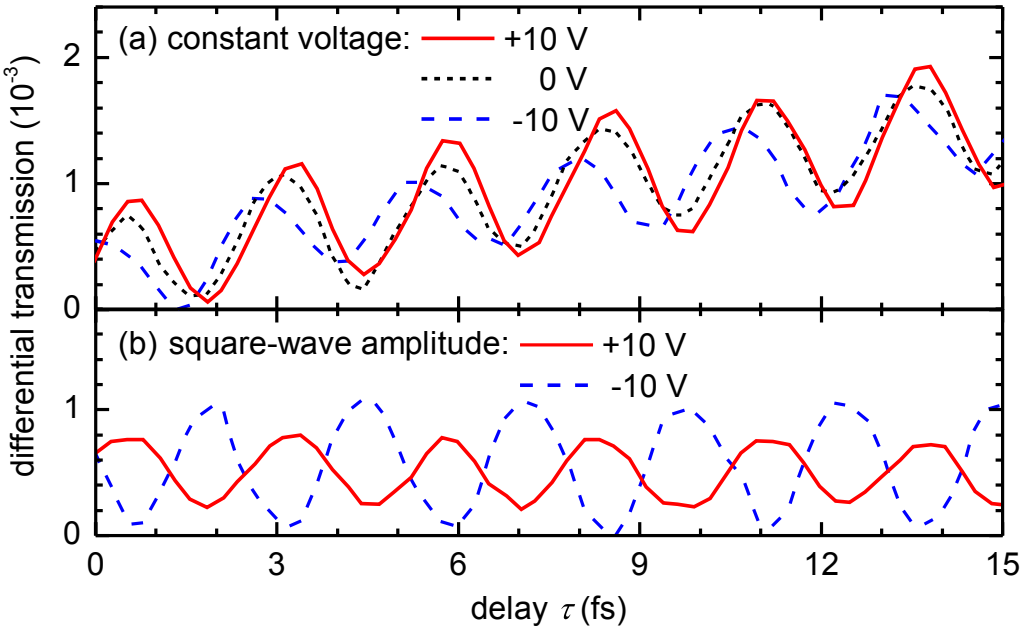

Fig. 6.4: Differential transmission of the second harmonic pulse pair component as a function of the relative delay τ between the pulse pair components for different voltages applied to the illuminated GaAs window. Approximated peak illumination intensities are 6 GW/cm^2 for the fundamental pulse pair component, 200 MW/cm^2 for the second harmonic pulse pair component and 700 MW/cm^2 for the additional second harmonic pump pulse. (a) Signal recorded with a constant voltage and the lock-in amplifier referenced to a chopper in the fundamental beam arm. (b) Signal recorded by referencing the lock-in amplifier to a square-wave voltage. Both signals are normalized to the total transmission of the second harmonic pulse pair component. A constant offset is subtracted from both graphs.

analyzed in more detail and subtracted from the graph.

The voltage dependence of the oscillation amplitudes is less pronounced than expected. In fact, the oscillation is even present if no voltage is applied to the GaAs window. In case that the oscillation is solely caused by the current-induced transmission increase detailed in chapter 6.1, the oscillation would be expected to vanish if no current and thus no asymmetry of the carrier distribution is present. Therefore, these oscillations must have another origin that is discussed in more detail below.

Most strikingly, an increase of the applied voltage results in a significant shift of the oscillation with respect to the delay τ. In order to separate this effect from the voltage-independent oscillation, another measurement technique is used. Instead of the chopper in the fundamental beam arm, the lock-in amplifier is referenced to a square-wave voltage that is applied to the sample. The square wave-voltage alternates with a frequency of 571 Hz between 0 V and up to $\pm$10 V. In this way, the measurement is only sensitive to voltage-induced transmission changes.

Exemplary measurements of the voltage-induced transmission changes are shown in Fig. 6.4(b). The corresponding experimental parameters, e.g. irradiances or pulse delays, are the same as in Fig. 6.4(a). Therefore, the differential transmission can be normalized in the same way. Furthermore, phase-independent offsets are subtracted. The two curves correspond to measurements employing square-wave voltages with the same amplitude of 10 V but with different polarity.

Both curves feature similar oscillation amplitudes and the same oscillation period as the curves in Fig. 6.4(a). However, the phases of the two curves differ by π and therefore correlate with the orientation of the applied voltage. Such a behavior is in agreement with the voltage-dependent phase shift of the three curves in Fig. 6.4(a). The observed oscillations can be thought of as a superposition of two slightly shifted oscillations, a voltage-independent component and a voltage-dependent component.

In order to investigate the underlying mechanism of the voltage-dependent component, the corresponding oscillation amplitudes are determined as a function of the illumination intensity. To this end, measurements as shown in Fig. 6.4(b) are repeated with different intensity combinations of both pulse pair components. If the intensity of the second harmonic component is kept constant, the extracted oscillation amplitudes scale linearly with the intensity of the fundamental beam. If the intensity of the fundamental component is kept constant, the oscillation amplitudes scale with the root of the second harmonic irradiance. Taken together, the phase-dependent transmission scales in the same way as the QUIC amplitude. However, the intensity dependence alone is not sufficient to identify QUIC as the origin of the transmission oscillation. At least, it can be concluded that the transmission signal originates from a nonlinear optical effect.

Influence of Second Harmonic Generation

The fact that the transmission signal features a sine-like phase dependence even if no voltage is applied to the GaAs windows indicates the influence of another effect than current-induced absorption saturation. A potential candidate for such an effect is second harmonic generation (SHG) in the GaAs sample itself [118, and references within; 119]. If the fundamental pulse pair component is frequency-doubled in the GaAs window, the emergent beam exhibits the same wavelength and propagation direction as the second harmonic pulse pair component. As a consequence, the illumination intensity on the photodiode would also be determined by the interference of the two second harmonic beams. In particular, the intensity would exhibit the same oscillation period as the oscillations in Fig. 6.4(a).

SHG in the GaAs window can be identified by a spectrally-resolved measurement. To this end, the photodiode behind the sample is exchanged with a spectrometer. During such

a measurement, only the fundamental beam is focused on the GaAs window. The other two second harmonic beams are blocked as their high intensity would saturate the spectrometer and perturb the measurement. For the same reason, the transmitted fundamental beam is prevented from entering the spectrometer by a shortpass filter between the sample and the detector.

If the fundamental beam is focused on the GaAs window, the spectrometer indeed reveals a peak at the second harmonic wavelength. According spectra are depicted in Fig. 6.5(a) for an exemplary fundamental beam intensity of 6 GW/cm^2. The peak features a central wavelength of about 780 nm, which is half the input beams' central wavelength of about 1550 nm. Utilizing again the photodiode, the integrated intensity of the emerging second harmonic component can be estimated to about 0.3 nW.

Application of a voltage to the GaAs window significantly influences the spectral amplitude of the second harmonic component. In this case, a voltage of +20 V causes an increase of up to 50 %. On the contrary, a negative voltage results in a slight decrease of the amplitude. It should be noted that the application of a voltage of ±10 V, which is used in the previous measurements, has a qualitatively similar but less pronounced influence on the spectral amplitudes.

To affirm that the spectral peaks stem from SHG in the sample, their dependence on the input beam intensity is analyzed. For example, improper filtering in the two-color interferometer could result in a residual second harmonic beam component in the fundamental arm. The intensity of such a second harmonic component would scale linearly

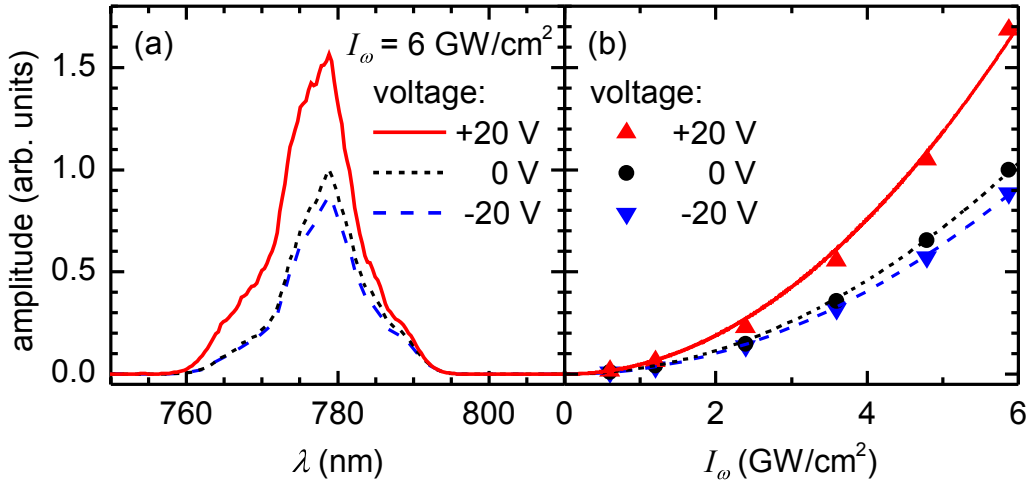

Fig. 6.5: (a) Spectra of the second harmonic signal behind the GaAs sample at a fixed intensity of the fundamental input beam and different voltages applied to the contact pair. (b) Integrated intensity of the second harmonic peaks as a function of the fundamental beam intensity and the applied voltage. The curves correspond to parabolic fits.

with the attenuation of the fundamental beam arm. In contrast, the intensity of SHG scales with the squared intensity of the fundamental input beam. Therefore, spectra of the second harmonic component are acquired for different fundamental beam intensities. Subsequently, the integrated intensity of the peaks is extracted.

Fig. 6.5(b) plots the integrated intensity of the second harmonic component as a function of the fundamental beam intensity and the applied voltage. As expected for SHG, the data points agree well with parabolic fits which are illustrated by curves. If a positive or negative voltage is applied to the GaAs window, the respective scaling factor of the parabolic fits is higher or lower than without a voltage. Similar to Fig. 6.5(a), the amplitude increase at positive voltages is much higher than the decrease at negative voltages. The underlying mechanism of this voltage dependence is addressed later in the chapter. First, the discussion focuses on the influence of SHG on the previously presented transmission measurements for the case that no voltage is applied to the sample.

During transmission measurements, the photodiode is simultaneously illuminated by two second harmonic beams. On the one hand, the pulses from the second harmonic arm of the interferometer transmit through the sample and hit the detector. On the other hand, as described above, the pulses from the fundamental arm generate an additional beam by SHG in the sample. Since the pulses from both second harmonic beams feature the same central wavelength and overlap spatially as well as temporally, the intensity on the detector is modulated by interference. This intensity can be described by a superposition of the corresponding electric field amplitudes E:

$$|E_{2\omega,\mathrm{trans}} + E_{2\omega,\mathrm{SHG}}|^2 \propto I_{2\omega,\mathrm{trans}} + 2\cos(\Delta\phi_{2\omega})\sqrt{I_{2\omega,\mathrm{trans}} \cdot I_{2\omega,\mathrm{SHG}}} + I_{2\omega,\mathrm{SHG}} \tag{6.2}$$

Here, the index "trans" refers to the transmitted beam from the second harmonic arm and "SHG" to the beam that is generated in the sample. The first and third term on the right-hand side of the equation denote the intensities of the individual beams. The interference of both beams is described by the second term. Its sign is determined by the phase difference $\Delta\phi_{2\omega}$ of the pulses. If the relative delay between the pulse pair components in the interferometer is continuously swept, the intensity oscillates with a period that corresponds to the second harmonic wavelength, as it is the case in Fig. 6.4(a).

In order to quantify the influence of interference on the transmission measurements, the oscillation amplitude of the intensity is exemplarily calculated for the measurement depicted in Fig. 6.4(a). The corresponding transmitted average beam power $I_{2\omega,\mathrm{trans}}$ is in the order of 200 µW. As mentioned above, the average second harmonic power $I_{2\omega,\mathrm{SHG}}$ can be estimated to 0.3 nW. If normalized to the total transmission which is dominated by $I_{2\omega,\mathrm{trans}}$, the relative oscillation amplitude is given by $2 \cdot \sqrt{I_{2\omega,\mathrm{SHG}}/I_{2\omega,\mathrm{trans}}}$. Inserting the above mentioned intensities yields a relative oscillation amplitude of $2 \cdot 10^{-3}$.

The calculated interference amplitude exceeds the observed oscillation in Fig. 6.4(a) by a factor of 4. However, it must be taken into account that the calculation assumes optimal coherence of both beams which is not fulfilled in practice. For one, the polarizations of both beams do not coincide but exhibit an angle of 45° with respect to each other. Furthermore, it is not taken care of that the beams propagate collinearly and illuminate the same area on the detector. As a consequence, the intensity interference is reduced compared to the calculation.

Owing to the good agreement of the oscillation amplitudes and the consistent oscillation period, it is reasonable to attribute the voltage-independent oscillation in Fig. 6.4(a) to interference, caused by SHG in the sample. In the following, it is further argued that it is also reasonable to attribute the voltage-dependent oscillation component in Fig. 6.4(b) to interference. Most likely, the application of a voltage influences the second harmonic generation in the sample via EFISH (electric field-induced second harmonic generation).

EFISH refers to frequency-doubling in a material by coupling of the electric field amplitude E_ω of the incident beam with the amplitude of a static electric field E_{DC} [120; 121; 122, and references within]. In terms of nonlinear optics, this effect is described by the fourth-rank tensor $\chi^{(3)}(-2\omega;\omega,\omega,0)$. Omitting the optical polarizations for clarity, the material's polarization P follows the relation

$$P_{\mathrm{EFISH}} \propto \chi^{(3)}(-2\omega;\omega,\omega,0)\, E_\omega^2\, E_{\mathrm{DC}}. \tag{6.3}$$

Since the electric field amplitude of the emitted second harmonic beam scales linearly with the polarization P, the second harmonic intensity is proportional to the square of the fundamental beam intensity, as it is also the case for regular SHG. Additionally, the second harmonic field amplitude is proportional to the static field amplitude E_{DC}. As a consequence, the phase is shifted by π upon a reversal of the polarity of the constant field [123].

Referring back to Fig. 6.5, the voltage-induced difference of the detected second harmonic intensity can be attributed to EFISH. Conventional SHG and EFISH both cause frequency-doubling of the incident fundamental beam. As evident from the good agreement with the parabolic fits, the voltage-induced difference in amplitude follows the quadratic intensity dependence of EFISH. On the basis of reference transmission measurements with the second harmonic pulse pair component, it can be ruled out that the difference is simply caused by a voltage-dependent absorption in the sample. The fact that depending on the voltage polarity the intensity is either increased or decreased can be explained by interference.

The spectrometer detects a superposition of two second harmonic components generated by conventional SHG as well as EFISH. Depending on their relative optical phase, these

interfere constructively or destructively. While the optical phase of the conventional SHG component is fixed, the EFISH component depends on the orientation of the static field. As a result the total intensity may be decreased upon application of a negative voltage.

A simultaneous generation of an EFISH component and of a field-independent SHG component in the sample is also consistent with the oscillations in Fig. 6.4(a). As mentioned above, the voltage-induced phase shift can be interpreted as a superposition of two oscillations, a voltage-independent component and a voltage-induced component. The former can be explained by interference of the second harmonic pulse pair component with SHG in the sample. The voltage-induced oscillation can be attributed to interference with an EFISH component. Consistent with the field dependence of EFISH, the voltage-induced oscillation in Fig. 6.4(b) is shifted by π if the polarity is inverted.

Apart from a phase shift in Fig. 6.4(a), the superposition of both oscillation components results in an increase of the oscillation amplitude for positive voltages and a decrease for negative voltages. This behavior is in qualitative agreement with the detected second harmonic intensity in Fig. 6.5. Quantitatively, the detected intensity difference does not match the relative amplitudes of the SHG and EFISH oscillation component even if twice the voltage is applied to the sample. However, it must be taken into account that the experimental conditions of both measurements differ. In contrast to the transmission measurements, the GaAs window and the contact pair are only illuminated by the fundamental beam during the spectral measurements.

Without illumination by a second harmonic beam, whose energy exceeds the band gap, the semiconductor-metal junction behaves rather like a high-resistive Schottky contact. As affirmed by the previously mentioned current-voltage characteristics, the penetration of the electric field into such a junction is reduced and asymmetric with respect to the polarity of the applied voltage. Consequently, the EFISH component in such a junction also features a reduced and asymmetric voltage-dependence. Therefore, the lack of a pump beam is able to resolve the discrepancy between the spectral measurements and the transmission measurements.

In summary, it can be concluded that the presented transmission measurements are dominated, if not fully determined, by interference of second harmonic components generated by SHG and EFISH. Measurements with lower intensity combinations of the pulse pair than in the measurement depicted in Fig. 6.4 show similar results. In fact, a reduction of the intensity is not expected to alter the amplitude relation between QUIC and interference by second harmonic generation.

QUIC, which is the underlying effect of the proposed optical current detection, and interference by second harmonic generation both exhibit the same intensity dependence. As evident from equation 6.2, intensity interference is proportional to the square root of

the intensity of both interfering second harmonic components. The intensity of second harmonic generation in the sample is in turn proportional to the squared intensity of the incident fundamental beam. Consequently, the oscillation amplitude scales with $\sqrt{I_{2\omega}}\, I_{\omega}$, similar to QUIC. As already mentioned, such scaling is also observed for the amplitude of the voltage-induced oscillations of the transmission measurements.

6.4 Conclusion and Outlook

An experimental implementation of the optical current detection scheme proposed by Liu *et al.* [35; 36] is presented and evaluated. The detection scheme is based on QUIC by a two-color pulse pair incident on the sample to be probed. Via the relative phase and polarization of the pulse pair components, the crystal momentum of the optically addressed electronic states can be controlled. If these electronic states are already occupied, the transmission of the pulse pair is expected to be increased because of absorption saturation. Such a selective absorption saturation would allow to sense an anisotropic carrier distribution which corresponds to the presence of a current. In specific, the current should manifest in the dependence of the transmission on the relative phase of the pulse pair.

The presented implementation of the detection technique is designed for an exemplary application at a voltage-induced current in a thin GaAs sample. Via frequency-doubling of ultrashort laser pulses in a nonlinear crystal and a subsequent interferometer, collinear coherent pulse pairs are provided; their components can be individually adjusted in intensity, relative delay and polarization. In essence, the sample to be probed consists of a thin layer of GaAs with metallic contacts on top to apply a voltage. In order to increase the amplitude of the induced current, the sample is further excited by an additional laser beam. The sample thickness is chosen such that components of the fundamental wavelength of 1.55 µm as well as of its second harmonic are transmitted. These transmitted components are recorded with a detector behind the sample.

On the basis of independent control measurements, it can be demonstrated that the setup fulfills the fundamental requirements of the proposed detection technique. Measurements of QUIC in the sample confirm a precise and coherent superposition of the pulse pair components. Therefore, the pulse pairs allow for a selective optical excitation of electronic states. Moreover, current-voltage characteristics imply a significant and localized current induction in the GaAs layer by the metallic contacts on top and selective optical excitation with the pump beam. The calculated excitation density corresponds to a massive population of the electronic bands that should result in a significant influence on the pulse pair transmission.

Despite careful design and optimization of the setup, the transmission measurements do not allow to deduce an influence by current-dependent saturation absorption. The

transmission of the fundamental beam does not feature a significant and reproducible dependence on the relative phase of the pulse pair. This result is not unexpected since the fundamental beam may only interact with the electronic states via two-photon absorption. In contrast, the second harmonic beam is able to directly address the electronic states. However, these measurements are perturbed by interference which can be attributed to second harmonic generation in the sample.

The focused illumination of the GaAs sample by the fundamental beam results in frequency-doubling which is verified by spectrally-resolved measurements. An additional voltage application influences the frequency-doubling in the sample by electric field-induced second harmonic generation (EFISH). As a consequence, the transmitted second harmonic pulse pair component interferes with the additionally generated second harmonic beam. The resulting intensity interference on the detector features a similar phase- and voltage-dependence as the predicted absorption saturation. Furthermore, QUIC and the interference follow the same intensity dependence. Therefore, a potential influence by current-dependent saturation absorption cannot simply be separated from the pronounced intensity interference.

There is still room for potential improvements of the setup which have not been tested yet because of their relatively high effort. By using another laser system with a longer wavelength, the sensitivity to the anisotropic carrier distribution could be enhanced. If the optically probed electronic states are closer to the band gap, they should be more influenced by the quasi-thermalized carrier distribution. Aside from that, the second harmonic generation could be reduced if another sample is used which is fabricated from another material or exhibits another crystal orientation. However, it must be taken into account that the reduction of such a nonlinear response may also be accompanied by a reduction of the magnitude of QUIC.

Apart from the aforementioned improvements, it could be tested whether the detection scheme is applicable on spin currents. Spin currents arise when carrier distributions of different spin states feature unequal anisotropies. Utilizing orthogonally polarized pulse pairs, coherence control has been demonstrate for the injection of pure spin currents with no net charge transfer [55–58]. Similar to coherent charge current injection, the spin current direction can be controlled by the pulse pair's relative polarization and optical phase. Conversely, a spin current should also manifest in the beam transmission, since the pulse pair addresses specific spin states. However, in the case of pure spin currents which do not result in a charge imbalance, the influence of EFISH should be minimized.

Chapter 7

Summary

This thesis covers physics and applications of coherently controlled current injection (QUIC) in the prototypical direct band gap semiconductor GaAs. QUIC is a nonlinear optical process that allows to inject currents by all-optical means. An ultrashort two-color laser pulse pair which is incident on a GaAs sample causes an interference of electronic transitions. Eventually, this quantum interference results in an ultrafast current burst. Its direction and amplitude can be controlled by the relative phase and polarization of the pulses. The use of low-temperature grown GaAs (LT-GaAs) allows to measure the current via metallic contacts on top of the sample. Essentially, defects in LT-GaAs freeze the charge separation of ultrafast current bursts and prevent it from a rapid recombination.

The first part of the thesis addresses the high-intensity regime of QUIC for which significant deviations from the initial theoretical description are predicted. Indeed, a collaborative experimental and theoretical study shows a pronounced current saturation at elevated intensities. Partly, the observed deviations can be attributed to an increased recombination of the induced charge dipole. Pump-probe type measurements and theoretical calculations also indicate significant deviations of the injection process itself. If the illumination intensity is increased, the induced transition rates eventually stagnate as there is only a finite number of optically addressable states. Therefore, the current injection is reduced due to absorption saturation of the laser pulses. Furthermore, the increased coupling between the carriers and the electric field amplitudes of the pulses can result in a breakdown of the perturbative description of the light-matter interaction.

In the second part of the thesis it is demonstrated that QUIC can be utilized to retrieve the spectral phase of ultrashort laser pulses. A specific combination of the beam to be characterized and its second harmonic is focused on a contacted LT-GaAs sample. The injected current is measured as a function of the temporal delay of these beams. Owing to the explicit phase dependence of QUIC, the spectral phase of the incident pulses, in particular their group velocity dispersion (GVD), can be directly retrieved from a Fourier transform of the current measurement. For a quantitative evaluation, the measurement

scheme is applied to differently chirped pulses with a central wavelength of 1.5 µm and a nominal pulse duration of 50 fs. With respect to typical experimental conditions, the retrieved GVD values are in good agreement with reference measurements by SHG-FROG.

The last part of the thesis discusses the experimental implementation of a proposed QUIC-based current detection scheme. In essence, a current in a semiconductor is predicted to manifest in the transmission of an incident two-color pulse pair. Depending on the relative phase of the two pulses, their absorption is expected to be reduced. This detection scheme is exemplarily applied to a voltage-induced current in a thin GaAs sample. The transmission of the pulse pairs is measured as a function of the relative optical phase as well as the current amplitude. It can be shown that the setup fulfills the fundamental requirements of the proposal. However, it turns out that interference by second harmonic generation in the sample perturbs the experimental implementation of the optical current detection scheme.

In conclusion, this thesis gives new insights into the physics and practical applications of QUIC. The study of the high-intensity regime advances the understanding of QUIC concerning the underlying light-matter interaction as well as the subsequent current dynamics. The prototype of the phase-retrieval scheme demonstrates that QUIC can provide a reliable alternative to existing methods for the temporal characterization of ultrashort laser pulses. Further modifications of the setup could improve the accuracy of this technique and extend its range of applicability. Although the all-optical current detection scheme could not be demonstrated experimentally, the study allows to identify the disturbing influences and to deduce practical solutions for future investigations.

Bibliography

[1] T. H. Maiman, "Stimulated Optical Radiation in Ruby," *Nature* **187**, 493 (1960)

[2] R. J. Collins, D. F. Nelson, A. L. Schawlow, W. Bond, C. G. B. Garrett and W. Kaiser, "Coherence, Narrowing, Directionality, and Relaxation Oscillations in the Light Emission from Ruby," *Physical Review Letters* **5**, 303 (1960)

[3] A. Javan, W. R. Bennett, Jr. and D. R. Herriott, "Population Inversion and Continuous Optical Maser Oscillation in a Gas Discharge Containing a He-Ne Mixture," *Physical Review Letters* **6**, 106 (1961)

[4] R. W. Boyd, *Nonlinear Optics* (Academic Press, San Diego, 1992)

[5] G. P. Agrawal and R. W. Boyd, eds., *Contemporary Nonlinear Optics* (Academic Press, San Diego, 1992)

[6] P. A. Franken, A. E. Hill, C. W. Peters and G. Weinreich, "Generation of Optical Harmonics," *Physical Review Letters* **7**, 118 (1961)

[7] R. Atanasov, A. Haché, J. L. P. Hughes, H. M. van Driel and J. E. Sipe, "Coherent Control of Photocurrent Generation in Bulk Semiconductors," *Physical Review Letters* **76**, 1703 (1996)

[8] A. Haché, Y. Kostoulas, R. Atanasov, J. L. P. Hughes, J. E. Sipe and H. M. van Driel, "Observation of Coherently Controlled Photocurrent in Unbiased, Bulk GaAs," *Physical Review Letters* **78**, 306 (1997)

[9] A. Haché, J. E. Sipe and H. M. van Driel, "Quantum Interference Control of Electrical Currents in GaAs," *IEEE Journal of Quantum Electronics* **34**, 1144 (1998)

[10] M. Göppert-Mayer, "Über Elementarakte mit zwei Quantensprüngen," *Annalen der Physik* **401**, 273 (1931)

[11] W. Kaiser and C. G. B. Garrett, "Two-Photon Excitation in CaF_2:Eu^{2+}," *Physical Review Letters* **7**, 229 (1961)

[12] F. Krausz, M. E. Fermann, T. Brabec, P. F. Curley, M. Hofer, M. H. Ober, C. Spielmann, E. Wintner and A. J. Schmidt, "Femtosecond Solid-State Lasers," *IEEE Journal of Quantum Electronics* **28**, 2097 (1992)

[13] U. Keller, "Recent developments in compact ultrafast lasers," *Nature* **424**, 831 (2003)

[14] L. Costa, M. Betz, M. Spasenović, A. D. Bristow and H. M. van Driel, "All-optical injection of ballistic electrical currents in unbiased silicon," *Nature Physics* **3**, 632 (2007)

[15] M. Spasenović, M. Betz, L. Costa and H. M. van Driel, "All-optical coherent control of electrical currents in centrosymmetric semiconductors," *Physical Review B* **77**, 085201 (2008)

[16] D. Sun, C. Divin, J. Rioux, J. E. Sipe, C. Berger, W. A. de Heer, P. N. First and T. B. Norris, "Coherent Control of Ballistic Photocurrents in Multilayer Epitaxial Graphene Using Quantum Interference," *Nano Letters* **10**, 1293 (2010)

[17] D. A. Bas, K. Vargas-Velez, S. Babakiray, T. A. Johnson, P. Borisov, T. D. Stanescu, D. Lederman and A. D. Bristow, "Coherent control of injection currents in high-quality films of Bi_2Se_3," *Applied Physics Letters* **106**, 041109 (2015)

[18] J. Güdde, M. Rohleder, T. Meier, S. W. Koch and U. Höfer, "Time-Resolved Investigation of Coherently Controlled Electric Currents at a Metal Surface," *Science* **318**, 1287 (2007)

[19] D. Côté, J. M. Fraser, M. DeCamp, P. H. Bucksbaum and H. M. van Driel, "THz emission from coherently controlled photocurrents in GaAs," *Applied Physics Letters* **75**, 3959 (1999)

[20] R. W. Newson, J.-M. Ménard, C. Sames, M. Betz and H. M. van Driel, "Coherently Controlled Ballistic Charge Currents Injected in Single-Walled Carbon Nanotubes and Graphite," *Nano Letters* **8**, 1586 (2008)

[21] R. W. Newson, A. A. Green M. C Hersam and H. M. van Driel, "Coherent injection and control of ballistic charge currents in single-walled carbon nanotubes and graphite," *Physical Review B* **83**, 115421 (2011)

[22] C. Ruppert, S. Thunich, G. Abstreiter, A. Fontcuberta i Morral, A. W. Holleitner and M. Betz, "Quantum Interference Control of Femtosecond, μA Current Bursts in Single GaAs Nanowires," *Nano Letters* **10**, 1799 (2010)

[23] S. Thunich, C. Ruppert, A. W. Holleitner and M. Betz, "Field-resolved characterization of femtosecond electromagnetic pulses with 400 THz bandwidth," *Optics Letters* **36**, 1791 (2011)

[24] C. Ruppert, J. Lohrenz, S. Thunich and M. Betz, "Ultrafast field-resolved semiconductor spectroscopy utilizing quantum interference control of currents," *Optics Letters* **37**, 3879 (2012)

[25] P. A. Roos, Q. Quraishi, S. T. Cundiff, R. D. R. Bhat and J. E. Sipe, "Characterization of quantum interference control of injected currents in LT-GaAs for carrier-envelope phase measurements," *Optics Express* **11**, 2081 (2003)

[26] T. M. Fortier, P. A. Roos, D. J. Jones.and S. T. Cundiff, R. D. R. Bhat and J. E. Sipe, "Carrier-Envelope Phase-Controlled Quantum Interference of Injected Photocurrents in Semiconductors," *Physical Review Letters* **92**, 147403 (2004)

[27] B. E. A. Saleh and M. C. Teich, *Fundamentals of Photonics*, 2nd ed., 3rd printing (John Wiley & Sons, Hoboken, 2007)

[28] S. Hooker and C. Webb, *Laser Physics* (Oxford University Press, Oxford, 2010)

[29] *Fundamental Optics*, Tutorial by IDEX Optics & Photonics Marketplace, available at `http://marketplace.idexop.com/store/technical-library` (last accessed on July 16, 2015)

[30] I. A. Walmsley and C. Dorrer, "Characterization of ultrashort electromagnetic pulses," *Advances in Optics and Photonics* **1**, 308 (2009)

[31] Antoine Monmayrant, Sbastien Weber and Batrice Chatel, "A newcomer's guide to ultrashort pulse shaping and characterization," *Journal of Physics B: Atomic, Molecular and Optical Physics* **43**, 103001 (2010)

[32] D. J. Kane and R. Trebino, "Single-shot measurement of the intensity and phase of an arbitrary ultrashort pulse by using frequency-resolved optical gating," *Optics Letters* **18**, 823 (1993)

[33] D. J. Kane and R. Trebino, "Characterization of Arbitrary Femtosecond Pulses Using Frequency-Resolved Optical Gating," *IEEE Journal of Quantum Electronics* **29**, 571 (1993)

[34] K. W. DeLong, R. Trebino, J. Hunter and W. E. White, "Frequency-resolved optical gating with the use of second-harmonic generation," *Journal of the Optical Society of America B* **11**, 2206 (1994)

[35] J.-T. Liu, F.-H. Su, X.-H. Deng and H. Wang, "Proposal for the momentum-resolved and time-resolved optical measurement of the current distribution in semiconductors," *Optics Express* **20**, 11694 (2012)

[36] J.-T. Liu, F.-H. Su, X.-H. Deng and H. Wang, "Direct map of the scattering current in real time by using the two-color optical coherence absorption spectrum," *Europhysics Letters* **99**, 67008 (2012)

[37] S. Ziegler, R. C. Woodward, H. H.-C. Iu and L. J. Borle, "Current Sensing Techniques: A Review," *IEEE Sensors Journal* **9**, 354 (2009)

[38] P. Ripka, "Electric current sensors: a review," *Measurement Science and Technology* **21**, 112001 (2010)

[39] H. T. Duc, T. Meier and S. W. Koch, "Microscopic Analysis of the Coherent Optical Generation and the Decay of Charge and Spin Currents in Semiconductor Heterostructures," *Physical Review Letters* **95**, 086606 (2005)

[40] H. T. Duc, Q. T. Vu, T. Meier, H. Haug and S. W. Koch, "Temporal decay of coherently optically injected charge and spin currents due to carrier-LO-phonon and carrier-carrier scattering," *Physical Review B* **74**, 165328 (2006)

[41] B. Pasenow, H. T. Duc, T. Meier and S. W. Koch, "Rabi flopping of charge and spin currents generated by ultrafast two-colour photoexcitation of semiconductor quantum wells," *Solid State Communications* **145**, 61 (2008)

[42] M. Pochwała, H. T. Duc, J. Förstner and T. Meier, "Intensity-dependent ultrafast dynamics of injection currents in unbiased GaAs quantum wells," *Physica Status Solidi – Rapid Research Letters* **5**, 119 (2011)

[43] T. Jostmeier, *Kohärente Kontrolle elektrischer Ströme in Galliumarsenid: Signaturen jenseits des störungstheoretischen $\chi^{(3)}$-Limits*, Master's thesis (TU Dortmund University, Dortmund, 2012)

[44] E. Sternemann, T. Jostmeier, C. Ruppert, H. T. Duc, T. Meier and M. Betz, "Femtosecond quantum interference control of electrical currents in GaAs: Signatures beyond the perturbative $\chi^{(3)}$ limit," *Physical Review B* **88**, 165204 (2013)

[45] E. Sternemann, M. Betz and C. Ruppert, "Phase-retrieval of femtosecond pulses utilizing $\omega/2\omega$ quantum interference control of electrical currents," *Optics Letters* **39**, 3654 (2014)

[46] E. Sternemann, T. Jostmeier, C. Ruppert, S. Thunich, H. T. Duc, R. Podzimski, T. Meier and M. Betz, "Quantum Interference Control of Electrical Currents in GaAs Microstructures: Physics and Spectroscopic Applications," submitted (2015)

[47] M. Fox, *Optical Properties of Solids*, 2nd ed. (Oxford University Press, Oxford, 2010)

[48] H. M. van Driel and J. E. Sipe, "Coherent Control of Photocurrents in Semiconductors," in *Ultrafast Phenomena in Semiconductors*, ed. by K.-T. Tsen (Springer, New York, 2001), ch. 5

[49] E. Dupont, P. B. Corkum, H. C. Liu, M. Buchanan and Z. R. Wasilewski, "Phase-Controlled Currents in Semiconductors," *Physical Review Letters* **74**, 3596 (1995)

[50] N. W. Ashcroft and N. D. Mermin, *Solid State Physics* (Thomson Learning, London, 1976)

[51] N. Laman, A. I. Shkrebtii, J. E. Sipe and H. M. van Driel, "Quantum interference control of currents in CdSe with a single optical beam," *Applied Physics Letters* **75**, 2581 (1999)

[52] J. J. Sakurai, *Modern Quantum Mechanics*, ed. by S. F. Tuan, rev. ed. (Addison-Wesley, Reading, 1994)

[53] J. S. Blakemore, "Semiconducting and other major properties of gallium arsenide," *Journal of Applied Physics* **53**, R123 (1982)

[54] C. Aversa and J. E. Sipe, "Coherent Current Control in Semiconductors: A Susceptibility Perspective," *IEEE Journal of Quantum Electronics* **32**, 1570 (1996)

[55] R. D. R. Bhat and J. E. Sipe, "Optically Injected Spin Currents in Semiconductors," *Physical Review Letters* **85**, 5432 (2000)

[56] M. J. Stevens, A. L. Smirl, R. D. R. Bhat, A. Najmaie, J. E. Sipe and H. M. van Driel, "Quantum Interference Control of Ballistic Pure Spin Currents in Semiconductors," *Physical Review Letters* **90**, 136603 (2003)

[57] J. Hübner, W. W. Rühle, M. Klude, D. Hommel, R. D. R. Bhat, J. E. Sipe and H. M. van Driel, "Direct Observation of Optically Injected Spin-Polarized Currents in Semiconductors," *Physical Review Letters* **90**, 216601 (2003)

[58] H. Zhao, A. L. Smirl and H. M. van Driel, "Temporally and spatially resolved ballistic pure spin transport," *Physical Review B* **75**, 075305 (2007)

[59] J. M. Fraser, A. I. Shkrebtii, J. E. Sipe and H. M. van Driel, "Quantum Interference in Electron-Hole Generation in Noncentrosymmetric Semiconductors," *Physical Review Letters* **83**, 4192 (1999)

[60] J. M. Fraser and H. M. van Driel, "Quantum interference control of free-carrier density in GaAs," *Physical Review B* **68**, 085208 (2003)

[61] J. Singleton, *Band Theory and Electronic Properties of Solids* (Oxford University Press, Oxford, 2001)

[62] S. Thunich, C. Ruppert, A. W. Holleitner and M. Betz, "Sub-diffraction optical coherent control of ultrafast electrical currents in antenna devices on GaAs," *Applied Physics Letters* **101**, 251119 (2012)

[63] Z. Lü, D. Zhang, Z. Zhou, L. Sun, Z. Zhao and J. Yuan, "Coherently controlled terahertz source for a time domain spectroscopy system via injection current in bulk ZnSe," *Applied Optics* **51**, 676 (2012)

[64] J.-C. Diels and W. Rudolph, *Ultrashort Laser Pulse Phenomena: Fundamentals, Techniques, and Applications on a Femtosecond Time Scale* (Academic Press, San Diego, 1996)

[65] H. A. Haus, E. P. Ippen and K. Tamura, "Additive-Pulse Modelocking in Fiber Lasers," *IEEE Journal of Quantum Electronics* **30**, 200 (1994)

[66] J. H. Davies, *The Physics of Low-Dimensional Semiconductors: An Introduction* (Cambridge University Press, Cambridge, 1998)

[67] H. Zhao, E. J. Loren, A. L. Smirl and H. M. van Driel, "Dynamics of charge currents ballistically injected in GaAs by quantum interference," *Journal of Applied Physics* **103**, 053510 (2008)

[68] D. C. Look, "Molecular beam epitaxial GaAs grown at low temperatures," *Thin Solid Films* **231**, 61 (1993)

[69] M. O. Manasreh, D. C. Look, K. R. Evans and C. E. Stutz, "Infrared absorption of deep defects in molecular-beam-epitaxial GaAs layers grown at 200 °C: Observation of an EL2-like defect," *Physical Review B* **41**, 10272(R) (1990)

[70] T. S. Sosnowski, T. B. Norris, H. H. Wang, P. Grenier, J. F. Whitaker and C. Y. Sung, "High-carrier-density electron dynamics in low-temperature-grown GaAs," *Applied Physics Letters* **70**, 3245 (1997)

[71] T. Elsaesser, J. Shah, L. Rota and P. Lugli, "Initial Thermalization of Photoexcited Carriers in GaAs Studied by Femtosecond Luminescence Spectroscopy," *Physical Review Letters* **66**, 1757 (1991)

[72] P. Grenier and J. F. Whitaker, "Subband gap carrier dynamics in low-temperature-grown GaAs," *Applied Physics Letters* **70**, 1998 (1997)

[73] S. Gupta, M. Y. Frankel, J. A. Valdmanis, J. F. Whitaker, G. A. Mourou, F. W. Smith and A. R. Calawa, "Subpicosecond carrier lifetime in GaAs grown by molecular beam epitaxy at low temperatures," *Applied Physics Letters* **59**, 3276 (1991)

[74] X. Q. Zhou, H. M. van Driel, W. W. Rühle, Z. Gogolak and K. Ploog, "Femtosecond carrier kinetics in low-temperature-grown GaAs," *Applied Physics Letters* **61**, 3020 (1992)

[75] R. J. Nelson and R. G. Sobers, "Minority-carrier lifetimes and internal quantum efficiency of surface-free GaAs," *Journal of Applied Physics* **49**, 6103 (1978)

[76] S. M. Sze and K. K. Ng, *Physics of Semiconductor Devices*, 3rd ed. (John Wiley & Sons, Hoboken, 2007)

[77] H. Haug and S. W. Koch, *Quantum Theory of the Optical and Electronic Properties of Semiconductors*, 5th ed. (World Scientific, Singapore, 2009)

[78] J. K. Wahlstrand, H. Zhang, S. B. Choi, J. E. Sipe and S. T. Cundiff, "Electric field-induced coherent control in GaAs: polarization dependence and electrical measurement [Invited]," *Optics Express* **19**, 22563 (2011)

[79] S. U. Dankowski, P. Kiesel, B. Knüpfer, M. Kneissl, G. H. Döhler, U. D. Keil, D. R. Dykaar and R. F. Kopf, "Annealing induced refractive index and absorption changes of low-temperature grown GaAs," *Applied Physics Letters* **65**, 3269 (1994)

[80] T. Jostmeier, *Kristallanisotropie der Zwei-Photonen-Absorption und des nichtlinearen Brechungsindex in GaAs*, Bachelor's thesis (TU Dortmund University, Dortmund, 2010)

[81] W. C. Hurlbut, Y.-S. Lee, K. L. Vodopyanov, P. S. Kuo and M. M. Fejer, "Multiphoton absorption and nonlinear refraction of GaAs in the mid-infrared," *Optics Letters* **32**, 668 (2007)

[82] D. H. Menzel, ed., *Fundamental Formulas of Physics*, vol. 1 (Dover Publications, New York, 1960)

[83] E. Y. Sherman, R. M. Abrarov and J. E. Sipe, "Dynamics of optically injected two-dimensional currents," *Journal of Applied Physics* **104**, 103701 (2008)

[84] S. Hunsche, H. Heesel, A. Ewertz, H. Kurz and J. H. Collet, "Spectral-hole burning and carrier thermalization in GaAs at room temperature," *Physical Review B* **48**, 17818 (1993)

[85] R. Tommasi, P. Langot and F. Vallée, "Femtosecond hole thermalization in bulk GaAs," *Applied Physics Letters* **66**, 1361 (1995)

[86] F. X. Camescasse, A. Alexandrou, D. Hulin, L. Bányai, D. B Tran Thoai and H. Haug, "Ultrafast Electron Redistribution through Coulomb Scattering in Undoped GaAs: Experiment and Theory," *Physical Review Letters* **77**, 5429 (1996)

[87] M. Grundmann, *The Physics of Semiconductors: An Introduction Including Devices and Nanophysics* (Springer, Berlin, 2006)

[88] T. Meier, G. von Plessen, P. Thomas and S. W. Koch, "Coherent Electric-Field Effects in Semiconductors," *Physical Review Letters* **73**, 902 (1994)

[89] T. Meier, F. Rossi, P. Thomas and S. W. Koch, "Dynamic Localization in Anisotropic Coulomb Systems: Field Induced Crossover of the Exciton Dimension," *Physical Review Letters* **75**, 2558 (1995)

[90] B. Pasenow, *Optische Erzeugung außergewöhnlicher Ladungsträgerverteilungen in Halbleiterstrukturen*, PhD thesis (Philipps-Universität Marburg, Marburg, 2006)

[91] X. Liu, D. Du and G. Mourou, "Laser Ablation and Micromachining with Ultrashort Laser Pulses," *IEEE Journal of Quantum Electronics* **33**, 1706 (1997)

[92] R. R. Gattass and E. Mazur, "Femtosecond laser micromachining in transparent materials," *Nature Photonics* **2**, 219 (2008)

[93] K. Sugioka and Y. Cheng, "Ultrafast lasers—reliable tools for advanced materials processing," *Light: Science & Applications* **3**, e149 (2014)

[94] J. Shah, *Ultrafast Spectroscopy of Semiconductors and Semiconductor Nanostructures*, 2nd ed. (Springer, Berlin, 1999)

[95] V. V. Lozovoy, I. Pastirk and M. Dantus, "Multiphoton intrapulse interference. IV. Ultrashort laser pulse spectral phase characterization and compensation," *Optics Letters* **29**, 775 (2004)

[96] B. Xu, J. M. Gunn, J. M. D. Cruz, V. V. Lozovoy and M. Dantus, "Quantitative investigation of the multiphoton intrapulse interference phase scan method for simultaneous phase measurement and compensation of femtosecond laser pulses," *Journal of the Optical Society of America B* **23**, 750 (2006)

[97] P. O'Shea, M. Kimmel, X. Gu and R. Trebino, "Highly simplified device for ultrashort-pulse measurement," *Optics Letters* **26**, 932 (2001)

[98] C. Iaconis and I. A. Walmsley, "Spectral phase interferometry for direct electric-field reconstruction of ultrashort optical pulses," *Optics Letters* **23**, 792 (1998)

[99] C. Iaconis and I. A. Walmsley, "Self-Referencing Spectral Interferometry for Measuring Ultrashort Optical Pulses," *IEEE Journal of Quantum Electronics* **35**, 501 (1999)

[100] P. Baum, S. Lochbrunner and E. Riedle, "Zero-additional-phase SPIDER: full characterization of visible and sub-20-fs ultraviolet pulses," *Optics Letters* **29**, 210 (2004)

[101] M. E. Anderson, A. Monmayrant, S.-P. Gorza, P. Wasylczyk and I. A. Walmsley, "SPIDER: A decade of measuring ultrashort pulses," *Laser Physics Letters* **5**, 259 (2008)

[102] E. Sidick, A. Dienes and A. Knoesen, "Ultrashort-pulse second-harmonic generation. II. Non-transform-limited fundamental pulses," *Journal of the Optical Society of America B* **12**, 1713 (1995)

[103] B. Tatian, "Fitting refractive-index data with the Sellmeier dispersion formula," *Applied Optics* **23**, 4477 (1984)

[104] J. Paye, M. Ramaswamy, J. G. Fujimoto and E. P. Ippen, "Measurement of the amplitude and phase of ultrashort light pulses from spectrally resolved autocorrelation," *Optics Letters* **18**, 1946 (1993)

[105] MATLAB implementation of the FROG algorithm by the group of R. Trebino (Georgia Institute of Technology), ver. 1.2.0,
available at `http://frog.gatech.edu/code.html` (last accessed on July 16, 2015)

[106] X. Gu, S. Akturk and R. Trebino, "Spatial chirp in ultrafast optics," *Optics Communications* **242**, 599 (2004)

[107] K. W. DeLong, D. N. Fittinghoff and R. Trebino, "Practical Issues in Ultrashort-Laser-Pulse Measurement Using Frequency-Resolved Optical Gating," *IEEE Journal of Quantum Electronics* **32**, 1253 (1996)

[108] M. Sheik-Bahae, "Quantum interference control of current in semiconductors: Universal scaling and polarization effects," *Physical Review B* **60**, R11257 (1999)

[109] B. Lee, "Review of the present status of optical fiber sensors," *Optical Fiber Technology* **9**, 57 (2003)

[110] A. Damascelli, Z. Hussain and Z.-X. Shen, "Angle-resolved photoemission studies of the cuprate superconductors," *Reviews of Modern Physics* **75**, 473 (2003)

[111] H. Petek and S. Ogawa, "Femtosecond time-resolved two-photon photoemission studies of electron dynamics in metals," *Progress in Surface Science* **56**, 239 (1997)

[112] J. B. Khurgin, "Current induced second harmonic generation in semiconductors," *Applied Physics Letters* **67**, 1113 (1995)

[113] B. A. Ruzicka, L. K. Werake, G. Xu, J. B. Khurgin, E. Y. Sherman, J. Z. Wu and H. Zhao, "Second-Harmonic Generation Induced by Electric Currents in GaAs," *Physical Review Letters* **108**, 077403 (2012)

[114] W. Franz, "Einfluß eines elektrischen Feldes auf eine optische Absorptionskante," *Zeitschrift für Naturforschung* **13a**, 484 (1958)

[115] L. V. Keldysh, "Behavior of Non-metallic Crystals in Strong Electric Fields," *Soviet Physics JETP* **6**, 763 (1958)

[116] L. V. Keldysh, "Ionization in the Field of a Strong Electromagnetic Wave," *Soviet Physics JETP* **20**, 1307 (1965)

[117] J. F. Lampin, L. Desplanque and F. Mollot, "Detection of picosecond electrical pulses using the intrinsic Franz–Keldysh effect," *Applied Physics Letters* **78**, 4103 (2001)

[118] J. L. P. Hughes and J. E. Sipe, "Calculation of second-order optical response in semiconductors," *Physical Review B* **53**, 10751 (1996)

[119] S. Buckley, M. Radulaski, K. Biermann and J. Vučković, "Second harmonic generation in photonic crystal cavities in (111)-oriented GaAs," *Applied Physics Letters* **103**, 211117 (2013)

[120] C. H. Lee, R. K. Chang and N. Bloembergen, "Nonlinear Electroreflectance in Silicon and Silver," *Physical Review Letters* **18**, 167 (1967)

[121] P. Godefroy, W. de Jong, C. W. van Hasselt, M. A. C. Devillers and T. Rasing, "Electric field induced second harmonic generation spectroscopy on a metaloxidesilicon structure," *Applied Physics Letters* **68**, 1981 (1996)

[122] J. Miragliotta and D. K. Wickenden, "Nonlinear electroreflectance from gallium nitride using optical second-harmonic generation," *Physical Review B* **53**, 1388 (1996)

[123] P. T. Wilson, Y. Jiang, O. A. Aktsipetrov, E. D. Mishina and M. C. Downer, "Frequency-domain interferometric second-harmonic spectroscopy," *Optics Letters* **24**, 496 (1999)

Publications

E. Sternemann, T. Jostmeier, C. Ruppert, H. T. Duc, T. Meier and M. Betz
"Femtosecond quantum interference control of electrical currents in GaAs: Signatures beyond the perturbative $\chi^{(3)}$ limit"
Physical Review B **88**, 165204 (2013)

E. Sternemann, M. Betz and C. Ruppert
"Phase-retrieval of femtosecond pulses utilizing $\omega/2\omega$ quantum interference control of electrical currents"
Optics Letters **39**, 3654 (2014)

E. Sternemann, T. Jostmeier, C. Ruppert, S. Thunich, H. T. Duc,
R. Podzimski, T. Meier and M. Betz
"Quantum Interference Control of Electrical Currents in GaAs Microstructures: Physics and Spectroscopic Applications"
submitted (2015)

Acknowledgements

I would like to thank all the people without whom this thesis would not have been possible. I am particularly grateful to ...

... my advisor Markus Betz for introducing me to ultrafast nonlinear optics, for his guidance and for his constant readiness to discuss arising questions and new ideas.

... Huynh Thanh Duc and Torsten Meier for the fruitful collaboration during the study of the high-intensity regime of QUIC.

... Claudia Ruppert for her ideas and calculations regarding the phase-retrieval via QUIC and Thorben Jostmeier for the productive collaboration in the final year of his master's degree. I also want to thank both of them as well as Christine Hautmann, Sebastian Thunich, Jan Lohrenz, Stephan Melzer and Manfred Janzen for their constant helpfulness and numerous entertaining as well as scientific discussions.

... Sebastian Thunich, the group of Alexander Holleitner at the Technische Universität München, Dieter Schuh, Werner Wegscheider and the group of Technische Physik 1 at the Friedrich-Alexander-Universität Erlangen-Nürnberg for excellent GaAs samples.

... Gisela Pike and Dirk Schemionek for help with the sample preparation.

... Lars Wieschollek, Klaus Wiegers, Thomas Stöhr and the members of the mechanical and electrical workshop for technical assistance.

... Michaela Wäscher and Nina Collette for administrative support.

... Manfred Bayer and all other members of Experimentelle Physik 2 for a pleasant working atmosphere and fun outside-of-work activities.

... Elisabeth Sternemann, Henning Sternemann and Thorben Jostmeier for proofreading.

... my family and of course Katharina for their unconditional support and encouragement.

Dortmund, July 2015, Elmar Sternemann